National Library of Canada

Bibliothèque nationale du Canada

Acquisitions and Bibliographic Services Branch

Direction des acquisitions et des services bibliographiques

395 Wellington Street
Ottawa, Ontario
K1A 0N4

395, rue Wellington
Ottawa (Ontario)
K1A 0N4

Your file Votre référence

Our file Notre référence

NOTICE

The quality of this microform is heavily dependent upon the quality of the original thesis submitted for microfilming. Every effort has been made to ensure the highest quality of reproduction possible.

If pages are missing, contact the university which granted the degree.

Some pages may have indistinct print especially if the original pages were typed with a poor typewriter ribbon or if the university sent us an inferior photocopy.

Reproduction in full or in part of this microform is governed by the Canadian Copyright Act, R.S.C. 1970, c. C-30, and subsequent amendments.

AVIS

La qualité de cette microforme dépend grandement de la qualité de la thèse soumise au microfilmage. Nous avons tout fait pour assurer une qualité supérieure de reproduction.

S'il manque des pages, veuillez communiquer avec l'université qui a conféré le grade.

La qualité d'impression de certaines pages peut laisser à désirer, surtout si les pages originales ont été dactylographiées à l'aide d'un ruban usé ou si l'université nous a fait parvenir une photocopie de qualité inférieure.

La reproduction, même partielle, de cette microforme est soumise à la Loi canadienne sur le droit d'auteur, SRC 1970, c. C-30, et ses amendements subséquents.

Canada

OPTICAL PROPERTIES OF TWO-DIMENSIONAL SEMICONDUCTOR HETEROSTRUCTURES: ION IMPLANTATION AND CARRIER DIFFUSION

by

Louis Bernard Allard

Submitted to the School of Graduate Studies in
partial fulfilment of the requirements
for the degree of Ph.D. in Physics

Department of Physics
University of Ottawa
Ottawa, Canada
October 1993

© Louis Bernard Allard, Ottawa, Canada, 1993

National Library of Canada

Acquisitions and Bibliographic Services Branch

395 Wellington Street
Ottawa, Ontario
K1A 0N4

Bibliothèque nationale du Canada

Direction des acquisitions et des services bibliographiques

395, rue Wellington
Ottawa (Ontario)
K1A 0N4

Your file Votre référence

Our file Notre référence

The author has granted an irrevocable non-exclusive licence allowing the National Library of Canada to reproduce, loan, distribute or sell copies of his/her thesis by any means and in any form or format, making this thesis available to interested persons.

L'auteur a accordé une licence irrévocable et non exclusive permettant à la Bibliothèque nationale du Canada de reproduire, prêter, distribuer ou vendre des copies de sa thèse de quelque manière et sous quelque forme que ce soit pour mettre des exemplaires de cette thèse à la disposition des personnes intéressées.

The author retains ownership of the copyright in his/her thesis. Neither the thesis nor substantial extracts from it may be printed or otherwise reproduced without his/her permission.

L'auteur conserve la propriété du droit d'auteur qui protège sa thèse. Ni la thèse ni des extraits substantiels de celle-ci ne doivent être imprimés ou autrement reproduits sans son autorisation.

ISBN 0-315-93552-9

Canada

UNIVERSITÉ D'OTTAWA
UNIVERSITY OF OTTAWA

Dédié à Gérard Allard, mon père.

Abstract

For the most part of this work, we study the effects of focused ion beam implantation in InGaAs/GaAs quantum well structures.

The technique of steady-state photoluminescence spectroscopy is utilized to study the compositional disordering occurring in InGaAs/GaAs quantum well structures having been implanted at different doses and subsequently annealed. Photoluminescence results of uniformly implanted regions of InGaAs/GaAs samples are given along with a simple formalism permitting the calculation of the interdiffusion lengths. These results, along with SIMS measurements, show that channeling effects play a most important role in disordering quantum wells that lie deep beneath the sample's surface. The observations also show a photoluminescence peak shift saturation with dose at approximately 2×10^{13} Ga^{+}/cm^{2}. Results of pattern-implanted samples give rise to the question of the minimum dose required to induce uniform compositional disordering in InGaAs/GaAs structures. Studies of this "critical" dose, are presented for both AlGaAs/GaAs and InGaAs/GaAs quantum well structures and show that the minimum dose required to induce intermixing in InGaAs/GaAs is approximately two orders of magnitude lower than that observed for the AlGaAs/GaAs structures which was 2×10^{10} Bi^{+}/cm^{2}.

As another major part of this work, we describe a novel, low light level optical detection system that can be easily configured

for various modes of operation. These include (1) time-integrated (steady-state) photoluminescence spectroscopy, (2) transient, spectrally gated photoluminescence decay, (3) time-windowed photoluminescence spectroscopy, (4) two-dimensional, time-integrated photoluminescence mapping, and (5) time-resolved, two-dimensional photoluminescence mapping with time resolution of ~100 ps.

We use the system in mode (5) to study electron-hole pair expansion in GaAs quantum wells as a function of temperature for a fixed excitation intensity. The results show that the diffusion coefficient rises from an initial value of 26 cm^2/s at 80 K to 38 cm^2/s at ~100 K and then monotonically decreases to a value of ~10 cm^2/s at room temperature. The rise in the diffusion coefficient is attributable to the gradual decrease of interface roughness scattering with increasing temperature while the decrease of the diffusion coefficient is attributable to the increase of phonon scattering mechanisms with increasing temperature. Results of diffusion at fixed temperature, but as a function of excitation intensity, are also presented and discussed.

Statement of Originality

The work carried out during the tenure of the author's Ph.D. research project is, to the best of his knowledge original and encompasses the following:

-integration of a two-dimensional microchannel plate photomultiplier with time-correlated single photon circuitry thereby yielding an experimental setup capable of time-resolved two-dimensional photoluminescence mapping;

-study of channelling effects in focused ion beam implanted InGaAs/GaAs strained quantum well structures;

-assessment of patterned focused ion beam implantation to produce quantum well wires and quantum well boxes in InGaAs/GaAs strained quantum wells;

-study of the minimum dose required to completely intermix uniformly implanted InGaAs/GaAs strained quantum wells.

Publications related to thesis:

T.E. Jackman, S. Charbonneau, L.B. Allard, R.L. Williams, I.M. Templeton, M. Buchanan, M. Vos, I.V. Mitchell, and J.A. Jackman. Compositional disordering of strained InGaAs/GaAs quantum wells by Au implantation: Channelling effects; Appl. Phys. Lett. 59 (21) 2733 (1991).

L.B. Allard, G.C. Aers, S. Charbonneau, T.E. Jackman, R.L. Williams, I.M. Templeton, M. Buchanan, D. Stevanovic, and F.J.D. Almeida. Fabrication of nanostructures in strained InGaAs/GaAs quantum wells by focused-ion-beam implantation; J. Appl. Phys. 72 (2) 422 (1992).

L.B. Allard, G.C. Aers, S. Charbonneau, T.E. Jackman, I.M. Templeton, and M. Buchanan. Focused-ion-beam implantation in strained InGaAs/GaAs quantum wells; Can. J. Phys. 70, 1023 (1992).

L.B. Allard, S. Charbonneau, and Jeff F. Young. A versatile, low light level optical detection system: from time-integrated emission spectra to time-resolved, two-dimensional emission mapping; Can. J. Phys. 70, 1199 (1992).

S. Charbonneau, L.B. Allard, Jeff F. Young, G. Dyck, and B.J. Kyle. Two-dimensional time-resolved imaging with 100 ps resolution using a resistive anode photomultiplier tube; Rev. Sci. Instrum. 63 (11), 1992.

L.B. Allard, S. Charbonneau, and Jeff F. Young. Two-dimensional, picosecond photoluminescence imaging of electron-hole pair expansion in GaAs quantum wells; Proceedings of the 21st International Conference on the Physics of Semiconductors, edited by Ping Jiang and Hou-Zhi Zheng, p. 1068, World Scientific (Singapore).

L.B. Allard, G.C. Aers, P.G. Piva, P.J. Poole, M. Buchanan, T.E. Jackman, S. Charbonneau, U. Akano, and I.V. Mitchell. The threshold dose for ion-induced intermixing in InGaAs/GaAs quantum wells. Submitted to Applied Physics Letters.

Presentations related to thesis:

L.B. Allard, S. Charbonneau, T.E. Jackman, G.C. Aers, I.M. Templeton, and M. Buchanan. In-plane migration of defects created by focused ion beam implantation in (In,Ga)As/GaAs strained quantum wells. Congress of the Canadian Association of Physicists, June 13-16 1993, Simon Fraser University, Burnaby B.C.

L.B. Allard. Photoluminescence de puits quantiques: effets d'implantation et propriétés de transport. Invited talk, Physics department, Université de Moncton, 5 February 1993.

L.B. Allard. Formation of quantum wires and quantum dots using focused ion beams. Graduate students seminar day, Ottawa-Carleton Institute for Physics, November 1991, Carleton University.

S. Charbonneau, L.B. Allard, T.E. Jackman, G.C. Aers, R.L. Williams, I.M. Templeton, and M. Buchanan. Optical characterization of focused ion beam implanted InGaAs/GaAs quantum well structures. 38th Scottish Universities Summer School in Physics: Physics of nanostructures, University of St. Andrews, Scotland, 29 July-9 August 1991.

Publications not immediately related to thesis:

S. Charbonneau, L.B. Allard, A.P. Roth, and T. Sudersena Rao. Time-resolved photoluminescence studies of biexcitons in InP; Phys. Rev. B (rapid communication) 47 (20) 13918 (1993).

D.J. Lockwood, G.C. Aers, L.B. Allard, B. Bryskiewicz, S. Charbonneau, D.C. Houghton, and A. Wang. Raman spectroscopy and optical properties of porous silicon. Proceedings of Phonons in nanostructures, September 1992, St-Felice, Spain. Sponsored by Nato.

D.J. Lockwood, G.C. Aers, L.B. Allard, B. Bryskiewicz, S. Charbonneau, D.C. Houghton, J.P. McCaffrey, and A. Wang. Optical properies of porous silicon; Can. J. Phys. 70, 1184 (1992).

T. Sudersena Rao, C. Lacelle, S.J. Rolfe, L.B. Allard, S. Charbonneau, A.P. Roth, T. Steiner, and M.L.W. Thewalt. Residual Impurities in High Purity InP Grown by Chemical Beam Epitaxy; Proceeding of The fifth international conference on InP and related materials, Paris, France, May 1993.

I.M. Templeton, M. Fallahi, S. Charbonneau, H.G. Champion and L.B. Allard. Focused-ion-beam damage-etch patterning for isolation of quantum structures in AlGaAs/GaAs; J. Vacuum Sc. and Technology, Nov.-Dec. 1993 issue, proceedings of the 37th Symposium on electron, ion and photon beam.

Presentation not immediately related to thesis:

L.B. Allard. Biexcitons dans l'InP. Invited talk, Physics department, Université de Montréal, 21 July 1993.

Acknowledgements

I have had the privilege to work with some very knowledgable people who were quite generous in the time they took for me. I wish to thank them.

Firstly, there is my thesis supervisor, Sylvain Charbonneau, who taught me many aspects of photoluminescence spectroscopy and semiconductor physics. Working with him permitted me to carry out measurements in his very well-equipped laboratory together with the benefits of being exposed to branches of semiconductor physics not immediately related to my thesis project.

Immediate collaborators were Geof Aers and Tom Jackman who provided vast input throughout the course of my research and with whom working again would be a pleasure.

I also had the opportunity to work with Jeff Young on the two-dimensional diffusion part of my project. This was enjoyable and will remain a high point of my stay at the National Research Council.

My presence at NRC was made possible by Marie D'Iorio. This kind gesture will not soon be forgotten.

I had the benefit of working, collaborating or receiving help from the following people: Mike Shahine, André Delâge, Simon Fafard, Sébastien Thériault and Gary Dyck.

Special thanks to: R.L. Williams, Z. Wasilewski and P. Coleridge for growth of samples; to J.P. McCaffrey for TEM measurements; to M. Buchanan for the RTA; to I.M. Templeton for the

FIB implanting; to D. Stevanovic and F.J.D. Almeida for RBS measurements; to M. Vos, U. Akano and I.V. Mitchell for ion implantation; to J.A. Jackman for SIMS measurements and to Geof Aers for calculations.

I appreciate and thank you all.

TABLE OF CONTENTS

Abstract.. iii

Statement of originality.............................. v

Acknowledgements...................................... viii

Table of contents..................................... x

List of figures....................................... xiii

List of Tables.. xvi

Chapter 1: Introduction............................... 1

1.1 Excitonic and free carrier confinement: from bulk to boxes.............................. 1

1.2 Photoluminescence spectroscopy.................... 11

1.3 Focused ion beam implantation..................... 16

1.4 Two-dimensional diffusion......................... 17

Chapter 2: Experimental techniques and apparatus........... 19

2.1 Introduction...................................... 19

2.2 Lasers in spectroscopy............................ 19

2.2.1 Lasers as excitation sources.................. 20

2.2.2 Mode locking................................. 23

2.2.3 Frequency doubling........................... 29

2.2.4 Synchronous pumping and pulse rejection... 35

2.3 Spectroscopy instrumentation...................... 36

2.3.1 Spectrometer................................. 36

2.3.2 Low-light-level optical detection system.................................. 37
2.4 Focused ion beam implantation.................... 52
2.5 Samples.. 53

Chapter 3: Focused Ion Beam Implantation.................. 54
3.1 Introduction.................................. 54
3.2 Focused Ion Beam............................... 55
3.3 Channeling Effects............................. 56
3.4 Wires and Boxes: An attempt..................... 69
3.4.1 Interdiffusion lengths.................... 75
3.4.2 Results................................... 81
3.5 The Critical Dose.............................. 91
3.6 Si^{+} Implantation: Low Dose Behaviour............ 111
3.7 Exciton lifetime and Implanted Dose.............. 113
3.8 Discussion..................................... 116

Chapter 4: Two-Dimensional Time-Resolved Photoluminescence Imaging... 120
4.1 Introduction.................................. 120
4.2 Temperature Dependence of the Diffusion Coefficient................................... 120
4.3 Diffusion coefficient Vs. excitation intensity... 126

Chapter 5: Conclusion.................................. 130

References.. 133

List of figures

1.1 Energy level of a single quantum well....................9

1.2 Density of states Vs. energy for bulk, 2D, 1D and 0D carriers....................12

1.3 K-space representation of PL mechanism for direct gap semiconductor and real space PL representation for quantum well structure....................13

1.4 Low temperature PL spectrum of high quality InP sample.....15

2.1 Brewster-angle-tilted birefringent crystal plate and its associated index ellipsoid....................24

2.2 Mode spectrum of a laser cavity and output intensity of a mode-locked laser....................26

2.3 Three-dimensional index ellipsoid for a positive uniaxial crystal....................34

2.4 Schematics of micro-computer-based optical detection setup....................40

2.5 Photoluminescence experimental setup....................44

2.6 Steady state PL spectrum of an AlAs/GaAs MQW along with its PL decay trace....................45

2.7 Time-resolved PL spectra of a high quality InP sample showing evidence of biexcitons....................49

2.8 Optical setup for 2D PL imaging....................51

3.1 Diagram showing compositional disordering mechanism........57

3.2 Cross-section of MQW sample....................59

3.3 Depth profile of 100 keV Au^+ ions implanted by FIB at 0° (nominal) in an InGaAs/GaAs structure....................63

3.4 Depth profile of 250 keV Au^+ ions implanted by FIB along the <100> crystal axis of an InGaAs/GaAs structure...65

3.5 Depth profile of 250 keV Au^+ ions implanted by FIB along the <100> crystal axis and 4° off-normal in an InGaAs/GaAs structure....................67

3.6 Diagram showing wire and box implantation patterns.........74

3.7 Diagram depicting the band structure of an InGaAs QW of width w before and after compositional disordering......77

3.8 Calculated transition energy shifts plotted as a function of interdiffusion length for two indium concentrations..80

3.9 PL spectra of sample #1020 before and after implantation...84

3.10 Ga^+ dose dependence of the PL transition energy shift for the four wells of sample #1020..........................85

3.11 Calculated interdiffusion lengths for the two lowest implanted doses in samples #1020 and #1021 along with the manner in which the indium concentration and the delivered dose vary with sample depth.......................87

3.12 Focused ion beam profile for gold ions......................92

3.13 PL peak energy shift Vs. implantation dose of 8 MeV bismuth ions into AlGaAs/GaAs sample #1198.................97

3.14 PL peak energy shift Vs. implantation dose of 8 MeV bismuth ions into AlGaAs/GaAs sample #1234.................98

3.15 Interdiffusion lengths fitted to PL energy shifts of figures 3.13 and 3.14.......................................99

3.16 PL spectra of virgin material and implanted material for QW4 of sample #1234 for a dose of 2 x $10^{10}/cm^2$.............100

3.17 PL peak energy shift Vs. implantation dose of 8 MeV bismuth ions into InGaAs/GaAs sample #1020.................103

3.18 PL peak energy shift Vs. implantation dose of 8 MeV bismuth ions into InGaAs/GaAs sample #1479.................104

3.19 PL peak energy shift Vs. implantation dose of 8 MeV bismuth ions into both InGaAs/GaAs samples #1020 and #1479...106

3.20 Interdiffusion lengths fitted to PL energy shifts of figures 3.17 and 3.18.......................................107

3.21 PL spectra of virgin material and implanted material for QW1 of sample #1020 for a dose of 6 x $10^{10}/cm^2$.............109

3.22 PL spectra for QW4 of sample #1021 showing doping effect of Si^+ ions for low dosage..........................112

3.23 Ga^+ dose dependence of the PL peak intensity decay time for the four quantum wells of sample #1020..................114

3.24 PL peak decay measurements for the n=1 heavy-hole exciton from QW3 of sample #1020............................117

4.1 Two-dimensional time-resolved PL images of photogenerated carriers at room temperature.................................122

4.2 Diffusion coefficient and carrier lifetime Vs. temperature for optically generated carriers in an AlAs/GaAs MQW sample...124

4.3 PL decay of AlAs/GaAs MQW sample for four different injected carrier densities..................................127

4.4 Full width half maximum data yielding diffusion coefficient for different injected carrier densities.......128

List of tables

III.I Energy shift of PL peak position after implantation-induced disordering for various implantation angles....68

III.II Comparison of the nominal indium concentration in the as-grown quantum wells for sample #1020 with the concentration determined from RBS measurements and by fitting PL transition energies....72

III.III Comparison of the nominal indium concentration in the as-grown quantum wells for sample #1021 with the concentration determined from RBS measurements and by fitting PL transition energies....73

III.IV Energy shift of PL after broad-area implantation and annealing of sample #1020 along with the calculated interdiffusion lengths required to give the fitted shift....83

III.V Energy shift of PL after broad-area implantation and annealing of sample #1021 along with the calculated interdiffusion lengths required to give the fitted shift....83

III.VI Energy shift of PL after wire-pattern implantation and annealing of sample #1020....88

III.VII Energy shift of PL after box-pattern implantation and annealing of sample #1020....89

III.VIII PL peak energy shift and interdiffusion length for sample #1198....95

III.IX PL peak energy shift and interdiffusion length for sample #1234....95

III.X PL peak energy shift and interdiffusion length for sample #1020....102

III.XI PL peak energy shift and interdiffusion length for sample #1479....102

Chapter 1

Introduction

1.1 Excitonic and free carrier confinement: from bulk to boxes

Since the advent of the molecular beam epitaxy (MBE) growth technique over two decades ago high-quality bulk semiconductors have been grown routinely[1.1]. In these crystals, excited carriers (electrons and holes) can thermalize from their excited state and become bound to each other pairwise by Coulombic interaction thereby forming what is called an exciton[1.2]. In materials having large covalent bonding, high mobility and large dielectric constant such as type IV and III-V semiconductors, the exciton is said to be of the Wannier-Mott type as opposed to the Frenkel type exciton which is typified by carriers in ionic crystals with low mobility and dielectric constant[1.3]. The radius of the latter is comparable to the crystal lattice parameter whereas the radius of the Wannier-Mott exciton can extend to many crystal unit cells and is the one we will consider in this work.

The calculation of the energy levels and Bohr radius of an exciton in a bulk semiconductor is solved straightforwardly by using the effective mass approximation (EMA) given that the electron and the hole are separated by many lattice constants. In this approximation, the periodicity of the crystal potential and the nature of its constituents are taken into account by the effective masses of the electron and the hole, m_e^* and m_h^*

respectively, and by the dielectric constant of the material.

Let us consider a direct gap semiconductors where an electron and a hole are far enough from each other to justify that the attractive potential between them be written

$$V(r) = -\frac{e^2}{\varepsilon r} \tag{1.1}$$

where r is the distance separating the carriers, e the fundamental charge and ε the dielectric constant of the material. By inserting (1.1) into Schrodinger's time independent equation in the center of mass frame of reference

$$\{-\frac{\hbar^2}{2\mu}\nabla^2_{\vec{r}_e-\vec{r}_h}+V(|\vec{r}_e-\vec{r}_h|)\}\psi_n(|\vec{r}_e-\vec{r}_h|)=E_n\psi_n(|\vec{r}_e-\vec{r}_h|) \tag{1.2}$$

one finds that the energy levels are given by

$$E_n(K) = -\frac{e^4\mu}{2\hbar^2\varepsilon^2 n^2}+\frac{\hbar^2K^2}{2M} \tag{1.3}$$

where μ is the reduced mass of the exciton given by $\mu^{-1} = m_e^{*-1} + m_h^{*-1}$, n is a positive integer, $M = m_e^* + m_h^*$ and $\hbar K$ is the exciton centre of mass momentum. Thus, one sees the analogy between an exciton and an hydrogen atom.

By solving (1.2) for n = 1, i.e. for the ground state of the system, one finds

$$\psi_{1s}(r) = (\pi a_x^3)^{-\frac{1}{2}} e^{-\frac{r}{a_x}} \tag{1.4}$$

where a_x is the exciton radius which gives the maximal radial probability density, also called the Bohr radius, given by

$$a_x = \frac{\hbar^2 \epsilon}{\mu e^2} \tag{1.5}$$

The exciton Rydberg (E_n for n = 1) can be expressed as

$$R_x = \frac{\mu e^4}{2\hbar^2 \epsilon^2} = \frac{e^2}{2\epsilon a_x} = \frac{\hbar^2}{2\mu a_x^2} \tag{1.6}$$

As an example consider GaAs for which $\mu = 0.058 m_o$, where m_o is the free electron rest mass and $\varepsilon = 12.5$. We then obtain R_x = 5 meV and a_x = 110 Å. These values support the claim that the EMA is appropriate and that such excitons will be stable at low temperatures. These excitons will exhibit true bulk-like properties if not dimensionally constrained, i.e. if the crystal volume in which it exists as a length scale larger than its Bohr radius. Free carriers will also have a three dimensional (3D) behaviour provided that their environment has a length scale larger than their associated de Broglie wavelength in every direction.

Up until now we have considered semiconductor crystals free of defects. Though modern growth techniques can provide very pure crystals, they are never defect-free. The epitaxial layers will always contain crystalline imperfections of some sort. One will have to deal with various type of impurities. These may be donor, acceptor or isoelectronic species that can appear interstitially or substitutionally. These impurities will perturb the crystal's periodic potential. The potential variations will act as binding centres where carriers are liable to get trapped or free excitons can simply become bound to the site in question and thus form a bound exciton. Excitons becoming bound to these sites and

recombining radiatively will emit photons at energies lower than that of the free excitons due to the extra localization energy. Peaks lower in energy than the free exciton peak will thus appear in the emission spectrum. These peaks can have very high intensities compared with that of the free excitons even when care is taken to have very clean growth chambers. The reason for this will become clear after we introduce the concept of oscillator strength[1,4].

Let us consider an electron bound to an atom by an elastic force. Its potential is written

$$V(r) = \frac{1}{2}m\omega_o^2 r^2 \tag{1.7}$$

where ω_o is the electron's natural angular frequency and m its mass. The equation of motion of the electron when subjected to an electric field $E_z=E\cos(\omega t)$ is

$$\frac{d^2z}{dt^2}+\omega_o^2 z=-\frac{e}{m}E_z \tag{1.8}$$

which yields the solution

$$z = A\cos(\omega_o t-\phi) - \frac{eE}{m(\omega_o^2-\omega^2)}\cos(\omega t) \tag{1.9}$$

whose first term on the right (with the two constant A and ϕ) represents the free motion of the electron while the other term is the particular solution of (1.8). In the case of weak damping (that we have neglected in the equation of motion) it can be shown that, when exciting at frequencies far from resonance, the particular solution suffices to describe the forced motion after

some time has elapsed since the onset of the excitation. Thus, after such a period of time, we have

$$z = -\frac{eE\cos(\omega t)}{m(\omega_o^2-\omega^2)} \tag{1.10}$$

The dipole moment of this system can then be expressed as

$$D(t) = -ez = \frac{e^2E\cos(\omega t)}{m(\omega_o^2-\omega^2)} = \chi E\cos(\omega t) \tag{1.11}$$

where we have introduced the susceptibility χ

$$\chi = \frac{e^2}{m(\omega_o^2-\omega^2)} \tag{1.12}$$

If we go through the quantum mechanical derivation of the induced dipole moment[1,3] we obtain the following

$$\langle D_z\rangle(t) = \frac{2e^2}{\hbar}E\cos(\omega t)\sum_n \frac{\omega_{no}|\langle\phi_n|Z|\phi_o\rangle|^2}{\omega_{no}^2-\omega^2} \tag{1.13}$$

where $|\phi_n\rangle$ are the quantum states of the oscillator. Let us now define the oscillator strength.

$$f_{no} = \frac{2m\omega_{no}|\langle\phi_n|Z|\phi_o\rangle|^2}{\hbar} \tag{1.14}$$

which satisfies

$$\sum_n f_{no} = 1 \tag{1.15}$$

and permits us to express the total electric dipole moment per unit volume as

$$N\langle D_z\rangle(t)=\sum_n Nf_{no}\frac{e^2}{m(\omega_{no}^2-\omega^2)}E\cos(\omega t) \qquad (1.16)$$

where N is the number of atoms contained in a volume whose dimension is much smaller than the driving wavelength.

Comparing (1.16) with (1.11) we can conclude that (1.16) corresponds to the situation where one has N classical oscillators (see equation (1.15)). f_{no} can thus be seen as the proportion of oscillators having angular frequency ω_{no}. In the study of excitons, we will assume these to behave like such oscillators.

Returning to the imperfections in a semiconductor crystal, it has been shown[1.5] that for an impurity bound exciton, the oscillator strength, f_i, obeys the following relation

$$f_i \sim \frac{a_x^3}{v}f_{ex} \qquad (1.17)$$

where f_{ex} is the oscillator strength of the free exciton, a_x its Bohr radius and v the volume of the crystal's primitive cell. This yields values of a_x^3/v in the $\sim 10^4$ range which tells us that a large number of excitons will recombine while bound to impurities rather than as free excitons. This explains why high intensity peaks related to impurity bound excitons are observed.

The oscillator strength also plays a role in the radiative recombination time of excitons. This lifetime, τ_r, is related to the oscillator strength, f, through the equation[1.6]

$$\tau_r = \frac{3mc^3}{2ne^2\omega^2 f} \qquad (1.18)$$

where n is the index of refraction of the material, m, the mass of the exciton and c the speed of light.

The development and perfection of growth techniques (MBE, chemical beam epitaxy (CBE), metal organic chemical vapour deposition (MOCVD)) now permit epitaxial thicknesses that can be controlled to monolayer precision[1.7]. This has opened the path to sequential growth of materials having different bandgaps which can lead to carrier confinement. Theoretical predictions and the possibility of new devices based on quantum effects made carrier confinement an attractive and now readily obtainable goal.

One specific method of achieving two-dimensional (2D) confinement is by sequentially growing two modulation doped semiconductor materials of different bandgaps thereby yielding a triangular-like confining potential for the uncompensated carriers. The appeal of this type of heterojunction is that the transfer of charge from one side of the junction to the other leads to a 2D carrier "gas" without the mobility-limiting impurities present[1.8].

Another way to achieve 2D confinement is by periodic sequential growth of semiconductors having similar lattice constants but differing bandgaps. The wider bandgap material acts as the barrier whereas the lower bandgap material is referred to as the well. The first to propose such a superlattice (SL) structure were Esaki and Tsu[1.9].

In this work we will be concerned only with single quantum well (QW) and multiple quantum well (MQW) structures and not with the above-mentioned SL. The difference between MQWs and SLs is

that in the latter, the barriers are narrow and low enough for the wave functions of the carriers in neighbouring wells to overlap as opposed to those in MQW who do not.

If one considers a bulk semiconductor material, its basic electronic and optical properties (i.e. essentially its band structure) are describable by quantum mechanics applied to the atomic realm. This can also be said for QW type heterostructures if one considers the appropriate boundary effects. To illustrate this, let us consider figure 1.1 in which a single QW is depicted.

Carriers (i.e. electrons in the conduction band and holes in the valence band) will experience a different potential along the X and Y axis than in the growth direction Z axis. In the plane perpendicular to the growth (i.e. the X,Y plane), the carriers will move in a periodic potential typical of the bulk material whereas along the growth axis they will see abrupt discontinuities at the heterointerfaces.

The discontinuity in the energy from the top of the barrier to the bottom of the well (for both electrons and holes) is related to the difference in bandgap energies of the well and barrier material and to the way they align themselves, the so-called band offset. A crude qualitative approximation of it may be given by the difference in the electronic affinity of the materials forming the barrier and the well[1.10]. If the width of the well is not too large and the barrier sufficiently high, confinement will occur, i.e. the electrons and the holes that are in their respective wells will have a discrete number of possible energy levels. In the case of

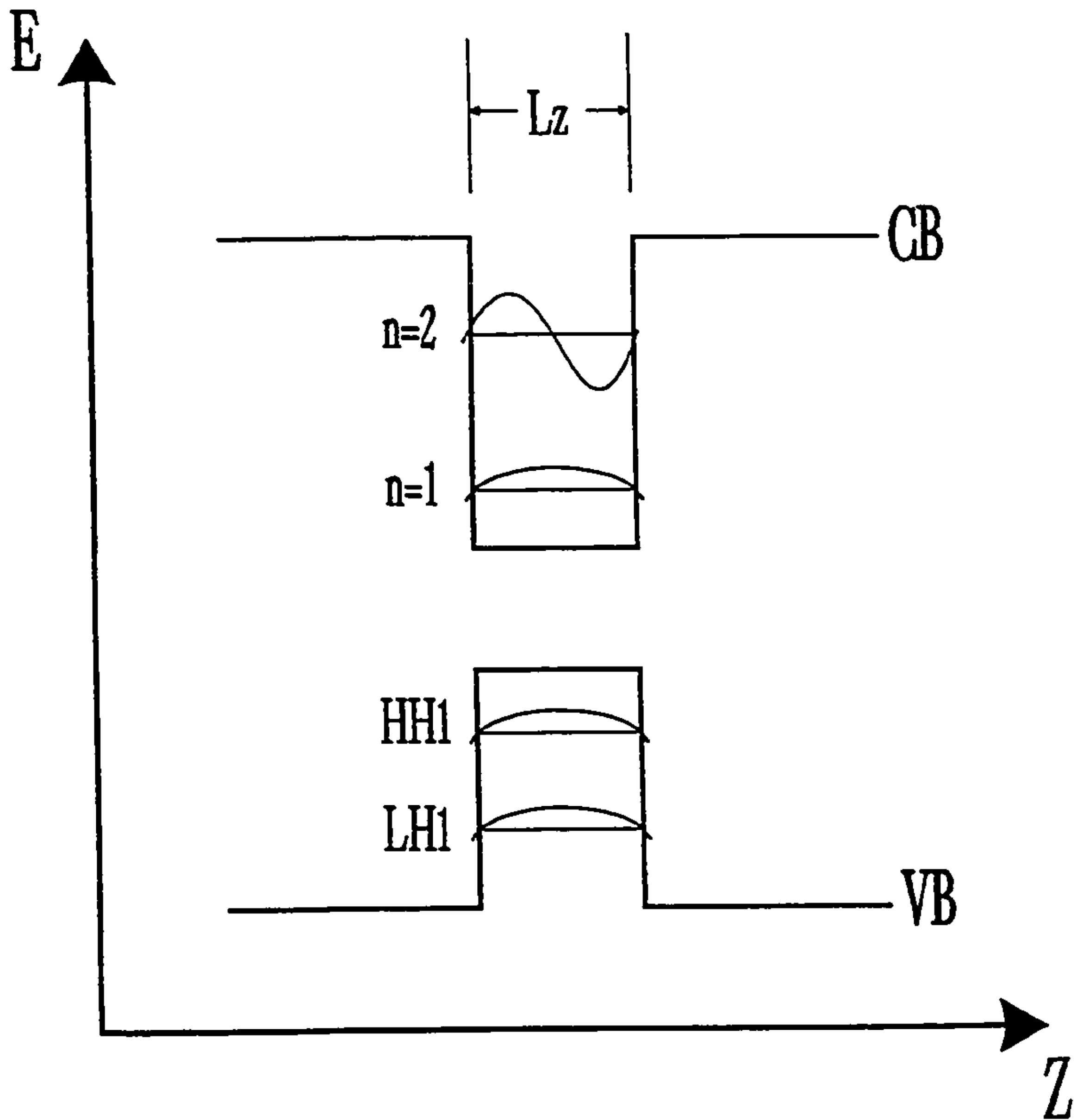

Fig. 1.1 Energy level diagram of a single QW of width Lz. CB and VB represent the conduction and valence bands of the heterostructure. The wavefunctions for the n=1 and n=2 electronic levels are depicted along with the wavefunctions of the first heavy hole (HH1) and light hole (LH1) levels.

infinitely high barriers, the energy levels for the well would be

$$E=E_n+\frac{\hbar^2}{2m^*}(k_x^2+k_y^2) \tag{1.19}$$

where

$$E_n=\frac{\hbar^2\pi^2}{2m^*}\frac{n^2}{L_z^2} \tag{1.20}$$

for n = 1,2,... and where m^* is the effective mass of the carrier considered. However, nature does not routinely provide such infinite barriers and analytical solutions are replaced by numerical analysis.

In this work, we will be interested in the optical properties of such QW's, especially in the photoluminescence (PL) emission of these. The first group to report on optical studies of quantum wells were Dingle et al.[1.11] who showed the absorption spectrum of GaAs QW's sandwiched between (Al,Ga)As barriers (typical of Fig. 1.1).

In quantum wells, the oscillator strength of free excitons increases with diminishing well width whereas that of bound excitons diminishes slightly from its bulk value[1.12]. This is consistent with the fact that the FE peak dominates in the emission spectra of quantum wells.

No theoretical reason exists to prevent the further confinement (less than 2D) of carriers in semiconductors i.e. to fabricate structures that would allow carrier motion in one given direction only. This type of structure is referred to as one dimensional (1D) or as a quantum "wire". Furthermore, pushing

confinement to its limits yields structures in which the carriers have no degree of freedom, the so-called quantum "boxes" or "dots", also referred to as zero dimensional structures (0D). In fact, only technological reasons limit the fabrication of these limited-size structures.

Carrier confinement gives rise not only to the quantization of the energy levels (a given energy level, say the ground state, for a given dimensionality structure will move to higher values with diminishing structure size and will move higher still with diminishing dimensionality) but also leads to marked differences in their associated density of states (DOS) as shown in figure 1.2 and this feature offers true potential for novel optoelectronic devices[1,13](e.g. quantum well lasers).

1.2 Photoluminescence spectroscopy

Luminescence spectroscopy essentially means the study of light emitted from excited material. That is, excited carriers are generated in the atoms (or the molecules) of the material by some means, subsequently recombine or relax to a lower energy level and photons are then emitted and detected. The term photoluminescence (PL) describes the manner in which the excited carriers are generated, that is, by absorption of light quanta. The PL technique will be the probing "tool" used throughout this work.

The PL mechanism considered throughout this work is shown in figure 1.3. In Fig. 1.3 (a), we have an incoming photon of energy

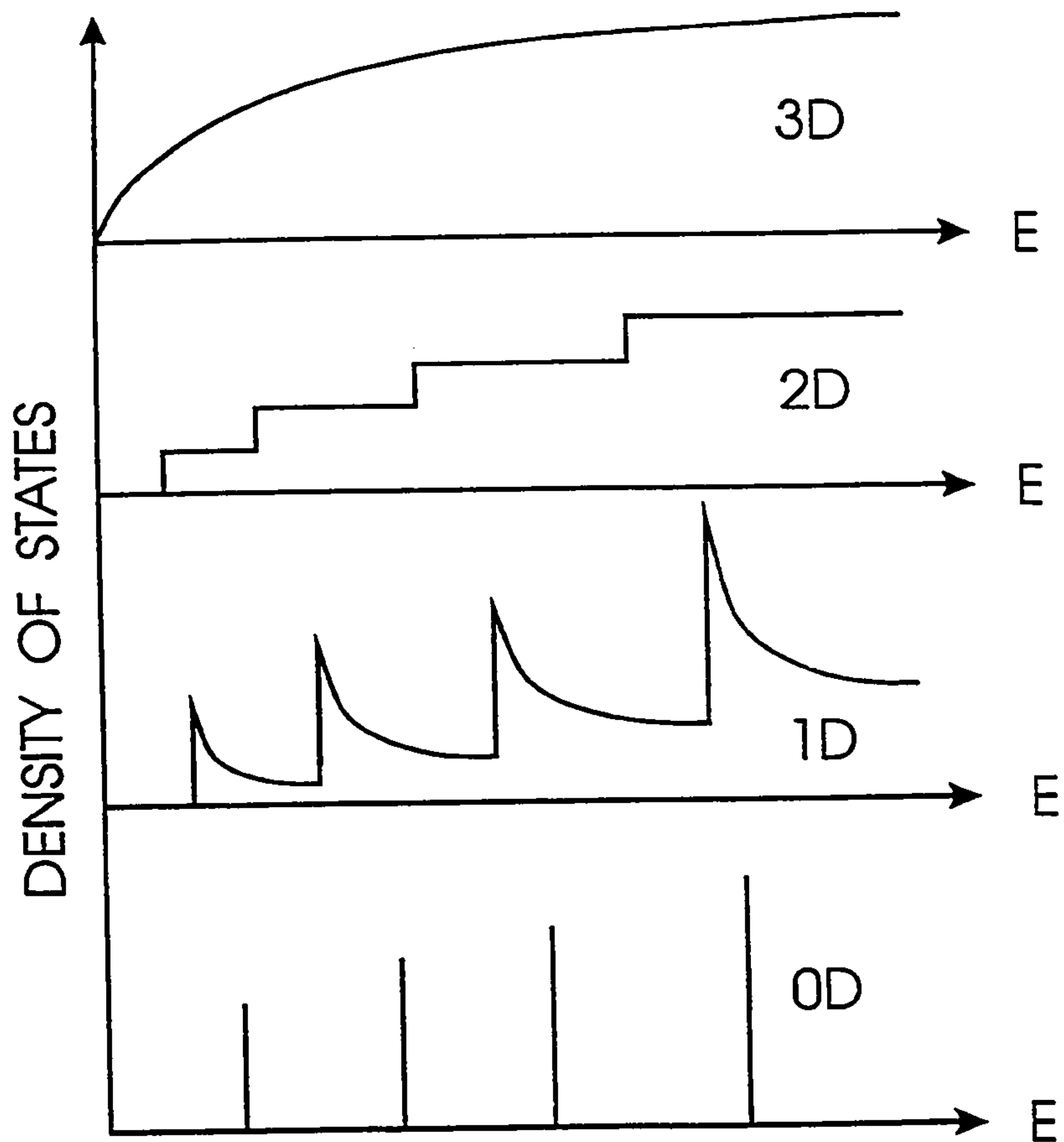

Fig. 1.2 Density of states Vs energy diagram for carriers in 3D (bulk), 2D (quantum wells), 1D (quantum wires) and 0D (quantum boxes).

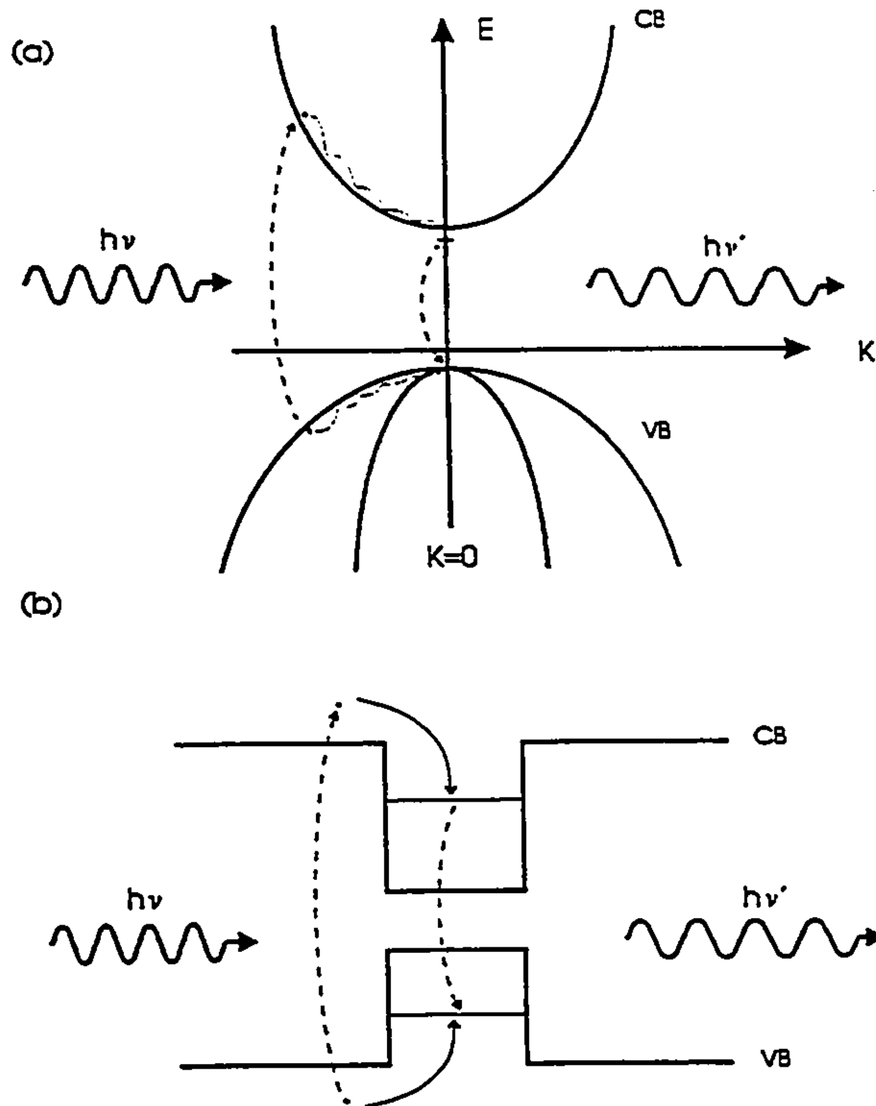

Fig. 1.3 (a) K-space representation of the PL mechanism in 3D direct gap semiconductor. The optically created carriers thermalize to their band extrema by emitting LO and acoustic phonons. The carriers recombine after having formed an exciton. (b) Real-space representation of PL mechanism in a QW structure.

hv impinging on a direct bandgap semiconductor. This photon extracts an electron from the valence band, leaving a hole behind in the process. The electron and the hole thermalize to the extrema of their respective band by emitting phonons, form an exciton (if the temperature warrants it) and thereafter recombine emitting a photon of energy hν′ with ν′ < ν.

In the case of indirect gap semiconductors the process is essentially the same except that in order to have conservation of momentum, the emission or absorption of phonons is required during the recombination process. This is observed as the so called Stoke shift. Fig. 1.3(b) illustrates the PL process for a quantum well.

Steady state PL (or time-integrated PL) has been extensively used to gain information about intrinsic and extrinsic energy levels in a variety of semiconductors materials[1.14]. A typical PL spectrum of a high quality InP sample is given as an example[1.15] in figure 1.4. There we see the free exciton (FE) peak with the donor-bound ((D°,X), (D^{+},X)) and acceptor-bound ((A°,X)) excitons along with the neutral donor to valence band ((D°,h)) transition. They all lie on the low-energy side of the FE transition and their relatively weak intensities (with respect to the FE peak intensity) is representative of the sample's high quality.

The possibility to measure the lifetime of various emission lines can greatly enhance one's ability to deduce detailed information concerning the nature of the corresponding transitions, especially in cases where a number of unknown, closely spaced peaks are observed in the steady state spectra[1.16].

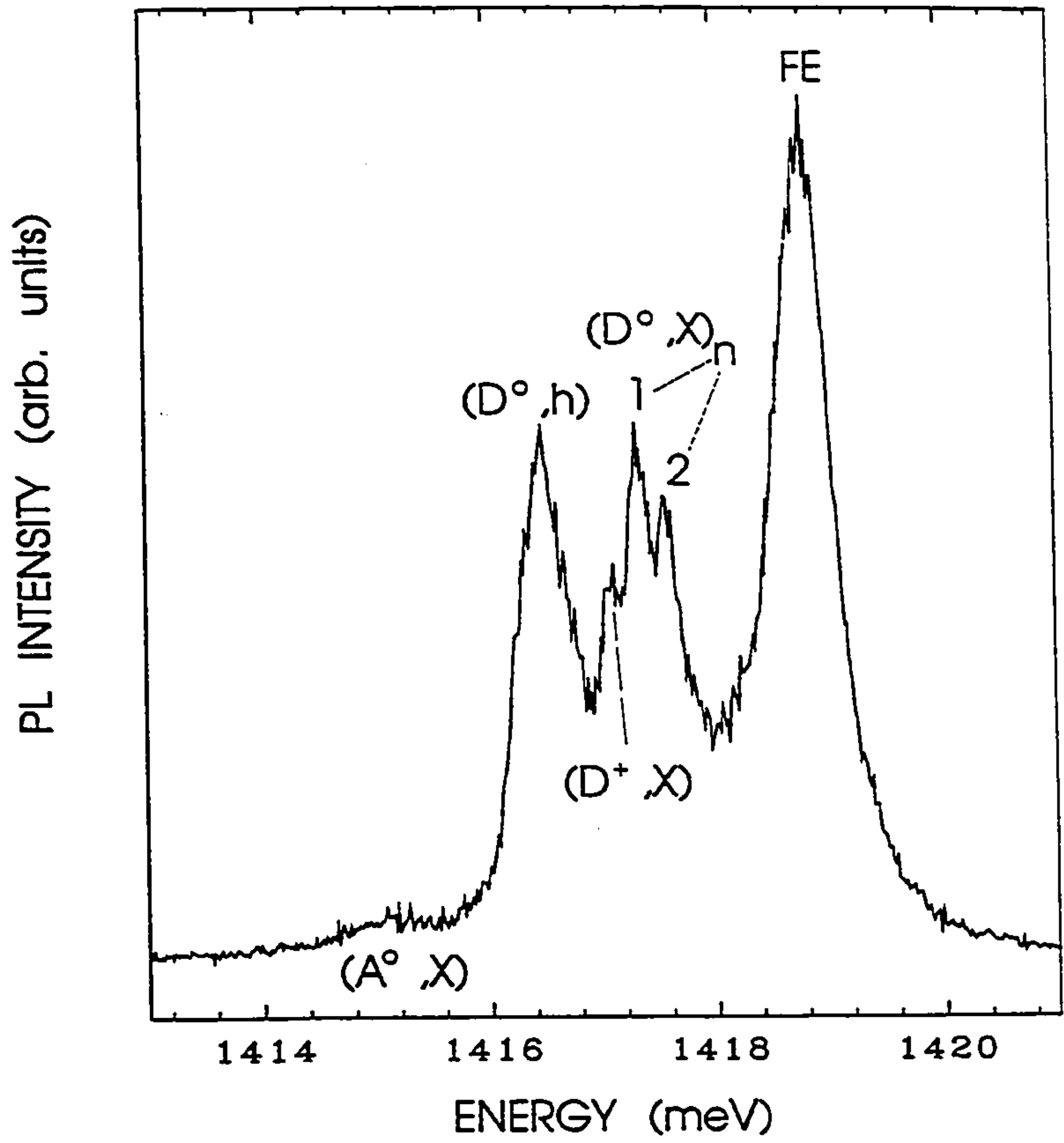

Fig. 1.4 Low temperature (5K) CW PL spectra of an InP sample. The exciting wavelength was 870 nm. The various emission peaks are identified as follows, FE: free exciton, (D°,X): exciton bound to neutral donor, (D^{+},X): exciton bound to ionized donor, (D°,h): neutral donor to valence band recombination and (A°,X): exciton bound to neutral acceptor.

A number of other techniques can be derived from steady-state PL and time-resolved (TR) PL, all of which can provide additional information regarding the nature of the radiative transition under investigation. We shall present in the subsequent chapter an experimental setup capable of carrying out several of these optical techniques including a novel two-dimensional TR PL technique permitting the study of transport properties of electron-hole pairs.

1.3 Focused ion beam implantation

The study of 2D systems was made possible by the advances of growth techniques as we have already pointed out. The problem of reducing the structure size to 1D and 0D is still not fully solved. Numerous techniques have been developed in this attempt. In her review on "Optical properties of III-V semiconductor quantum wires and dots"[1.17], K. Kash discusses some of these techniques which include the following: etching arrays of free-standing structures from quantum wells sometimes combined with high quality regrowth of confining layers; growth of quantum wells on nonplanar substrates (particularly v-groove substrates) or on tilted substrates and the technique of strain confinement by a strained layer separated from a quantum well by a thin barrier and thereafter patterned.

One of the goals of this research is to investigate the technique of focused ion beam (FIB) patterned implantation combined

with rapid thermal annealing in the (In,Ga)As/GaAs QW system for the eventual fabrication of quantum wires and quantum dots. In chapter 3, we will show that obtaining quantum wires and quantum boxes in (In,Ga)As/GaAs strained quantum wells by using FIB implantation is a complicated task.

The major appeal of the FIB implantation technique, is that it does not require the use of masks and therefore no need for removal of these by etching. Thus the number of fabrication steps required for the production of devices is reduced. This is particularly appealing for the fabrication of optical devices whose optical quality is known to decrease with the number of fabrication steps involved in their fabrication. Chapter 3 will deal in part with FIB implantation into quantum wells.

1.4 Two-dimensional diffusion

We will present in the following chapter a PL imaging system capable of carrying out 2D TR PL imaging. This enables us to follow the spatial and temporal evolution of a laser-pulse-created cloud of electron-hole pairs as they drift away from the centre of the excitation and to extract information on the scattering mechanisms involved (interface roughness, impurity scattering, barrier-alloy scattering, phonon scattering). We will demonstrate the usefulness of this PL mode of operation by obtaining diffusion coefficient values at different temperatures for an AlAs/GaAs MQW

structure. The clear advantage of this system is that it requires no sample preparation or scanning hardware unlike other previously reported techniques[1-18].

Chapter 2

Experimental techniques and apparatus

2.1 Introduction

This chapter will focus on three areas of experimental techniques. The first area will cover the aspect of lasers in spectroscopy. We will describe the basics of operation for the lasers we have used and of their related components. The second area of interest will be the photoluminescence setup we have developed. An in-depth look at its associated electronics will be given with a description of its various operating modes to demonstrate its versatility. Finally, we will discuss the focused ion beam implanter used to disorder our samples.

2.2 Lasers in spectroscopy

The advent of lasers has had a tremendous impact on spectroscopy. The coherent light sources are characterized by their spectral energy densities which may be several orders of magnitude bigger than those of incoherent sources. This aspect of lasers greatly reduces noise problems due to detectors or to background radiation. Moreover, the small bandwidths of single-mode lasers permit a spectral resolution far better than that of usual spectrometers. Given these two elements, it is clear that

experiments which could not previously be done due to low light intensities and/or inadequate spectral resolution can now be routinely carried out.

A particularly interesting type of laser is the continuously tunable one which in many cases replaces wavelength-selecting elements such as spectrometers and interferometers. Tunable dye lasers and solid state based lasers such as the Ti:sapphire are representative of this type of laser and are used extensively in research.

The development and refinement of techniques such as Q-switching and mode-locking now permit the study of fast transient phenomena. Apart from the short pulses thereby generated, $\approx 10^{-8}$ seconds for Q-switching[2.1] and less than 10^{-9} seconds for mode-locking[2.2], another benefit is the high peak power of these pulses.

2.2.1 Lasers as excitation sources

In this sub-section we give a summary of the lasers and laser techniques used to excite luminescence. For more extensive details, the reader is referred to other references[2.3].

Some lasers operate in a continuous wave (CW) while others are pulsed. These two types of lasers are available in fixed frequency lasing and in tunable frequency lasing varieties. The active medium of the lasers will often show gain on many transitions and

the laser is liable to oscillate simultaneously on many lines. Given that these different gain regions are narrow and distinct from each other, the wavelength of each line will be restricted to its narrow gain range and the laser will be referred to as a multi-line fixed wavelength laser. Many electrically pumped CW gas lasers are of this type, e.g. the Argon ion laser whose two strongest emission lines are at 488 nm and 514.5 nm. The laser we used as our above-bandgap CW excitation source was a 5 mW HeNe whose principal emission line is 632.8 nm. To ensure that the other plasma lines present in the He-Ne mixture did not play any role in our collected spectra, a Fabry-Perot passing only the 632.8 nm line was placed at the output of our HeNe laser.

Conversely, there exist many cases where the active medium gain regions are broad and no longer fully distinguishable. The prime example being the dye laser[2-4] where the stimulated emission from the excited state to many vibrational levels is possible. Due to the strong interaction of the dye molecules with the solvent, these levels are broadened to the point that their linewidths exceed the level separation. Therefore, the absorption and fluorescence of the dye solution show a broad continuous spectral distribution and the gain profile can extend over a large spectral range of several hundred nanometres. In this case, where the laser wavelength can be tuned continuously over a large spectral range, we have a tunable laser.

Let us consider a simple cavity of length d. The possible laser wavelengths λ_L are determined from the optical distance

separating the resonator mirrors by[2.5]:

$$q\lambda_L=2nd \tag{2.1}$$

where q is a positive integer and n is the index of refraction of the medium. This cavity length wavelength-selection method is, however, insufficient for most lasers since the gain bandwidth is usually much larger than the intermode spacing.

Thus, to achieve a single-line oscillation in a medium having gain for several transitions, we must introduce wavelength-selecting elements either inside or outside the resonator cavity. In the case of lines having a wide spectral separation, one can use the selective reflectivity of dielectric mirrors to isolate a single transition. On the other hand, for broadband reflectors and/or closely spaced lines, one can use prisms, gratings, Lyot filters or birefringent filters for wavelength selection. In our Coherent 599 Dye Laser, this selection is achieved by a birefringent filter tuning element. This device achieves wavelength selection by the interference of polarized light passing through a birefringent crystal and is well described elsewhere[2.6]. To summarize how it works, let us consider a birefringent plate sandwiched between two perfectly parallel polarizers placed in such a way that the normally incident polarized light is split equally between the components corresponding to the two indices of refraction of the crystal. It can then be shown that the light intensity transmitted through the crystal will vary with wavelength according to:

$$\cos^2\left(\frac{\pi \Delta n t}{\lambda}\right) \tag{2.2}$$

where λ is the wavelength, t the crystal plate thickness and $\Delta n = n_o - n_e$ (n_o is the ordinary index while n_e is the extraordinary one). The same transmitted intensity can be achieved if, instead of having polarizers, we tilt the plate so that the impinging beam strikes it at the Brewster angle thereby yielding p-polarized transmitted light. Thus if the optical axis of the plate is not in the plane defined by the p-polarized light, the incoming wave will be split into an ordinary wave and an extraordinary one. To clarify this, let us consider figure 2.1. The ordinary refractive index is the same whatever the value of the angle θ; however, n_e depends on θ. Therefore, Δn depends on θ and, for (2.2) to be maximized, the transmitted wavelength must change if θ (i.e. Δn) is varied.

A single birefringent plate alone would not tune a laser with very much precision. That is why our laser's birefringent filter tuning element consists of three quartz plates placed inside the dye laser's cavity thereby yielding a 40 GHz linewidth (0.5 Å for a wavelength of 630 nm).

2.2.2 Mode locking

Laser mode locking is a technique permitting the generation of very short duration, high peak power laser pulses. These pulses are said to be mode-locked when the resonator cavity modes are made

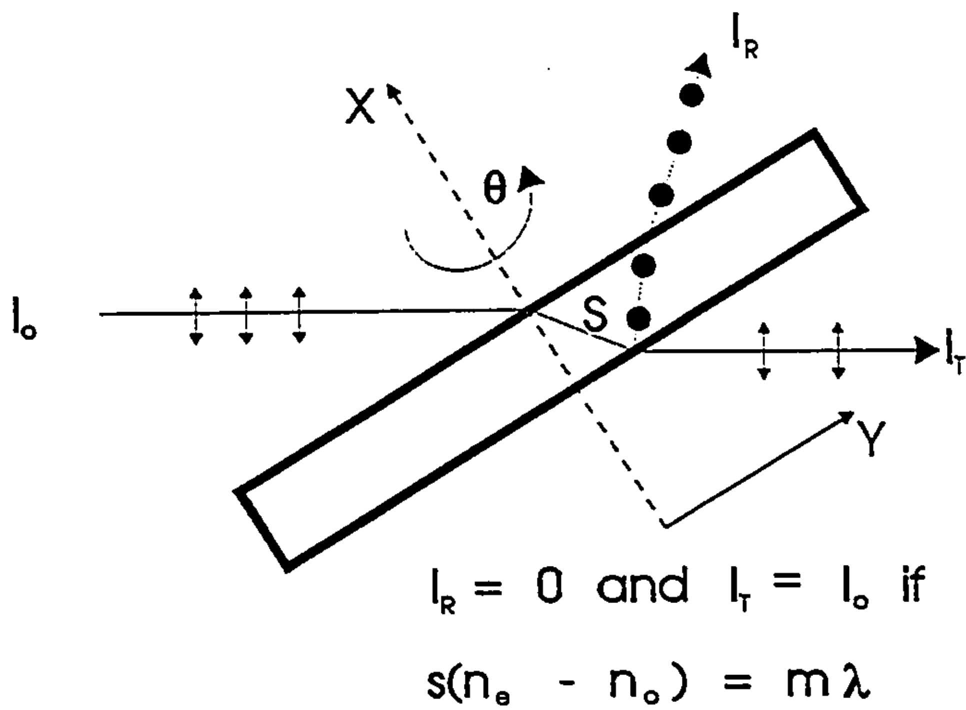

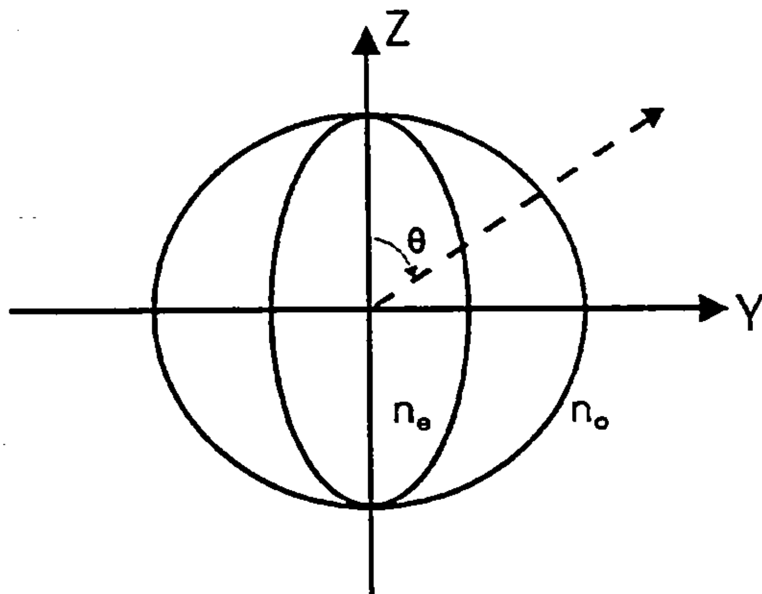

Fig. 2.1 Brewster-angle-tilted birefringent plate used as a tuning element and its corresponding index ellipsoid.

to oscillate with comparable amplitudes and locked phases.

To illustrate how this works, let us consider 2n+1 longitudinal modes oscillating with the same amplitude E_o and let us also assume that their locked phases ϕ_l obey the relation

$$\phi_l - \phi_{l-1} = \phi \tag{2.3}$$

Thus, the electric field resulting from this can be written, for any point inside or outside the cavity of length L, as

$$E(t) = \sum_{l=-n}^{n} E_o \exp\{i([\omega_o + l\Delta\omega]t + l\phi)\} \tag{2.4}$$

where $\omega_o = 2\pi\nu_o$ is the frequency of the central mode, (see figure 2.2(a)). The frequency spacing $\Delta\omega = \pi c/L$ since the condition for having a standing wave inside a resonator of optical length L is $q\lambda_q/2 = L$ where q is a positive integer. Therefore, the mode spacing is

$$\Delta\nu = \frac{\Delta\omega}{2\pi} = \frac{c}{2L} \tag{2.5}$$

Thus, equation (2.4) can be reduced to the following form

$$E(t) = A(t)\exp(i\omega_o t) \tag{2.6}$$

where

$$A(t) = E_o \frac{\sin[(2n+1)(\Delta\omega t + \phi)/2]}{\sin[(\Delta\omega t + \phi)/2]} \tag{2.7}$$

The output power will be proportional $A^2(t)$ and an example illustrating the mode-locking of 21 modes is shown in figure 2.2(b). Furthermore, this phase locking forces the oscillating modes to interfere in a way to produce short light pulses whose peak separation is found by subtracting two consecutive arguments that yield a nil denominator for (2.7). The pulse separation is

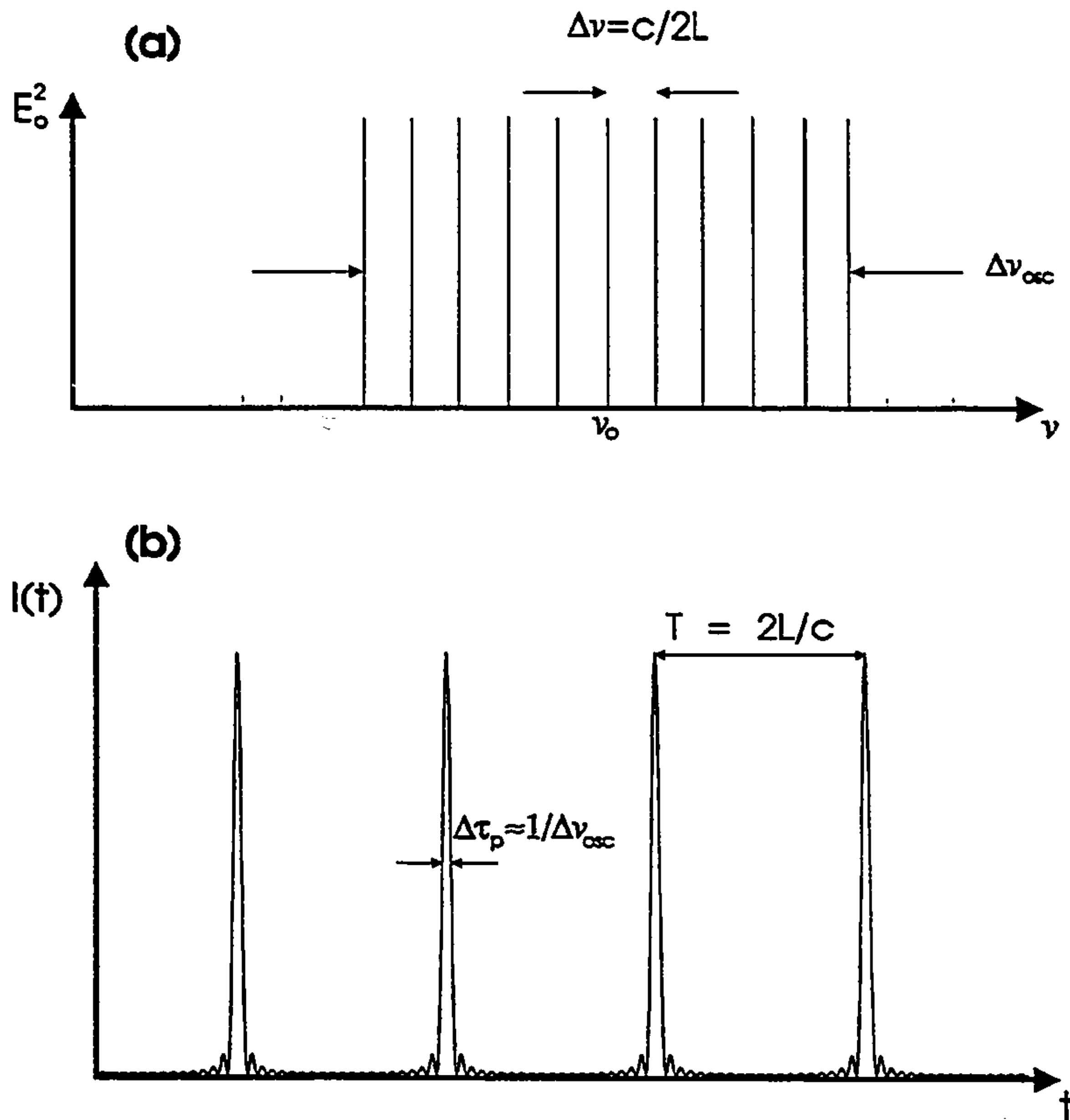

Fig. 2.2 (a) Mode spectrum for a cavity of length L. (b) Output intensity of a mode-locked laser. The output is made up of periodic ultrashort pulses.

found to be

$$T=\frac{2L}{c} \tag{2.8}$$

One can also deduce from (2.7) that the full width at half maximum of a pulse is

$$\Delta\tau_p\approx\frac{1}{\Delta\nu_{osc}} \tag{2.9}$$

where

$$\Delta\nu_{osc}=(2n+1)\Delta\nu \tag{2.10}$$

is the total oscillating bandwidth.

Another interesting characteristic is that the peak intensity of a pulse is given by

$$I_{peak}=(2n+1)\langle I\rangle \tag{2.11}$$

where <I> is the average intensity[2.7].

Most mode-locking methods fall into one of the two following categories: (1) mode-locking by nonlinear optical material (passive mode-locking) or (2) mode-locking by an active modulator operated by an external signal (active mode-locking).

We will concern ourselves with the active mode-locking scheme used with our Coherent Antares 76-S Nd^{3+}:YAG laser. The modulator in this case is an acousto-optic one which produces a periodic diffraction loss inside the cavity. To illustrate its operation let us consider the following.

Assume a sinusoidal transmission modulation of the form:

$$T=\frac{(1+\delta\cos(\Omega t))}{2} \tag{2.12}$$

The amplitude of a mode, say the centre one, will now be written as

$$A_o(t)=TE_o\exp(i\omega_o t)=\frac{E_o}{2}(1+\delta\cos(\Omega t))\cos(\omega_o t) \tag{2.13}$$

which we can rewrite as

$$A_o(t)=\frac{E_o}{2}\cos(\omega_o t)+\frac{E_o\delta}{4}[\cos((\omega_o+\Omega)t)+\cos((\omega_o-\Omega)t)]. \tag{2.14}$$

If the modulation Ω is such that

$$\frac{\Omega}{2\pi}=q\frac{c}{2L}=q\Delta\nu \tag{2.15}$$

(i.e. equal to a finite multiple of the mode spacing) the sideband amplitudes

$$A_{\pm1}=\frac{E_o\delta}{4}\cos(\omega_{\pm1}t) \tag{2.16}$$

are generated in the adjacent modes which are further amplified by stimulated emission. These three waves will be in phase at times

$$T_k=\frac{2\pi}{\Omega}k; \quad k=0,1,2,3,... \tag{2.17}$$

The modulation of these waves will generate new sidebands at $\omega_{\pm2}=\omega_o\pm2\Omega$ and these in turn will do the same until all the modes within the gain profile of the active medium oscillate with mutually coupled phases, i.e. the 2n+1 modes in the gain bandwidth $\Delta\nu_{osc}$. Thus, the superposition of these phase-coupled modes gives a total amplitude

$$A(t)=\sum_{l=-n}^{+n}A_l\cos((\omega_o+l\Omega)t). \tag{2.18}$$

Thus, the output field is mode-locked and is of the form shown in figure 2.2(b). In the case of our Nd^{3+}:YAG laser, the acousto-optic modulator is driven at half the cavity mode spacing frequency to produce a cavity loss modulated at the mode frequency separation. That is, the refractive index variation in the crystal, due to the

standing sound wave in the medium (frequency ω_s, wavevector k_s), can be written

$$\Delta n(z,t) = A \sin(\omega_s t+\theta)\sin(k_s z). \tag{2.19}$$

The temporal oscillation at frequency ω_s implies that the diffraction is most effective at times t such that

$$\sin(\omega_s t+\theta) = \pm 1. \tag{2.20}$$

Consequently, the "strength" of the diffraction varies harmonically in time with frequency $2\omega_s$ and hence a modulated cavity loss at the mode-spacing frequency is achieved by driving the modulator at half this frequency.

Since the length of our acousto-optic modulator crystal is fixed, the precise frequency tuning is achieved by controlling the temperature of the crystal.

The pulse width of our 1.064μm Nd^{3+}:YAG laser line is approximately 100 ps. These relatively wide pulses can be narrowed by being frequency doubled and then used to synchronously pump our previously described dye laser. Frequency doubling is described below.

2.2.3 Frequency doubling

The semiconductor heterostructures we will be interested in are characterized by luminescence emission in the 700 to 900 nm region. We will be studying the photoluminescence which means that luminescence-generating photons of energy greater than the observed

transitions are required. Consequently, for time-resolved PL measurements, the 1.064μm line of our Nd^{3+}:YAG is inadequate for either directly pumping the sample or pumping a dye laser (which cannot lase at energies greater than the pumping wavelength). We will resolve this problem by using the second harmonic of the 1.064μm line generated in a LiB_3O_5 (LBO) nonlinear crystal.

A material is referred to as being optically either linear or nonlinear depending on whether or not its polarization vector is proportional to the driving electric field. Thus, as an intense laser-generated sine wave interacts with a nonlinear material, its shape becomes distorted as the electric field goes through its maximum. A distorted wave will contain harmonics of its fundamental frequency. So, for a classic linear medium, the induced dielectric polarization is related to the applied electric field in the following manner

$$\vec{P}=\varepsilon_o\chi\vec{E} \tag{2.21}$$

where χ is the dielectric susceptibility and ε_o is the permittivity of empty space. When high intensity laser beams are involved, (2.21) is no longer a good approximation and terms of higher order in E must be considered. This nonlinear response is at the basis of energy exchange between electromagnetic waves of different frequencies. For the following discussion we shall consider only one additional term, the one proportional to the square of the electric field and consequently we will only be concerned with the frequency transformation leading to second harmonic generation (SHG). The generation of coherent light of frequency 2ω, from a

laser beam of frequency ω impinging on a nonlinear crystal was first shown in the early sixties[2.8]. Let us rewrite (2.21) with the additional term as

$$\bar{P}=\bar{P}^{L}+\bar{P}^{NL} \tag{2.22}$$

where P^{L} is the linear polarization term (2.21) and

$$P^{NL}=2\epsilon_0 dE^2 \tag{2.23}$$

is the nonlinear polarization where d is a coefficient whose dimension is that of the inverse of an electric field. The origin of (2.23) stems from the nonlinear deformation of the orbitals of the outer, loosely bound electrons of the atomic system when subjected to high fields. A classical analogy to this would be the response of a spring when subjected to large displacements i.e. when it no longer obeys Hooke's law. To get a feeling for the field strength required to observe nonlinear behaviour, let us consider P^{L} and P^{NL} to be of equal magnitude. This yields $E \approx O(\chi/d)$ and since $\chi \approx 1$ we can expect 1/d to be of the order of the field existing at the radius of an atom which, for a 1 Å radius gives $1/d \approx 10^{11}$ V/m. For crystal having an inversion centre, d must be zero since symmetry dictates that a field reversal must give a reversal of the polarization vector and since P^{NL} is proportional to the square of E, that is only possible when d=0.

Now, let us consider a monochromatic plane wave of frequency ω propagating along the z direction in a nonlinear crystal. We can write it as

$$E_{\omega}(z,t)=\frac{1}{2}\{E(z,\omega)\exp[i(\omega t-k_{\omega}z)]+C.C.\} \tag{2.24}$$

where C.C. is the complex conjugate of the term on its left and the

wavevector at frequency ω is

$$k_\omega=\frac{n_\omega \omega}{c} \tag{2.25}$$

where n_ω is the crystal index of refraction at frequency ω. This yields a nonlinear polarization term of the form

$$P_{2\omega}^{NL}=\frac{e_o d}{2}\{E^2(z,\omega)\exp[i(2\omega t-2k_\omega z)]+C.C.\} \tag{2.26}$$

This polarization wave will radiate at frequency 2ω thereby generating an electromagnetic wave at the second harmonic frequency 2ω [2.9]

$$E_{2\omega}(z,t)=\frac{1}{2}\{E(z,2\omega)\exp[i(2\omega t-k_{2\omega}z]+C.C.\} \tag{2.27}$$

where

$$k_{2\omega}=\frac{2n_{2\omega}\omega}{c}. \tag{2.28}$$

By comparing (2.26) and (2.27) we arrive at the conclusion that if SHG is to occur efficiently, we require that the phase velocity of the polarization wave be equal to that of the generated wave. That is

$$\frac{2\omega}{2k_\omega}=\frac{2\omega}{k_{2\omega}} \rightarrow k_{2\omega}=2k_\omega \tag{2.29}$$

which we rewrite

$$n_{2\omega}=n_\omega \tag{2.30}$$

which is referred to as the phase-matching condition.

As previously-mentioned, a birefringent crystal is one in which the refractive index depends on the polarization of the light wave in the medium. We can use such crystals to get the prescribed phase-match. In these crystals, there exists a direction, referred to as the optical axis, along which the refractive index is

independent of the direction of polarization. A uniaxial crystal has only one such optical axis. It can be shown that for such anisotropic crystals, a given direction of propagation of light can yield two different polarizations each having a different index of refraction. We illustrate this in figure 2.3.

The optical axis is parallel to z and we can see that one of the polarization directions will necessarily be perpendicular to it. Waves having this polarization are the so called ordinary waves. The waves having the other polarization direction are referred to as the extraordinary ones. A positive uniaxial crystal has $n_e > n_o$ and a negative uniaxial crystal has $n_e < n_o$. The equation for $n_e(\theta,\omega)$ is given, in cylindrical coordinates, by

$$\frac{1}{n_e^2(\omega,\theta)}=\frac{\cos^2\theta}{n_o^2(\omega)}+\frac{\sin^2\theta}{n_e^2(\omega,\frac{\pi}{2})} \tag{2.31}$$

We can have phase-matching in a positive uniaxial crystal when the angle θ_p is such that

$$n_o(2\omega) = n_e(\omega,\theta_p) \tag{2.32}$$

which implies

$$\sin^2(\theta_p) = \frac{n_o(\omega)^{-2}-n_o(2\omega)^{-2}}{n_o(\omega)^{-2}-n_e(\omega)^{-2}} \tag{2.33}$$

If the crystal is normally dispersive i.e. $n_o(\omega) > n_o(\omega')$ for $\omega > \omega'$, we see that $n_e(\omega) > n_o(\omega)$ is required for $\sin^2\theta_p > 0$ which, since $\sin^2(\theta_p) < 1$, implies that

$$n_e(\omega) > n_o(2\omega) \tag{2.34}$$

Practically, we set the pump beam to impinge onto the crystal as an extraordinary wave (the polarization is set to obtain this) at the angle θ_p. The second harmonic wave is generated as an

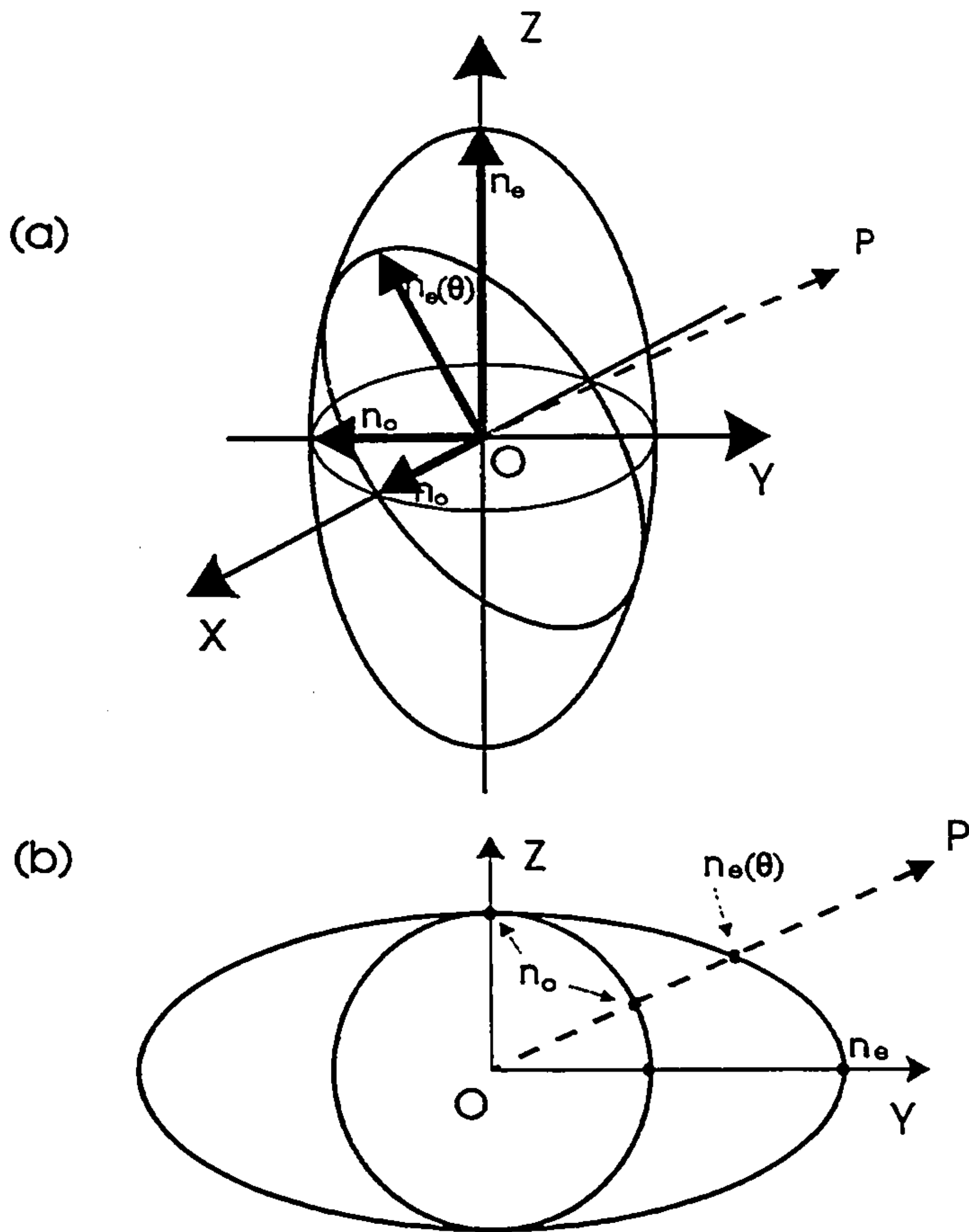

Fig. 2.3 (a) Three-dimensional index ellipsoid for a positive uniaxial crystal. (b) Normal surface for both the ordinary and extraordinary waves for a positive axis crystal. OZ is the optical axis. OP is the direction of propagation.

ordinary wave propagating also in the θ_p direction.

Descriptions of the LBO crystal used in SHG have been reported in the literature in recent years[2.10].

2.2.4 Synchronous pumping and pulse rejection

We have seen how to obtain a 532 nm mode-locked laser beam by pumping an LBO nonlinear crystal with the 1.064μm mode-locked beam of an Nd^{3+}:YAG laser. The pulse width of both original and frequency-doubled beam are of the order of 100 ps. We shall now see how much shorter pulses can be obtained by using the frequency doubled YAG to pump a dye laser.

The method uses direct modulation of the dye laser gain[2.11]. The fact that organic dyes exhibit efficient laser gain over a wide spectral region provides a mean to generate ultrashort laser pulses (refer to equation (2.9)). Thus, by pumping a dye laser whose cavity length is a multiple of a mode-locked pump laser cavity, we obtain mode-locked ultrashort laser pulses at its output (typically 5 ps at for a 630 nm wavelength pulse). This method is referred to as synchronous pumping.

The mode-locker used in our YAG laser produces pulses at a repetition rate of 76 MHz corresponding to a time interval of approximately 13 ns between each pulse. If one is interested in studying luminescent decay lifetimes having typical durations of a few nanoseconds, the 76 MHz repetition rate will not permit full

relaxation of the system before exciting it again. We must therefore reduce this rate and we achieve this by directing the output of our dye laser through a Conoptics Laser Modulation System Model 50 whose operation is based on the Pockel effect also called the electro-optic effect. Here, electrically induced birefringence is used to deflect some of the laser pulses so they do not participate in the sample excitation. By adjusting the frequency of the applied voltage to the output polarizer of our modulator's active element we obtain the desired repetition rate. For a full discussion of how this works and of the broader subject of modulation of optical radiation the reader is referred to the work of Yariv[2.12]. In our case, the periodicity of the applied voltage is such that the laser output pulses are reduced from 76 to 4 MHz.

2.3 Spectroscopy Instrumentation

In this section we will discuss the dispersion, detection and electronics aspects of the PL setup we have used.

2.3.1 Spectrometer

For the CW PL and PL lifetime decay measurements we have used a double 0.75 m Czerny-Turner spectrometer. The 1200 grooves/mm gratings, blazed at 500 nm give a reciprocal linear dispersion of ~5 Å/mm when operated in first order. However, we operate it with the exit slits removed and by coupling its output directly to a

two-dimensional microchannel plate photomultiplier tube which gives the coordinates of each photon event occurring at its photocathode. Details of the detector are given in the following sub-section. This setup permits dispersion of 120 Å over 25 mm (the diameter of the detector) thereby yielding a resolution better than 0.1 meV.

2.3.2 Low-light-level optical detection system

In recent years, there has been much interest in both linear and areal multichannel detectors. The advantage of these devices is their ability to spatially resolve and record photon events detected on their surfaces. The speed and ease of data acquisition made possible by these multi-element array detectors have propelled them into the field of optical spectroscopy with particular emphasis on the detection of extremely weak signals. The advantages and disadvantages of a large number of these multichannel detectors have been discussed[2.13]. One particular type of multichannel detector which is of interest to us is the microchannel plate (MCP) detector. These may be used to detect ion, electron and photon images. For visual output, one can use a phosphor screen at the output of the MCP detector. However, to take advantage of its high sensitivity, it is best to utilize it in a pulse counting mode which requires an electrical output. This output is obtained when the amplified electronic charge packet from the final plate of the MCP detector is deposited on a position-

encoding anode where it distributes itself amongst a number of output electrical contacts. The position of a particular event can thereafter be decoded by connecting these contacts to amplifiers and appropriate electronics which in turn yield analog and/or digital outputs of the event. Two kinds of position-sensing anodes exist: discrete conductor patterns which locate each event digitally[2.14] and others which yield a continuous variation in output with respect to the event location thereby yielding an analog position signal[2.15] . We will concern ourselves with the second category.

In this category of analog position signal anodes is the resistive anode (RA) variety. The principal advantage of MCP detectors is the simplicity of the anode itself and of the associated electronics[2.16]. Furthermore, the MCP-RA detector is capable of providing very accurate temporal information when used with standard time-correlated single photon counting (TCSPC) techniques[2.17] . This is due to the fact that the photocathode is in close proximity to the RA with no intervening electrostatic or magnetic lens system thereby reducing the electron transit time. The TCSPC technique is advantageous in measurements requiring a wide dynamic range and high-speed response as well as for measurements using a low-noise photon-counting detector. It has been reported[2.16] that by modifying the standard biasing circuit of a commercial MCP-RA detector, timing signals comparable to fast single channel photomultiplier tubes could be generated. By combining this with TCSPC circuitry, a very versatile PL data-

acquisition setup was developed combining the parallel collection capabilities of the MCP-RA detector with the ability to spectrally resolve the information into two adjustable time-windows. Recently, this approach was expanded[2.18] to enable either the simultaneous collection of 1024 decays for up to 1024 spectral channels (one-dimensional time-windowing) or the acquisition of four 512×512 channel time-gated two-dimensional images.

As stated previously in the introductory chapter, we have developed a low-light-level optical detection system capable of carrying out steady state (time-integrated) PL, PL decay, time-windowed PL, 2D PL imaging and finally 2D TR PL. Figure 2.4 shows the schematics of the micro-computer based acquisition setup, the optical detector and TCSPC circuitry used to obtain timing information with ~100 ps resolution.

The detector is an MCP-RA imaging photomultiplier tube (IPMT), Mepsicron™ model F4146M, manufactured by ITT/Surface Sciences Laboratories (SSL). This IPMT is a proximity focused device incorporating five MCPs arranged in a set of two plates with their faces in contact and a single potential across them (the V-plate) followed by a set of three plates also having their faces in contact and a separate single potential across them (the Z-plate). The 25 mm diameter multi-alkali photocathode of our Mepsicron is composed of Sb, Na, K and Cs (type MA3) and is cooled to -30 °C to reduce the dark count to less than 40 counts per second over the entire detector area or less than 0.00004 count per digital channel (1024x1024 channels). The quantum efficiency of the tube is better

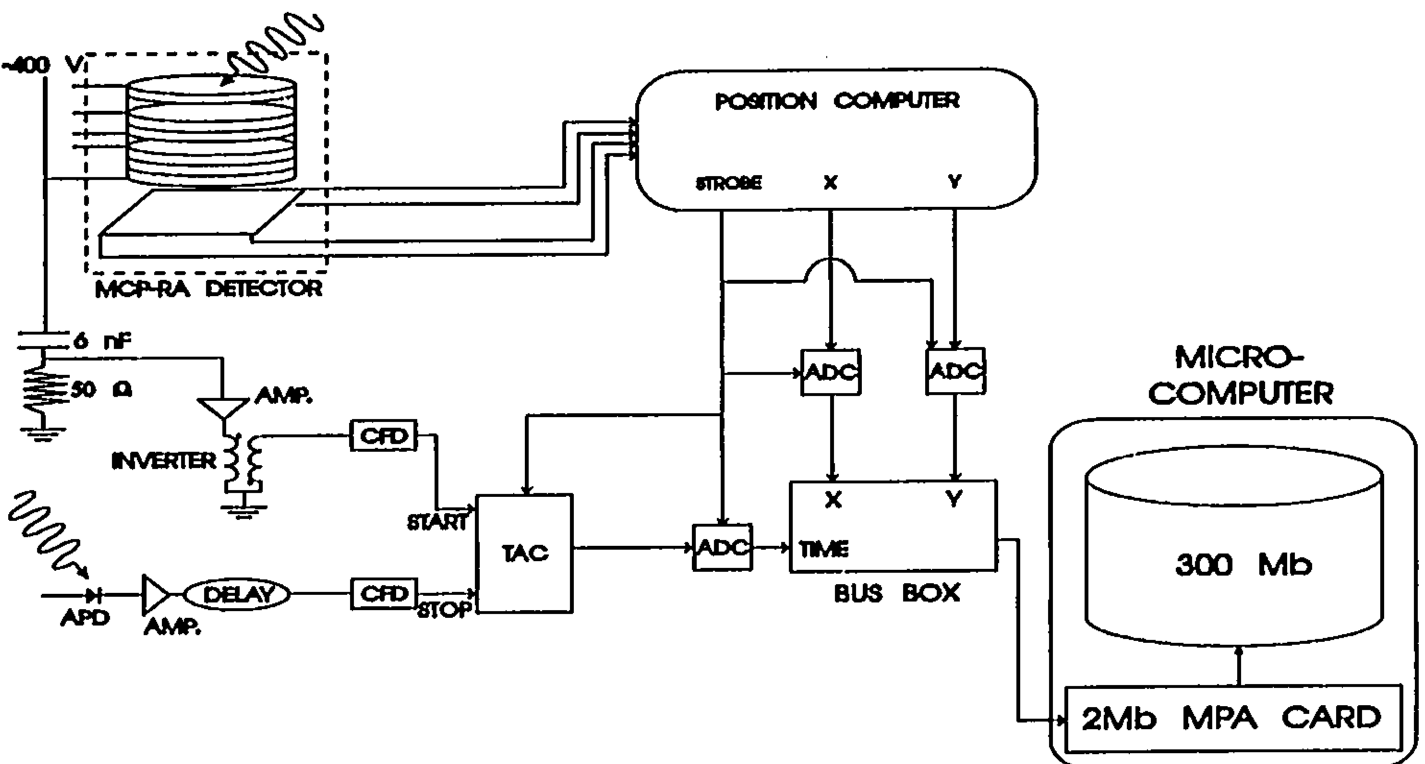

Fig. 2.4 Experimental setup showing the IPMT and its associated electronics together with the time-correlation circuitry. AMP.: amplifier, CFD: constant fraction discriminator, ADC: analog to digital converter, TAC: time to amplitude converter, APD: avalanche photodiode.

than 0.5% over the spectral range 400-900 nm with a total electron gain of approximately 10^6. The limiting spatial resolution of an event occurring on the surface of the F4146M is ~60 μm full width at half maximum (FWHM) over the 25 mm diameter.

Once the amplified charge packet from the final MCP is deposited on the position-encoding RA, it diffuses through the highly uniform resistive film towards four corner-located electrical collection contacts. The proportion of the total charge from each event reaching each corner contact is measured by charge sensitive pre-amplifiers and fed to the SSL 2401 position computer which converts the anode output into both analog and digital (10 bit numbers) X and Y coordinates. The position computer is designed to output only the location of events taking place inside a rectangular, electronically active area (distinct from the entire physical area of the sensor) whose size is determined by four front panel electronic gates. The preliminary alignment and the positioning of the event rejecting borders are achieved in real-time with the help of an oscilloscope that maps the IPMT on its screen.

The data acquisition is based on the Canberra MPA/PC Multiparameter System. It comprises a 33 MHz 80386 micro-computer as the host processor, an MPA/PC multiparameter 2 Mb card and a programmable external analog-to-digital (ADC) bus box which connects the MPA/PC adapter cord to three ADCs shown in Fig. 2.4. The 2 Mb capacity MPA/PC card is capable of storing and displaying a maximum of 1024x1024 channels. Word size is configurable from 1

to 4 bytes per channel. This system may be used in various acquisition formats which include the following:

(1) Single parameter format. Here, the data from up to three ADCs can be collected independently and that from any two ADCs may be displayed simultaneously. The memory acts as a histogram map of events which increments the corresponding channel by one every time an event is mapped into that channel. It is important that the product of the ADCs range settings (i.e. the number of channels into which the incoming signal is digitized) and the channel word size (which determines the dynamic range) be less than or equal to the 2 Mb capacity of the card. For example, in the CW PL experiments, we use only the X-ADC (corresponding to wavelength since the detector is placed at the ouput of the spectometer). If we set its range setting to the maximum 8K value, we can also set the word size to its maximum 4 bytes without overloading the memory card.

(2) Multiparameter format. In this case, the data of two ADCs can be collected in coincidence and displayed simultaneously in either colour-coded or isometric maps. Here again, the memory card acts as a histogram map of events, so restriction of the product of the ADC range setting and word size apply. For example, it is possible to store and display a maximum of 1024x1024 channels each having a 2 byte word size.

(3) List format. In this case, the memory card acts as a 2 Mb memory buffer. The coincidental data of the three ADCs is sequentially stored in the memory buffer and then off-loaded onto

the micro-computer's hard drive. Although the above restrictions do not apply in this format of operation, software must be written to construct files suitable for display. In our case, 2D time-windows are constructed from such list data. The list format effectively expands the real-time memory capacity to that of the micro-computer's hard disk.

Before presenting the optical part of our PL setup we present the system's various modes of operation in order of increasing complexity.

(a) Steady state PL. The simplest function of this setup is the acquisition of steady state PL spectra. To achieve this, the IPMT is placed at the output of our spectrometer (figure 2.5). Hence a PL signal from the sample is directed into the spectrometer and dispersed along the X direction of the IPMT. With only the X channel enabled (refer to Fig. 2.4) and the electronic Y-gates set to reject any event occurring outside the region onto which the input slits are imaged, the data is digitized and sent to the MPA/Multiparameter card. The software stores the incoming data in single parameter format. With only one position channel enabled, the histogram in memory directly reflects all of the events occurring along the Y axis at the corresponding X positions (proportional to wavelength at the output of the spectrometer). Hence, a plot of the stored histogram directly provides the time-integrated PL spectrum (example shown in Fig. 2.6 (a)).

(b) Time-resolved PL decay. The other one channel application of this setup is taking transient, spectrally gated, PL decay

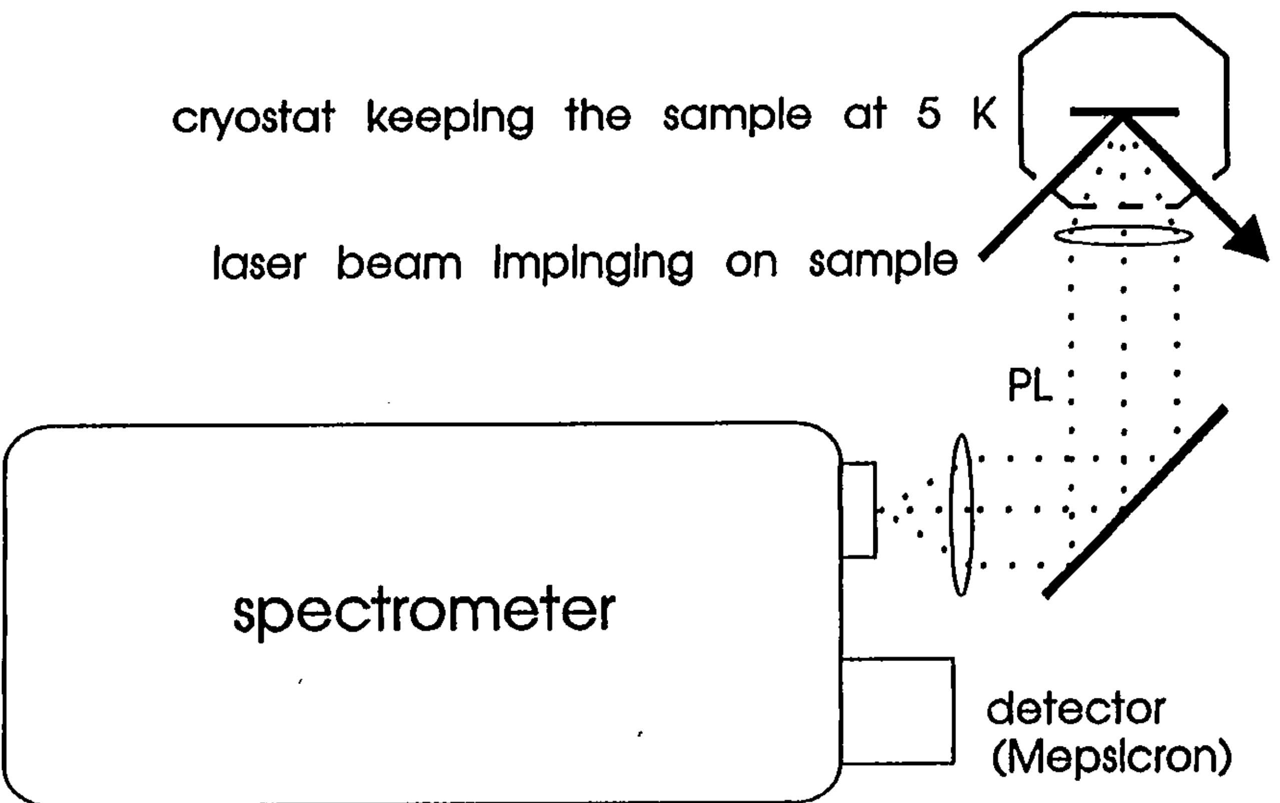

Fig. 2.5 Photoluminescence experimental setup used to carry out CW PL, PL lifetime decay and time-windowed PL. In the two latter cases, the exciting beam is generated by the frequency-doubled YAG laser synchronously pumping a dye laser.

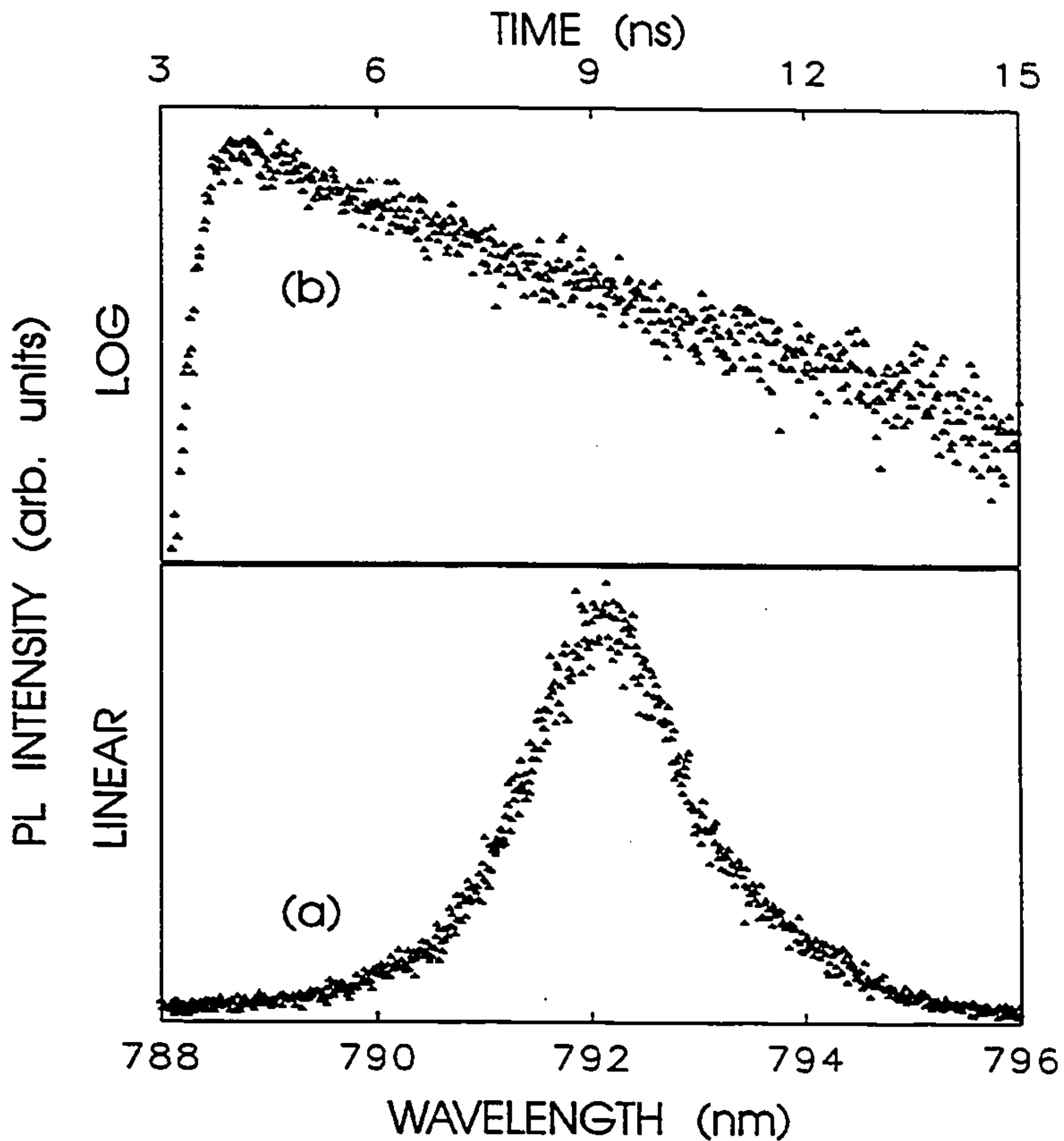

Fig. 2.6 (a) CW PL spectrum corresponding to the recombination of the n=1 heavy hole exciton of an AlAs/GaAs MQW structure having thirty 9.3 nm wide wells. (b) PL decay measurement which corresponds to the transition described in (a). The lifetime corresponding to the exponential decay is 5.3 ns. In both (a) and (b) the temperature was 86 K.

measurements. The technique employed in measuring such PL time-decays is called time correlated single photon counting. The PL signal is optically generated by a frequency doubled YAG laser synchronously pumping a dye laser. Using essentially the same setup as in Fig. 2.5, PL photons are directed towards the IPMT. As a photon strikes the photocathode, a transient positive voltage pulse develops across the 50 Ω resistor (Fig. 2.4). This pulse is amplified, inverted, and fed to a constant fraction discriminator (CFD) that generates the fast logic NIM start pulse for the time-to-amplitude converter (TAC). The TAC stop pulse is provided by sampling a portion of the exciting laser beam with an avalanche photodiode, the output of which is amplified and fed to a second CFD. A CFD's purpose is to let only pulses with specific heights reach the TAC. Apart from discriminating against ringing pulses generated by a true photon-generated pulse, it also eliminates those generated from electrons not originating from the photocathode since the height of these noise pulses is probably less than that of the pulses of interest. The TAC's purpose is to deliver an input pulse to a pulse-height-analyzer. The amplitude of this pulse will then be accurately converted to the time difference between the start and stop pulses. The stop pulses are delayed so that they arrive at the TAC sometime after the start pulse. In the setup of Fig. 2.4, the stop rate is the same as the laser repetition rate, whereas the start rate is much lower since a PL photon is not detected for every laser pulse. This choice of start pulse is much more efficient than the more intuitive reverse

choice since the TAC has a reset dead time of ~10 μs after each start-pulse-initiated cycle. Therefore, in the arrangement employed here, a TAC cycle is initiated only when a PL photon is detected, thus each photon contributes to the histogram of the decay. It should also be emphasized that for this time-resolved technique to be effective, the detection probability has to be kept below one PL photon per excitation pulse. This is necessary since the above method can only process one photon per excitation pulse, and distortions of the data would result if a significant number of photons were missed. Practically, this means keeping the PL count rate at a factor of 100-1000 below the laser pulse rate. This choice of operation is very well suited for weak PL signals having fast time decays. For transitions that have slow time constants, the reverse polarity (start-stop) has to be selected for maximum efficiency.

The spectral feature whose decay is to be recorded is selected by setting the spectrometer and the electronic gates of the position computer. The MPA card is again set to acquire data in the single parameter format (with the time-ADC enabled). The temporal range (i.e., the time interval to be digitized) is set on the TAC and should ideally be slightly longer than the lifetime of the signal being observed. The range setting of the MPA card can then be selected to balance the competing factors of minimum accumulation time and maximum temporal resolution. Thereafter, the histogram in memory records the total number of photon events at the selected wavelength, in the corresponding time interval. Fig.

2.6 (b) gives an example of this.

(c) Time-windowed PL. The next step in increasing complexity is enabling both X and time ADCs and acquiring in the multiparameter mode thereby recording entire time-resolved (time-windowed) PL spectra. Here, the timing signal is obtained as mentioned above. By selecting the proper time scale on the TAC and the number of time windows (via the time ADC range setting and the MPA software) so as to obtain the desired time window width, it is possible to observe the temporal evolution of the entire PL spectrum, in real time.

The time scale is chosen based on TR PL decay measurements as described previously. Then, the number of time windows is chosen so as to see the decay of the full spectrum with reasonable contrast and signal to noise ratio. Thus, the histograms in memory correspond to summing all events in two dimensional X (wavelength) Δt bins. Figure 2.7 shows such acquired PL spectra of a high quality InP sample. Here, we observe the free excitons (FE) and the biexctions (BIEX) peaks moving to lower and higher energies respec ively as the time after the passage of the exciting pulse increases[1.9]. This is attributable to the cooling of both FE and BIEX populations.

(d) 2D PL imaging. This mode of operation is attained by enabling both X and Y ADCs, thus permitting 2D mapping capabilities when the spectral resolution is set by a filter instead of a spectrometer. The system configuration is the same as in the time-resolved PL mode, except the time input is replaced with the Y

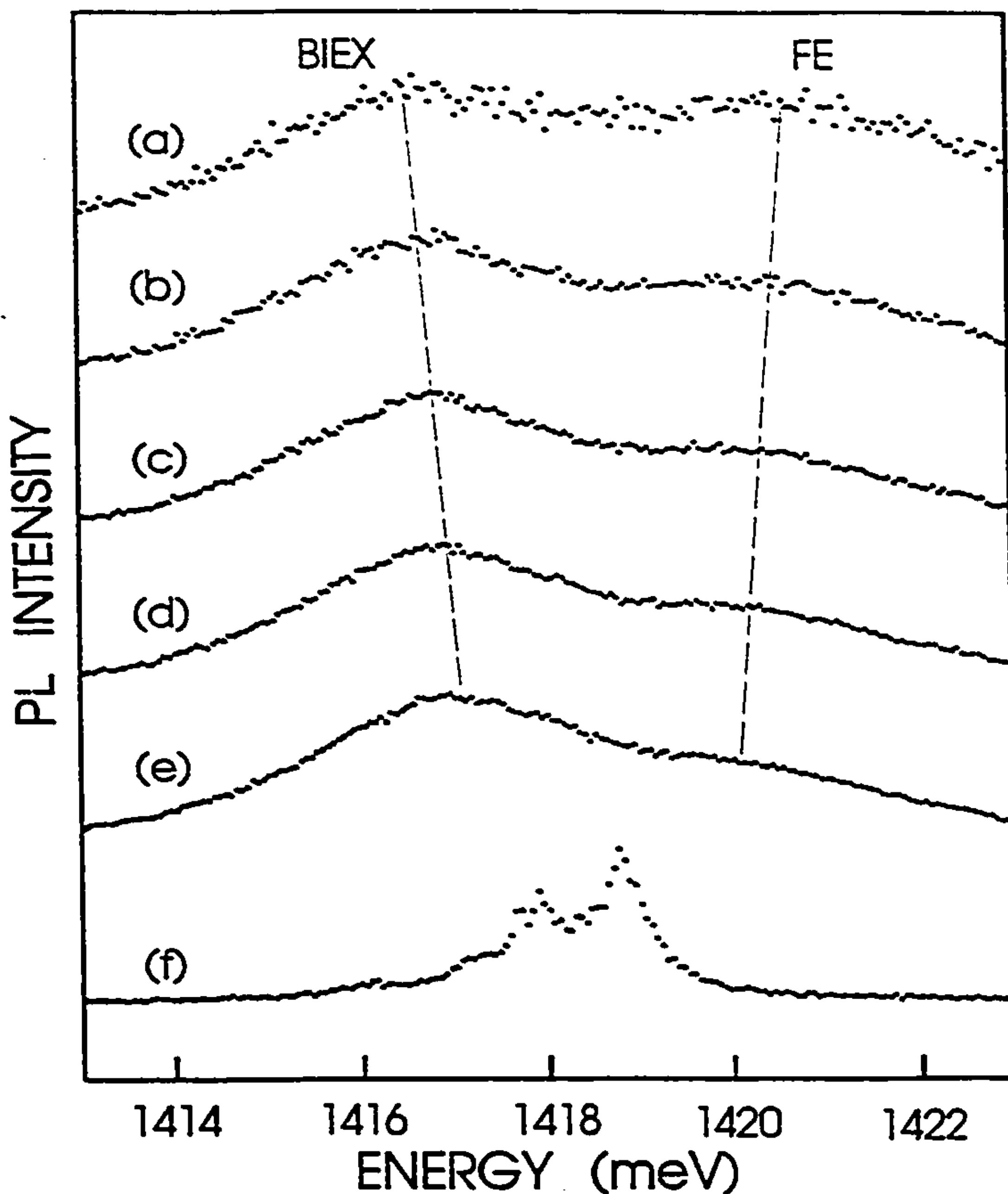

Fig. 2.7 Low temperature (5K) time-resolved spectra for the same InP sample as in Fig. 1.4. The average excitation density was 85 mW/cm^2. All time-windows are of 80 ps in width and evidence of biexcitons is seen by the peak shift from (a) through (e) i.e. as the temperature of both free exctions and biexcitons goes down. The time-domains are as follow: (a) 0-80 ps, (b) 80-160 ps, (c) 160-240 ps, (d) 240-320 ps, (e) 320-400 ps and (f) 2080-2160 ps. A thorough explanation of the features is given in Ref. 1.15. The lines showing the peaks shifting ((a) through (e)) are drawn to guide the eye.

input and the histograms in memory now integrate all events that occur at specific, real-space X and Y coordinates. A system of this sort has previously proven to be very effective in mapping out defects in semiconductor wafers[2.19].

(e) 2D time-resolved PL imaging. Finally, when used at its full potential, all three ADCs are enabled (X, Y and time) and the software is set to store the coordinates in list format. In this mode, each PL event corresponding to two position coordinates and one time coordinate are sequentially stored directly on the hard disk. The acquired file is then processed into 2D picture files producing the time-window data. This processing involved writing custom software to extract and sort the PL images in various time-windows and to create files that can be read and manipulated by the MPA software in the multiparameter mode (this final step is unnecessary if one is willing to write separate graphics drivers as well). The file processing time is a function of computer speed, the number of time windows, and the accumulation time (proportional to the data file size). For a typical 100 Mb file with 16 time windows, the processing takes approximately one hour for a 80386 33 MHz microprocessor. Figure 2.8 shows the optical setup used to acquire such data. The laser source is the same as the one used for time-resolved PL decay and time-windowed PL. The cryostat used in cooling the sample is, in the case of 2D TR imaging, a Joule-Thompson-effect-based MMR Technologies Cryogenic Microminiature Refrigeration System I operating on high-purity nitrogen. The lowest temperature attainable is thus approximately

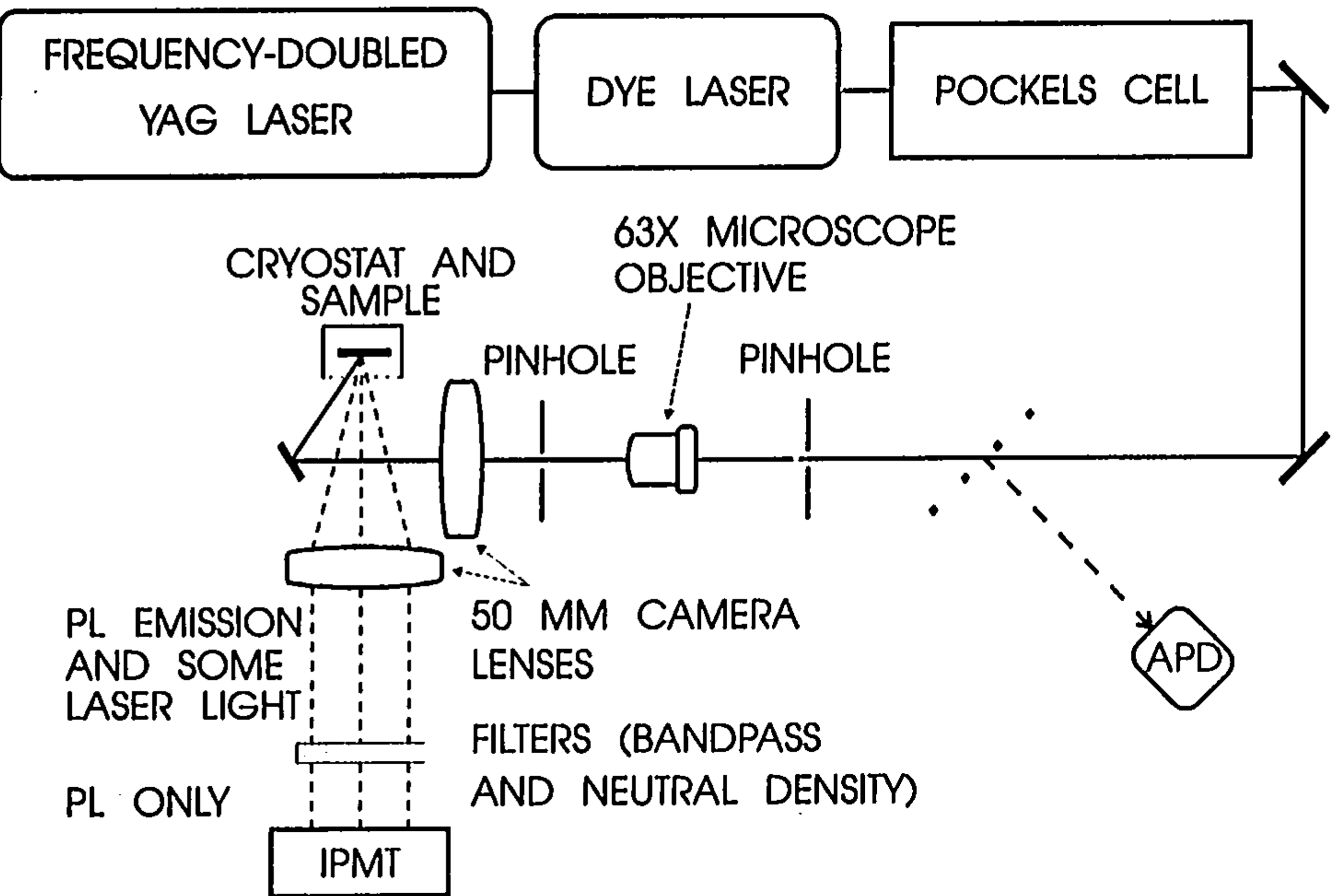

Fig. 2.8 Optical setup for the two-dimensional PL imaging. The 630 nm, 5 ps wide laser pulses are directed through a Pockels cell modulator where the repitition rate is reduced from 76 MHz to 4 MHz. The 63X microscope objective lens focuses the beam to a 5μm diameter and is imaged onto the sample.

80 kelvin. In all other modes of PL measurement at low temperatures, a Cryo Industries Model 8 CN liquid helium optical cryostat is used.

The laser pulses are focused to a 5 μm diameter on the sample surface and thus act as a localized source of electrons and holes whose subsequent expansion is monitored by the detection of the radiation emitted as they recombine. A more detailed discussion will be given in chapter 4.

2.4 Focused ion beam implantation

The disordering of our QW samples was achieved using a JIBL-104 ultra-high vacuum focused ion beam facility. Au^+, Ga^+ and Si^+ ions were implanted at energies of 100 keV. This FIB implanter has a FWHM of 70 nm and its beam profile is Gaussian to the 10% level, and no wider than twice the projected value at the 0.5% level. Furthermore, the beam angle is of the order of 4 mrad.[2.20] The geometry of the target stage and ion column is such that the implantation direction is normal to the epilayer surface (nominally 0° alignment angle). The implanted samples were annealed at 850 °C for periods ranging from 30 to 60 seconds in a N_2 atmosphere using a Heatpulse 410 rapid thermal annealer.

2.5 Samples

In this work, (In,Ga)As/GaAs and AlAs/GaAs QW structures were studied. The (In,Ga)As/GaAs QW structures were grown by molecular beam epitaxy in a Vacuum Generators V80H system, using solid sources of Ga, In, Al and As_4. These structures were capped with (Al,Ga)As to reduce surface recombination. The (Al,Ga)As and GaAs layers were grown at 605 °C at a growth rate of 0.7 µm/hour while the (In,Ga)As layers were grown after the substrate temperature was rapidly lowered to 565 °C. Growth at this temperature produces materials with high luminescence although desorption of In from the substrate makes a precise prediction of the composition difficult[2.21] .

The AlAs/GaAs sample was grown in a similar fashion.

Chapter 3

Ion Implantation

3.1 Introduction

The stopping of energetic ions in matter has attracted much experimental and theoretical attention during the last century.

The aim of this chapter will be to present results of PL measurements carried out on FIB implanted (In,Ga)As/GaAs strained quantum wells, with a view to investigate the feasibility of this technique for fabrication of nanostructures.

As an energetic ion impinges on a solid target, it will lose its kinetic energy through interactions with the atoms and the electrons of the target material. That is, most of the energy transfer will occur through the recoiling of the target atoms upon collision with the incoming ion and by the excitation of electronic states in the solid. This can create structural damage in the crystal by an amount which is generally assumed to be proportional to the energy transferred through atomic processes[3.1]. Studies of metals and semiconductors support this both theoretically[3.2] and experimentally[3.3].

The historically minded reader is referred to the writings of J.F. Ziegler[3.4] and of J.W. Mayer and coworkers[3.5] for an exhaustive look at the principles of ion implantation.

3.2 Focused Ion Beam

Ion beams impinging on a target provide a source of energy and of material. The ability to focus and steer such a beam by means of electric and magnetic fields adds further appeal to the science of ion implantation.

The use of focused ion beams in direct write lithography offers potential for greater resolution and resist sensitivity than do electron beams[3-6]. Furthermore, the ability to carry out direct doping without the requirement of resist deposition, exposure, development and removal offers reduced processing times which in turn provides rapid prototyping of devices[3-7]. Also, FIB sputtering capabilities by means of finely focused high energy ions allows for the direct micro-machining of materials[3-8] and can also act as a high resolution secondary ion mass spectroscopy (SIMS) source[3-9]. Micro-machining is also used for repairs of x-ray masks and integrated circuits[3-10].

On another front, the fabrication of quantum wires and boxes has been encouraged both by the desire for an improved understanding of dimensionally reduced systems and because of the possibility of novel electronic devices based on quantum size effects. Such nanostructures have been realized primarily through the use of conventional lithography techniques but focused ion beams have recently played an increasingly important role. Such FIB applications include the formation of quantum wires either by simple implantation into GaAs to create high resistivity boundary

regions[3.11] or by the selective etching of implantation-created amorphous regions to produce periodic structures[3.12]. In the AlGaAs/GaAs system, quantum well wires (QWW) have been created by implantation-induced compositional disordering[3.13]. That is, the quantum well sample is subjected to patterned implantation which disorders it. A subsequent annealing recrystallizes the sample while favouring the interdiffusion of the well and barrier materials thereby yielding compositional disordering (see Fig. 3.1). These QWW exhibited fine structure in photoluminescence excitation spectra which were attributed to the changes in the density of states caused by the confinement of carriers. One-dimensional channels controlled by a gate electrode have also been made using FIB implantation[3.14] while the formation of an antidot lattice has been reported by Ensslin and Petroff[3.15]. FIB implantation has also been used to introduce dopants into undoped AlGaAs/GaAs heterostructures to form 2D electron-gas structures[3.16].

3.3 Channeling Effects

Upon implantation into a crystalline target, ions might penetrate to a considerable depth if their incoming direction is parallel to one of the crystal's main axes. In such a case, one will find ions at depths that far exceed the ion range, R_p, predicted from Monte Carlo simulations (TRIM code)[3.17]. This is

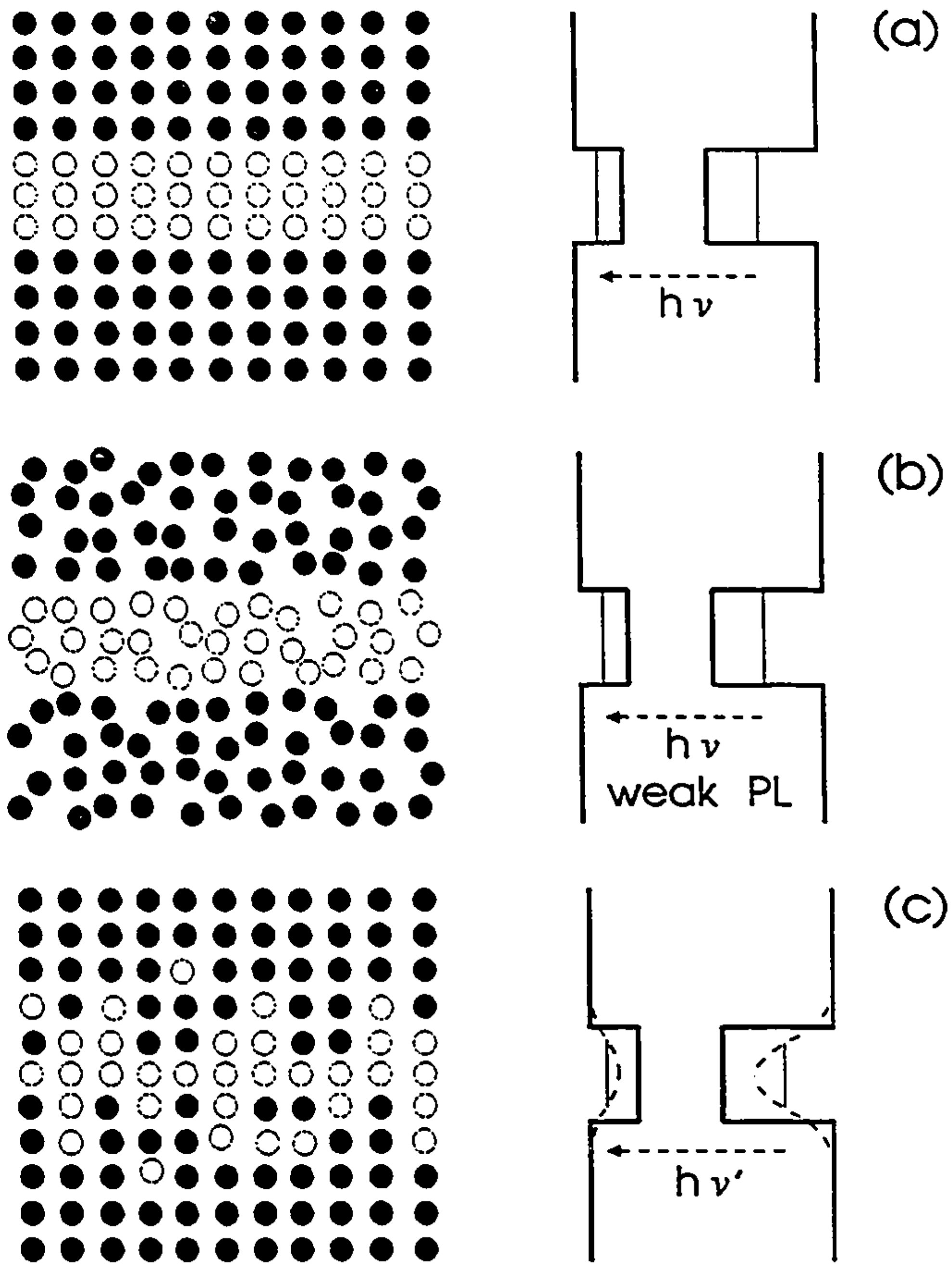

Fig. 3.1 Diagram showing the quantum wells crystal structure and band diagram. (a) QW prior to implantation, PL signal is strong; (b) Implanted QW prior to annealing. The crystal is partially disordered and the PL signal is weak; (c) QW after implantation and annealing, the PL signal is again strong and blue-shifted.

what is called channeling. The lateral straggling, ΔR_p, is defined as the half width at half maximum of the ion distribution centered at R_p.

As previously stated, patterned implantation through quantum wells and subsequent annealing to produce wires and dots has been demonstrated[3.13]. However, recent reports[3.18] have shown that this effect occurs at depths significantly beyond the expected range of the ions[3.19]. Petroff and co-workers[3.20] have used cathodoluminescence from GaAs quantum wells of different thicknesses located at depths as far as 500 nm below the surface to monitor the implantation effects of 50–150 keV Ga^+ ions (R_p – 60 nm and range straggling, ΔR_p, –28 nm). This study showed, by measuring the energy shift and the overall intensity of the luminescence, that changes occurred 500 nm below the surface. A number of possibilities were discussed[3.21], with ion channeling being proposed as a likely mechanism[3.22]. One supplier of FIB equipment has considered channeling as a potential problem[3.23], and offers the option of doing the implantation at an angle to the surface normal.

Somewhat surprisingly, there has been resistance to the idea that ion channeling is the mechanism responsible for deep disordering. To clarify this issue, we have grown a test structure containing four 3.0 nm thick, strained $In_xGa_{1-x}As$ quantum wells of differing nominal composition (x = 0.10, 0.15, 0.20 and 0.25) located at varying depths from the surface (50, 100, 250 and 450 nm respectively), see figure 3.2. As previously mentionned in section

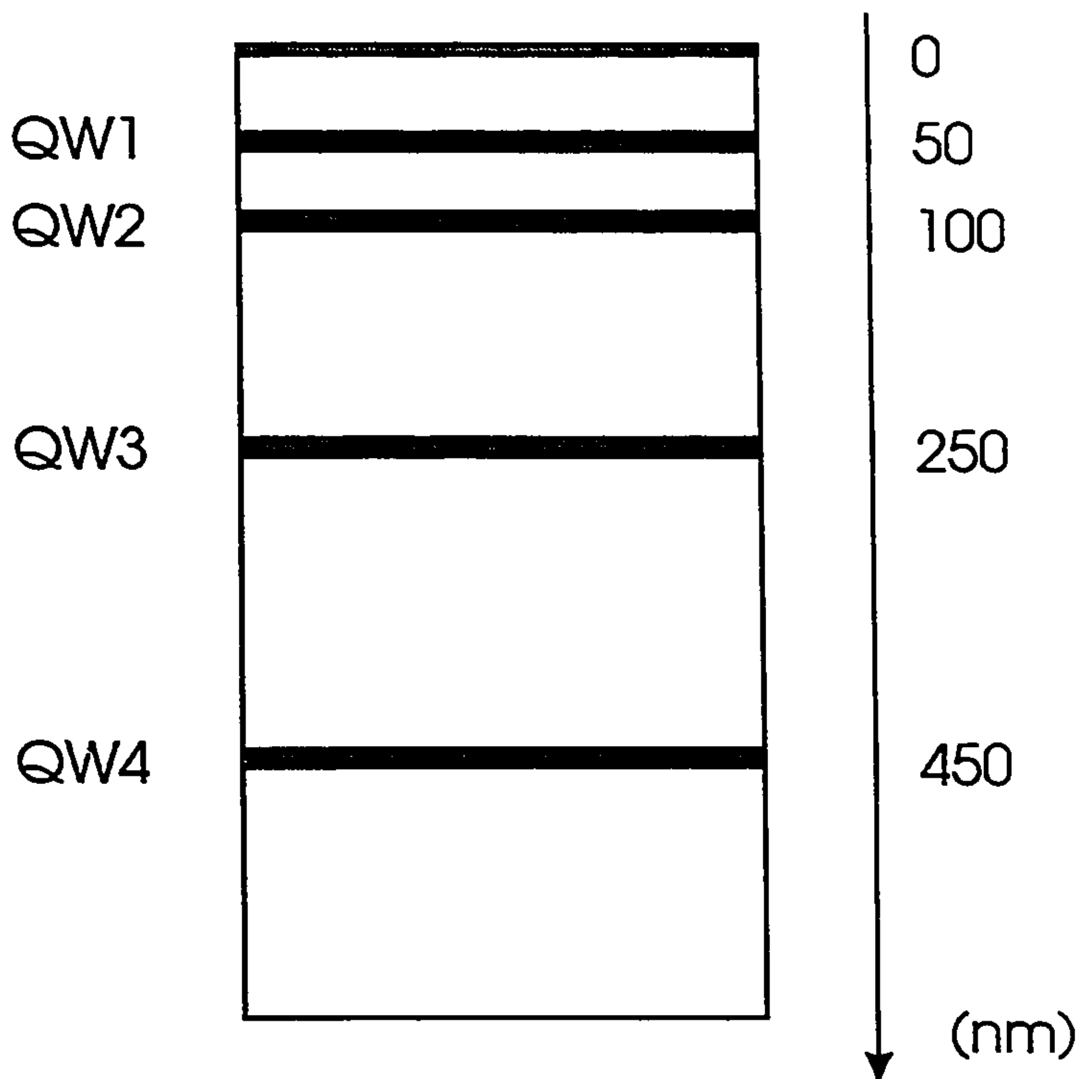

Fig. 3.2 Cross section of the quantum well samples studied. The well material is InGaAs while the barrier material is GaAs. The well widths are all 3.0 nm. The indium concentration is 10, 15, 20 and 25% for both type of samples whose difference lies in the ordering of the wells. The capping layer is 30% AlGaAs reducing surface recombination.

2.5, the sample was capped with 15 nm of $Al_{0.3}Ga_{0.7}As$ to reduce surface recombination. A second structure with the same nominal compositions and thicknesses but with the order of the quantum wells reversed, was grown to confirm that none of the effects observed were due to the particular ordering. The samples were grown by solid source molecular-beam epitaxy using Ga, In, Al, and As_4. GaAs and AlGaAs were grown at 605 °C at a growth rate of 0.7 µm/h, while the InGaAs was grown after the substrate's temperature was lowered rapidly to 565 °C. Growth at this temperature produces materials with high luminescence[3,24] although desorption of In from the substrate makes a precise prediction of the composition difficult. We will discuss the determination of the composition in a later section.

Two different implantation facilities were used in this study. First, a JIBL-104 ultrahigh vacuum FIB was used to implant uniform areas (250 µm X 250 µm) with 100 keV Au^+ ions obtained from a Au-Be-Si source. A current of 14 pA with a beam diameter of ~70nm was used to implant doses ranging from $3x10^{12}$ to $6x10^{13}$ ions/cm^2. The geometry of the target stage and ion column is such that the implantation direction is normal to the epilayer surface (nominally a 0° alignment angle, i.e. the sample holder's orientation is not excatly parallel to the crystal's <100> axis). Second, on pieces from the same wafer, 250 keV Au^+ ions from a 1.7 MeV Tandetron were implanted using a five-axis target stage, which permits precise orientation of the substrate with respect to the trajectory of the Au ions. The orientation of the epilayer was determined by

measuring the Rutherford backscattering yield of 1 MeV He ions from a different area of the same sample[3.25] as a function of tilt and azimuthal angle. Implantations were done with the Au beam parallel to the surface normal (similar to the FIB implant), at 4° and 12° to the surface normal, and into the aligned ⟨100⟩ axis. Finally, an implantation was also done through a 20 nm Si_3N_4 cap at the nominal angle of 0°. The samples were rapid thermal annealed (RTA) at 850 °C for 60 seconds in a N_2 atmosphere, using a Heatpulse 410 RTA to initiate the compositional disordering of the quantum wells and remove nonradiative recombination sites. The sample surfaces were protected during annealing by placing a second, larger piece of GaAs on top of them.

The obvious advantage of implanting Au^+ ions into GaAs (instead of Ga^+ [3.20]) is that the depth distribution of ions for the different alignments can be obtained directly by SIMS. In this case, a Cameca IMS-4f ion microprobe was used with 10 keV Cs^+ ions (14.5 keV net-impact energy) for sputtering, while Au^{197} negative ions were detected. We have used PL (HeNe laser excitation source) with the sample held at 5 K, to probe the changes in composition and width of the quantum wells by monitoring the energy shifts and fitting these with a model to be described later. The resolution of this PL system described in chapter 2 is better than 0.1 meV and is more than sufficient to measure the energy shifts of the quantum wells luminescence. In addition, implanted areas were compared to as-grown areas on either side to avoid problems due to possible inhomogeneities caused by deposition variation across the

sample during growth.

Figure 3.3 shows the depth distribution of the 100 keV Au ions (R_p - 27 nm, ΔR_p - 10 nm) as implanted by FIB at a nominal angle of 0°. Immediately obvious is the long tail of the distribution which extends through the third quantum well (250 nm below sample surface) with a small fraction reaching the fourth quantum well (450 nm below sample surface). This is a distance twenty times that of R_p and much larger than $R_p + \Delta R_p$. Also noteworthy is that the number of ions in the tail is essentially independent of the dose for the two doses shown. This effect can be understood in terms of channeling[3.26]. Even for a "perfectly" aligned beam, there is a substantial amount of dechanneling of the Au ions in the near-surface region. As the implantation proceeds, the damage created by the dechanneled ions increases the dechanneling rate until no further ions are channelled deep into the bulk. This self-limiting process leads to a saturation of the damage created at greater depths, and therefore, to a saturation in the shift of luminescence, as observed previously[3.27]. As can be seen in figure 3.4 (a), the general shape of the distribution of the 250 keV Au ions (R_p - 51 nm, ΔR_p - 18 nm) implanted with the crystal aligned along the normal <100> channel is similar to that of Fig. 3.3 with the mean range and the depth of penetration of the channelled ions shifted to greater depths because of the higher energy (250 Vs. 100 keV). Note, there is no evidence in these SIMS profiles of an increased yield of the Au negative ions due to matrix effects in either the InGaAs layers or the Si-doped

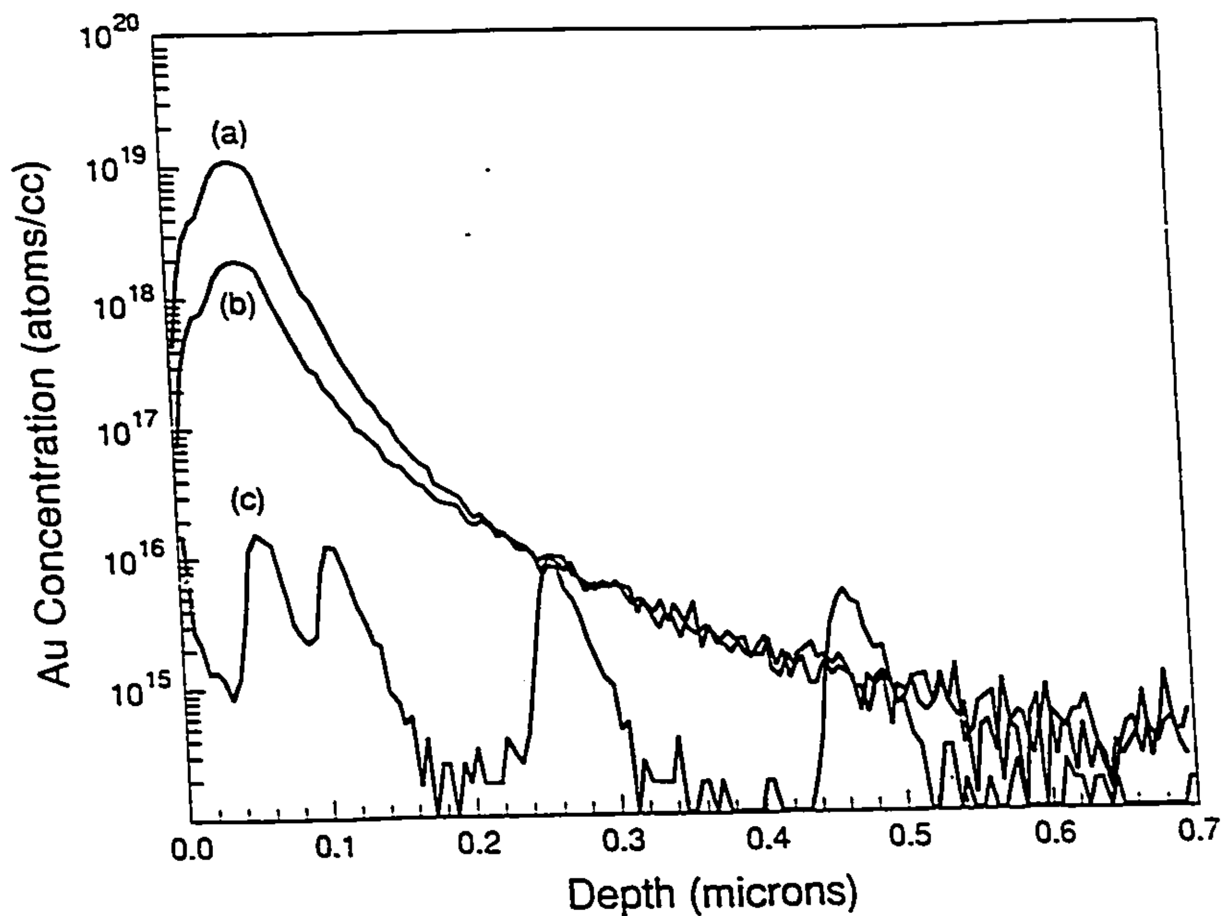

Fig. 3.3 The depth profile of the 100 keV Au^+ ions implanted using an FIB at nominal 0° into the InGaAs/GaAs structure. The distribution was measured by SIMS using a 10 keV Cs^+ beam for sputtering while ^{197}Au negative ions were detected. Two different doses are shown: (a) 5.5×10^{13} ions/cm^2; (b) 1.1×10^{13} ions/cm^2. This illustrates the saturation of the channeling in the tail. The indium distribution, curve (c), is shown in arbitrary units and serves to confirm the depth scale.

substrate (0.9 μm). The intensities of the luminescence from the quantum wells were greatly reduced (5 orders of magnitude when compared to the virgin material) and no shift in energy was observed for the various peaks.

Upon annealing, the situation changes drastically, as shown in Fig. 3.4(b). First, Au has diffused throughout the entire epilayer into the substrate. The sudden increase in Au concentration observed at the epilayer/substrate interface (0.9 μm) is due to some change in the diffusion mechanism. This feature allows us to estimate that over one third of the original implant has diffused into the substrate after only 60 seconds of RTA. Second, Au has accumulated in all four InGaAs quantum wells, also probably because of a change of diffusion mechanism at the well/barrier interfaces. We were not able to obtain any significant luminescence intensity from the first two quantum wells for any implant discussed here because of either complete disordering, and/or incomplete removal of nonradiative sites. Energy shifts in the PL were now observed from the third and fourth quantum wells after annealing, indicative of changes in the composition and width, see Table III.I (a simple model explaining this will shortly be presented). As observed previously[3.28], the energy shifts saturated after the 60 second anneal. The intensity was comparable to the pre-implanted levels. The question remaining is: was the compositional disordering caused (enhanced) by the point defects created by the implantation of the Au ions, or was it simply due to the rapid thermal diffusion of the Au through the quantum well?

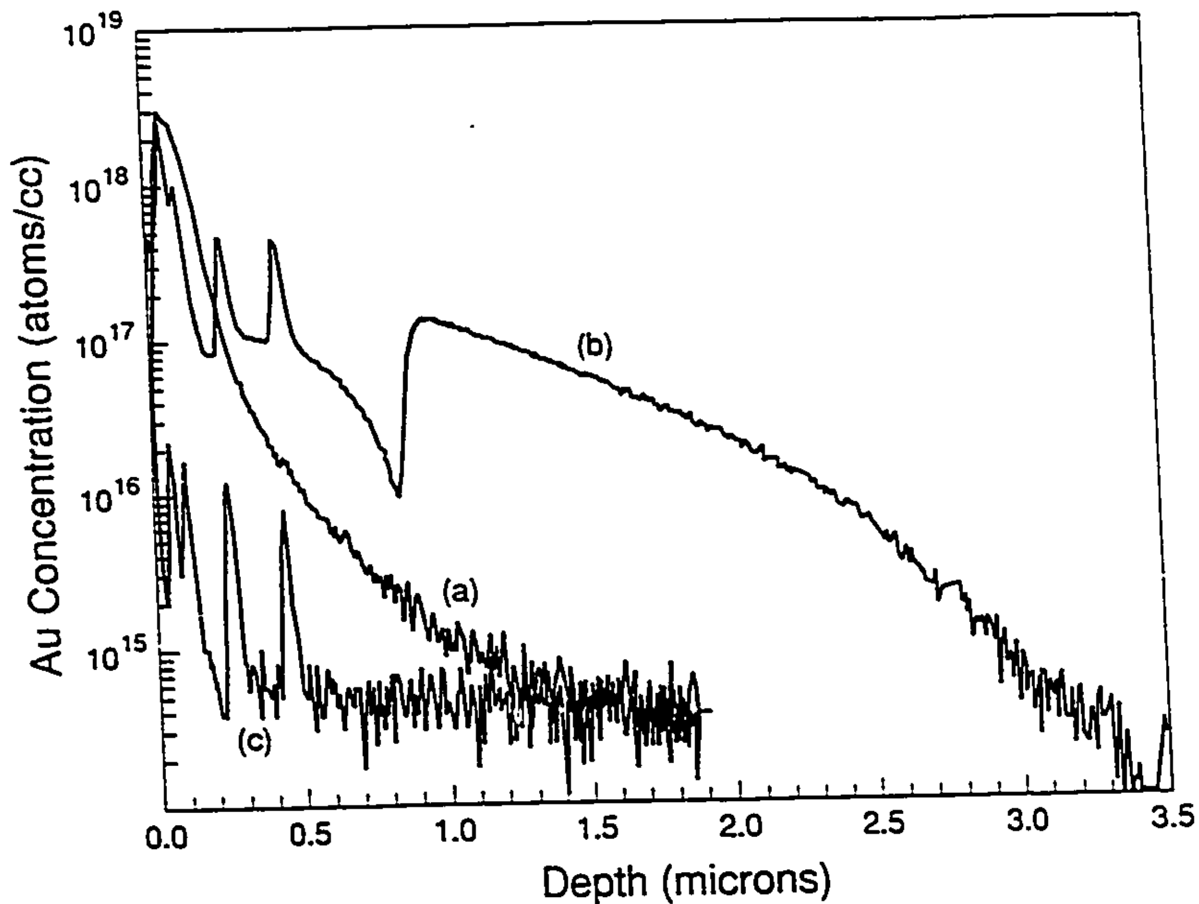

Fig. 3.4 The depth profile of 250 keV Au ions (5×10^{13} ions/cm^2) implanted into the test structure along the <100> channel before (curve (a)) and after (curve (b)) an RTA at 850°C for 60 seconds. The epilayer/substrate interface is at 0.9 µm. Measurement conditions are similar to Fig. 3.3. Again the In distribution (curve (c)) is in arbitrary units.

Comparing the depth distributions, after annealing, of the 4° off-normal implant and the aligned <100> axial implant, figures 3.5(a) and (b) respectively, it is clear that the extent of rapid thermal diffusion of the gold is similar in both cases. This is indicated by the comparable Au distributions at depths larger than 0.9 µm. Table III.I shows however that the energy shifts observed in the third and fourth quantum wells are strongly dependant of the implantation angle, demonstrating that this rapid thermal diffusion cannot be responsible alone for the observed disordering effects.

As discussed previously, a change of the alignment angle between the Au^+ ion beam and the crystal orientation drastically affects the depth distribution of the implanted ions. In figure 3.5(a) and (b), we observe significant differences in the amount of Au which has accumulated in the quantum wells. For the 4° implant, the accumulation of Au and the shift in the PL energy in the fourth quantum well (Table III.I) is much smaller than that in the <100> implant. This result is consistent with the significantly reduced number of Au ions which reached the fourth QW during the original implantation at 4°, i.e. reduction in channeling[3.26]. This resulted in fewer point defects being created in the vicinity of this quantum well and, subsequently, in less disordering upon annealing. The third QW of the 4° implant also shows the same trend (a reduced energy shift and Au accumulation) when compared to that of the <100> implant, but the differences are not as great. This again demonstrates that the amount of disorder depends on the amount of damage created by the original implant. As expected, these same

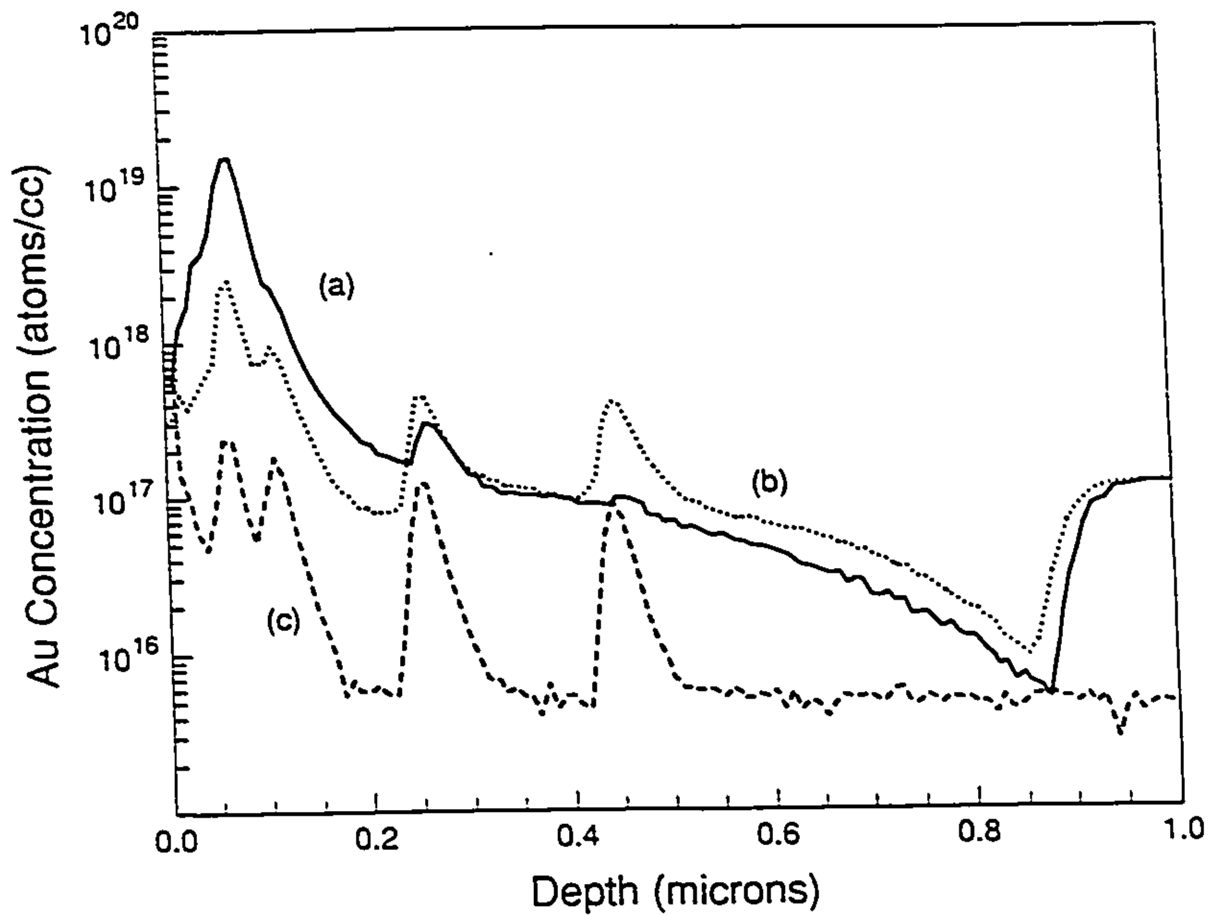

Fig. 3.5 The depth profile of 250 keV Au ions implanted into the test structure at 4° off-normal (curve (a)) and along the <100> axis (curve (b)) after an RTA at 850°C for 60 seconds. Measurements conditions are similar to those of Fig. 3.3. Again, the In distribution (curve (c)) is in arbitrary units.

TABLE III.I Energy shift (meV) of QW luminescence after implantation-induced disordering.

Alignment	QW3 (250 nm)	QW4 (450 nm)
as-grown	1467.5 meV	1488.6 meV
<100> axis	10.8 meV	4.5 meV
nominal 0°	7.2 meV	3.2 meV
4° off-normal	5.7 meV	1.1 meV
12° off-normal	1.3 meV	0.9 meV
nominal 0°, 20 nm Si_3N_4	1.1 meV	0 meV

observations were magnified for the 12° off-normal implant. Similar effects were observed for the sample with the order of the quantum wells reversed.

The channeling process should also be suppressed by implantation through an amorphous layer[3.26]. For the implant through the 20 nm Si_3N_4 cap, the effects observed by either SIMS or PL are more pronounced than for the 12° off-normal data. Significantly fewer ions channelled (due to the multiple scattering which occurs in the cap layer), with no accumulation of Au in the fourth QW. Again, these results are consistent with the PL, which shows no change in the fourth QW, and very little in the third QW. As expected, the first and second quantum wells were completely disordered.

The above clearly demonstrates that channeling effects[3.22] must be taken into account in FIB implantation. Compositional disordering of the quantum wells occurs only if implanted Au ions reach the layer during the implantation to create a reservoir of

point defects. The disordering is not due to thermally diffusing Au. Ions other than Au should yield quite similar conclusions in the sense that the damage delivered will occur mostly through atomic collisions regardless of the ion specie.

3.4 Wires and Boxes: An Attempt

In this section, we report on the initial investigations of the compositional disordering of the strained (In,Ga)As/GaAs QW structures (described in the preceding section) with emphasis on the eventual fabrication of QWW and quantum well boxes (QWB) which would exhibit confinement effects.

Following the Laruelle and co-workers[3.29] study of AlGaAs/GaAs structures, the FIB implantations were made at a nominal 0° with respect to the surface normal and without an amorphous Si_3N_4 cap, to permit channeling of the implanted ions[3.30]. Because of the limited energy of FIB facilities, channeling is required if ion-induced effects are to be utilized at large depths. More important, it has been reported that channeling reduces the lateral ion straggling and makes it easier to form nanostructures[3.31]. Hirayama[3.32] has shown that the interdiffusion depends linearly on the dose for values less than 10^{14} ions/cm^2 in the AlGaAs system. In such AlGaAs/GaAs studies, it was the thickness of the GaAs QW layers which was varied in the different growths since the QW was the binary (material made up of

two atomic constituents i.e. GaAs) and hence the only sensible parameter to vary (not the well indium concentration as in the present work) and the layers also contain insignificant strain. Under such circumstances, the defect creation probability will not vary from QW to QW and should scale linearly with dose. However, for systems in which the quantum wells vary in composition or are strained, the defect production is expected to vary from well to well as will be shown in what follows. For example, selective amorphization of the strained layers by ion bombardment has been observed in the Si/SiGe/Si (100) system[3.33]. In addition, intermixing of heteroepitaxial interfaces has been shown to be dependent on the amount of strain[3.34]. A priori, it is not at all obvious that the conclusions drawn for the AlGaAs/GaAs system will be the same as for the strained InGaAs/GaAs system.

The two InGaAs/GaAs structures studied and previously described nominally differed in the ordering of their quantum wells only. The one named #1020 has its topmost well composed of 10% (nominal) indium while the underlying ones are made of 15, 20 and 25% indium in order of increasing depth. The structure named #1021 has the same QW nominal indium compositions but had the order of the wells reversed. This was done to disentangle the dependence of the dose delivered at a particular depth from variations in QW composition.

The actual compositions of the as-grown InGaAs quantum wells were determined using Rutherford backscattering spectroscopy (RBS) of 2 MeV helium ions and/or 20 MeV oxygen ions[3.25]. For the case of

the 20 MeV oxygen ions, the RBS yield from all four InGaAs quantum wells could be separated from the GaAs signal which allowed the compositional ratio of the quantum wells to be determined precisely. The yield from either sample was converted to an areal density (In atoms/cm^2) using the stopping power of oxygen in GaAs[3.35]. The accuracy of this areal density was improved by measuring the In content of the two uppermost quantum wells in each sample using 2 MeV helium ions. In this case, the In areal concentration was obtained through the use of a secondary standard (Bi implanted silicon of known dose[3.36]). The relative concentration error was estimated to be ±7%. The width of each QW was measured to be 3.0 ± 0.3 nm from cross-sectional transmission electron micrographs[3.37]. Combining this with the measured In content, the In concentration (%) was determined and is reported in Table III.II (sample 1020) and Table III.III (sample 1021). Note that, as expected, the actual concentrations were less than nominal due to In desorption from the surface during growth.

Again, implantation was carried out using NRC's JIBL-104 UHV FIB facility. 100 keV Ga^+ ions were implanted at a constant 40 pA current to get doses ranging between 0.6 to 11.0x10^{13} ions/cm^2 in both samples 1020 and 1021. The beam profile is Gaussian to the 10% level (FWHM ~70 nm), and no wider than twice the projected value at the 0.5% level[3.38]. The geometry of the target stage and ion column is such that the implantation direction is normal to the epilayer surface (0° nominal alignment).

For each of the five implant doses, three different patterns

of implantation were made. First, to act as a reference, a broad area of 250 μm x 250 μm was implanted. Second, to attempt creation of QWW of different lateral dimensions, four sets of 50 uniform rectangles (100 x y μm^2, where y = 0.4, 1.2, 1.6 and 1.8) were implanted and each was separated from its neighbours by an unimplanted rectangle (100 x (2-y) μm^2). In this way, four

TABLE III.II Comparison of the nominal indium concentration in the as-grown quantum wells for sample 1020 with the concentration determined from RBS measurements and by fitting PL transition energies. The error bars show lateral variation of the PL and the resulting calculated composition across the wafer. The error bars on the RBS do not include any contributing error from the determination of the QW width by transmission electron microscopy (TEM).

	Depth (nm)	PL (meV)	Nominal (%)	RBS determined (%)	Calculated from PL (%)
QW1	50	1493 ± 1	10	6.5 ± 0.5	7.0 ± 0.15
QW2	100	1475 ± 1	15	10.4 ± 0.7	10.3 ± 0.15
QW3	250	1448 ± 1	20	14.0 ± 1.0	14.7 ± 0.15
QW4	450	1426 ± 1	25	17.7 ± 1.2	18.0 ± 0.15

TABLE III.III Comparison of the nominal indium concentration in the as-grown quantum wells for sample 1021 with the concentration determined from RBS measurements and by fitting PL transition energies. The error bars show the lateral variation of the PL and the resulting calculated composition across the wafer. The error bars on the RBS do not include any contributing error from the determination of the QW width by TEM.

	Depth (nm)	PL (meV)	Nominal (%)	RBS determined (%)	Calculated from PL (%)
QW1	50	1416 ± 3	25	20.5 ± 1.4	19.6 ± 4.5
QW2	100	1439 ± 1	20	16.2 ± 1.1	16.3 ± 0.15
QW3	250	1467 ± 1	15	11.2 ± 0.8	11.7 ± 0.15
QW4	450	1488 ± 1	10	6.9 ± 0.5	8.1 ± 0.15

different areas, 100 x 100 μm^2, were created (see Fig. 3.6(a)). Finally, to create QWB of different dimensions, another area of the wafer was implanted as above and then additional implants were placed between the original rectangles to create intersecting rectangles but without any area of the surface receiving a double dose of ions. Thus, for each dose, there was a broad area implanted region, four sets of wires, and four sets of boxes of differing dimensions (Fig. 3.6(b)). The samples were then annealed as described in the previous section. As mentionned, we used the shift of the peak of the PL from each QW to monitor the compositional disordering.

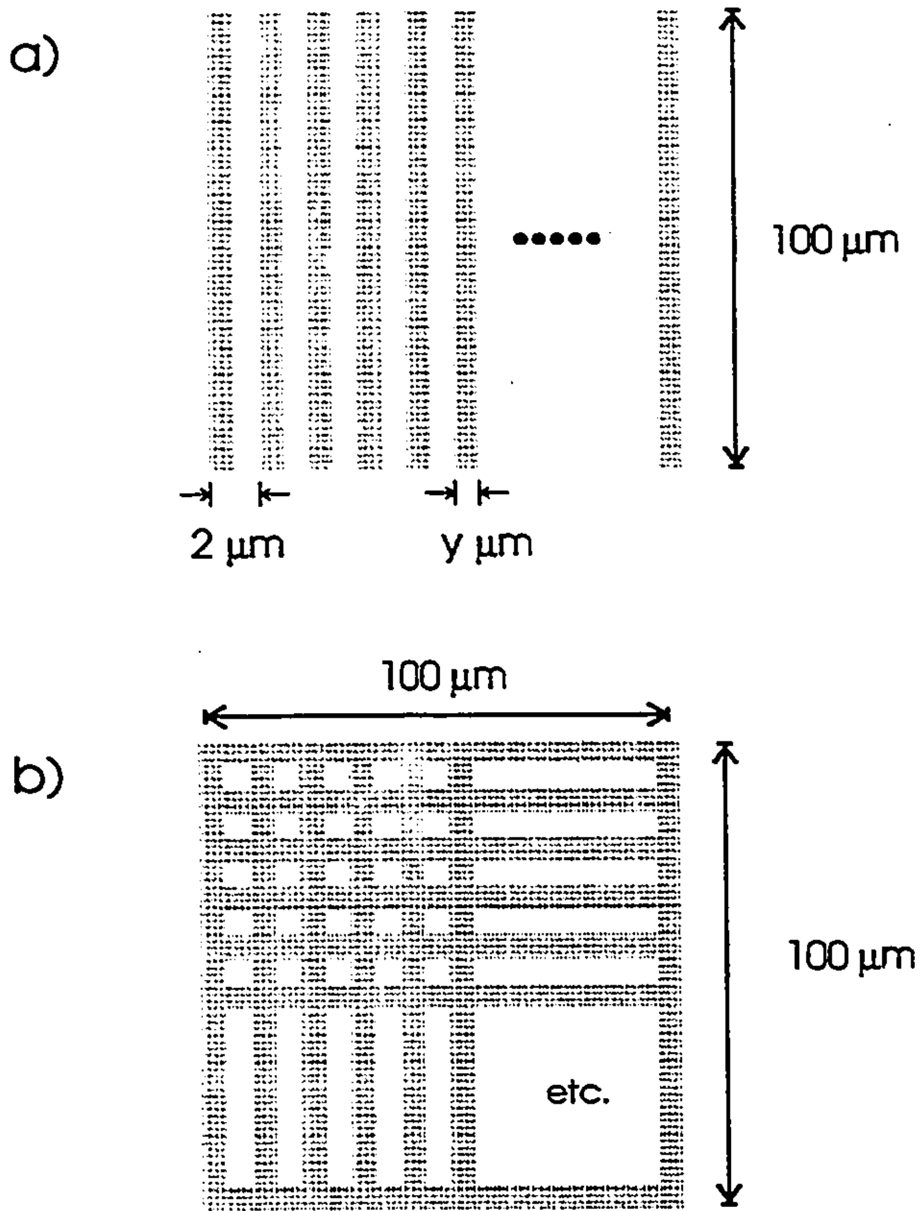

Fig. 3.6 Diagram showing the wire (a) and box (b) implantation patterns used in the study. The implantation rectangle width (y) has the value 0.4, 1.2, 1.6, and 1.8µm.

3.4.1 Interdiffusion lengths

The calculations were performed within the envelope function approximation including the effects of strain in the $In_xGa_{1-x}As$ layers by way of band-gap shifts[3.39] but neglecting strain dependencies in the effective masses. We ignored valence-band coupling and calculated all the eigenenergies within a single band scheme by the numerical integration of Schroedinger's equation in one dimension. The above approximations should be adequate since we were dealing mainly with energy shifts. As will be shown below, the calculated absolute transition energies were in good agreement with experiment.

The strain-dependent electron/heavy-hole and electron/light-hole band gaps for an $In_xGa_{1-x}As$ layer at low temperature (5K) are given by[3.40]

$$E_g^{hh} = E_g^o + \delta E_H - \delta E_s \tag{3.1}$$

$$E_g^{lh} = E_g^o + \delta E_H + \frac{\delta E_S}{2} + \frac{\Delta_o}{2} - \frac{1}{2}(\Delta_o^2 + 9\delta E_S^2 - 2\Delta_o E_S)^{1/2} \tag{3.2}$$

where, in meV, $E_g^o(x) = 1519.2 - 1594x + 485x^2$ is the unstrained band gap and $\Delta_o = 340 - 94x + 144x^2$ is the spin-orbit splitting. The hydrostatic pressure shift δE_H and uniaxial stress-induced valence-band splitting δE_S are given by

$$\delta E_H = 2a[(C_{11} - C_{12})/2]e \tag{3.3}$$

and

$$\delta E_S = b[(C_{11} + 2C_{12})/C_{11}]\epsilon \qquad (3.4)$$

where a and b are the interband hydrostatic pressure and uniaxial deformation potentials, C_{ij} are elastic constants, and $\varepsilon = (a_o - a_x)/a_x$ is the biaxial strain in the layer calculated from the lattice constants a_x for $In_xGa_{1-x}As$ and a_o for GaAs. All these quantities were obtained by linear interpolation between GaAs and InAs values[3.39] at 4 K.

The longitudinal effective masses (normal to the layers) for the electron, heavy, and light holes in the $In_xGa_{1-x}As$ layer were taken to be

$$\begin{aligned} m_e &= 0.067 - 0.044x \\ m_{hh} &= (\gamma_1 - 2\gamma_2)^{-1} \\ m_{lh} &= (\gamma_1 + 2\gamma_2)^{-1} \end{aligned} \qquad (3.5)$$

where the Lüttinger parameters γ_1 and γ_2 were also obtained by linear interpolation.

For all In compositions studied at low temperatures here, light holes are not bound within the well and no optical transitions from light hole levels to the electron levels were observed experimentally. We therefore considered only transitions from the heavy-hole states.

Interdiffusion normal to the wells was included using the model of Cibert and Petroff[3.41]. Before ion implantation the band profile is close to that of a square well of width w as illustrated in figure 3.7(a). After annealing, the indium fraction in a broad-area-implanted region as a function of position z in the well was assumed to be given (in the limit of long anneal time) by

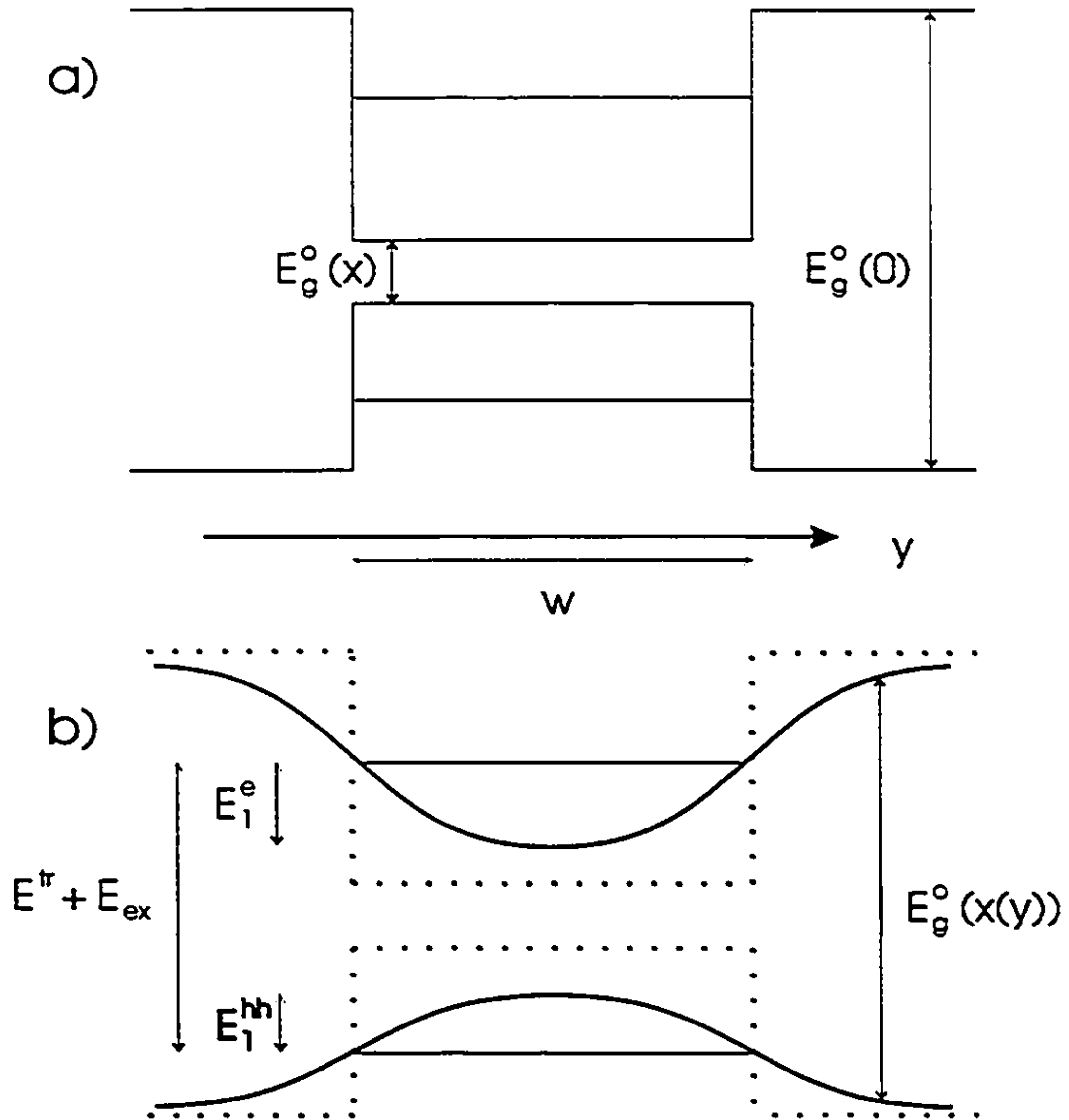

Fig. 3.7 Diagram depicting the band structure of an InGaAs quantum well of width w before (a) and after (b) compositional disordering. The Indium concentration is symbolized by "x".

$$x_i(z) = x[1-\frac{1}{2}erf(\frac{\frac{1}{2}w-z}{2\Delta_i})-\frac{1}{2}erf(\frac{\frac{1}{2}w+z}{2\Delta_i})] \quad (3.6)$$

where x is the initial indium fraction and Δ_i is the interdiffusion length. Δ_i is defined such that $4\Delta_i$ is the distance across the QW interface over which the In concentration drop from 90% to 10% of the original value. In calculating the eigenenergies of the electron and hole states we assumed that the band gap and effective masses are determined (using equations (3.1)-(3.6)) by the local value of $x_i(z)$. This leads to a band profile like that shown in Fig. 3.7(b). In practice, of course, even starting from layers with thickness variations less than a monolayer, the ion beam damage is likely to lead to some variation of the resulting band profile across the implanted area so that the PL linewidth broadening is greater than would be if induced by a precise band profile like that illustrated in Fig. 3.7(b).

The transition energy between the first heavy-hole and electron states E_1^{hh} and E_1^e (measured with respect to their respective band minima) is

$$E^{tr} = E_1^{hh}+E_1^{e}+E_g^{hh}(z=0)-E_{ex} \quad (3.7)$$

where the exciton binding energy E_{ex} was calculated for a confined hydrogenic exciton[3.42].

In Fig. 3.8(a) and (b) we show the calculated transition energy (blue) shifts ΔE^{tr} as a function of interdiffusion length Δ_i for initial indium fractions 5% and 20%. Obviously the larger the concentration, the greater the possible shift due to

interdiffusion. Also shown in these figures are the heavy-hole and electron eigenenergy shifts which are clearly dominated by the change in the band gap to produce a net positive ΔE^{tr}. In these calculations, the exciton binding energy E_{ex} was assumed to be constant, independent of interdiffusion. However, as the In composition decreases, E_{ex} is known to decrease. We estimate that this will contribute a maximum of 1.5 meV to the shifts discussed below.

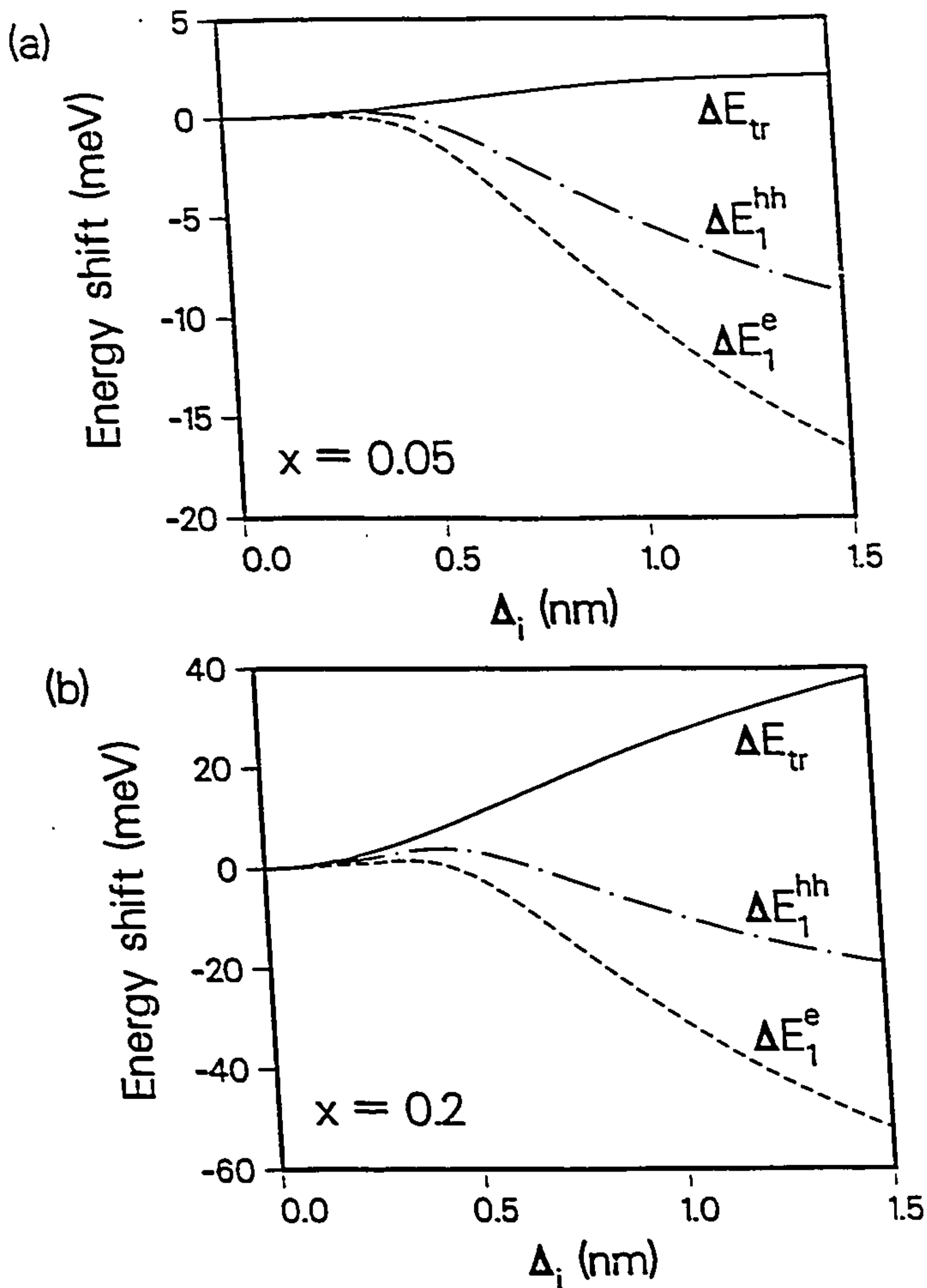

Fig. 3.8 Calculated transition energy shifts ΔE^{tr} plotted as a function of the interdiffusion length Δ_i for (a) 5% and (b) 20% indium concentration. Also shown are the heavy-hole and electron eigenenergy shifts which are dominated by the change in the band gap to produce the net positive ΔE^{tr}.

3.4.2 Results

Although we were primarily interested in the gap energy shifts required to produce the net positive ΔE^{tr}, induced by implantation, we tested the validity of the model described above by comparing the calculated absolute transition energies, E^{tr}, with measurements on the four quantum wells in unimplanted areas (i.e., as grown) of sample 1020 and 1021. The PL energies for these transitions are given in Tables III.II (#1020) and III.III (#1021). The PL uncertainties quoted are an indication of the lateral variation across the wafer i.e. statistical errors (these uncertainties do not include the systematic errors that may arise from the use of equations (3.1) to (3.7)). A more realistic estimate, including these statistical errors would yield an uncertainty of ± 0.5%. Using equation (3.7), we calculated the indium concentration required to give the observed transitions energies for wells of width 3 nm and these are also shown in Tables III.II and III.III. Excellent agreement was found with the RBS-determined In concentration. It should be noted that an error in the reported thickness of the quantum wells would cause both the RBS and PL determinations of the In concentration to change in the same direction and therefore the comparison is relatively insensitive to this width.

The broad area implanted regions were examined before annealing. The intensities of the luminescence from the quantum wells were greatly reduced but were not shifted in energy compared

to the surrounding unimplanted region. This indicates that the implant doses were well below those required for collisional (ion beam) mixing, consistent with what has been reported previously for the AlGaAs system[3.32].

The observed energy shifts for each of the four quantum wells after broad area implantation and annealing are shown in Tables III.IV and III.V. "Missing" entries in the tables indicate conditions where no luminescence was observed (i.e., complete disordering and/or incomplete removal of non-radiative recombination sites). A typical PL spectrum before and after broad area implantation followed by RTA is shown in Fig. 3.9 for sample #1020.

Remembering that the mean range R_p and straggling ΔR_p of 100 keV Ga^+ ions in randomly aligned GaAs are 50 and 25 nm respectively, the effect of channeling which results in implantation ions penetrating further into the sample[3.43] is immediately apparent in Tables III.IV and III.V. Substantial compositional disordering has been initiated even for the QW which is 450 nm below the surface, a distance nearly ten times the mean range. This is similar to the observations of Laruelle and co-workers in the AlGaAs system[3.29]. As the dose is increased, the energy shifts saturates (or slows significantly for QW3) as shown in Fig. 3.10. As explained before, even for a "perfectly" aligned beam, there is a substantial amount of dechanneling of the ions in the near-surface region. As the implantation proceeds, the damage created by the dechanneled ions increases the dechanneling rate

until no further ions are channelled deep into the bulk. This self-limiting process leads to a saturation of the damage created at greater depths and therefore to a saturation in the shift of the luminescence[3,43].

TABLE III.IV Energy shift (meV) of PL after broad-area implantation of sample 1020 and annealing for 60 seconds at 850°C along with the calculated interdiffusion length Δ_i required to give the fitted shift.

Dose (10^{13} Ga^+/cm^2)	QW1		QW2		QW3		QW4	
	shift (meV)	Δ_i (nm)	shift (meV)	Δ_i (nm)	shift (meV)	Δ_i (nm)	shift (meV)	Δ_i (nm)
0.6	3.2	0.82	7.8	0.92	10.6	0.73	6.8	0.44
2.0	4.5	1.13	11.1	1.31	16.6	1.05	16.1	0.77
4.0	...	...	12.2	1.50	16.6	1.05	16.3	0.78
7.0	...	...	...	...	17.6	1.11	16.4	0.78
11.0	...	...	...	...	19.2	1.21	16.5	0.78

TABLE III.V Energy shift (meV) of PL after broad-area implantation of sample 1021 and annealing for 60 seconds at 850°C along with the calculated interdiffusion length Δ_i required to give the fitted shift.

Dose (10^{13} Ga^+/cm^2)	QW1		QW2		QW3		QW4	
	shift (meV)	Δ_i (nm)	shift (meV)	Δ_i (nm)	shift (meV)	Δ_i (nm)	shift (meV)	Δ_i (nm)
0.6	19.4	0.82	10.3	0.64	5.2	0.59	0.3	0.18
2.0	25.1	1.01	15.4	0.86	7.7	0.77	0.5	0.23
4.0	...	...	17.1	0.94	7.7	0.77	0.5	0.23
7.0	...	...	...	...	9.6	0.92	1.4	0.41
11.0	...	...	...	...	9.8	0.94	1.4	0.41

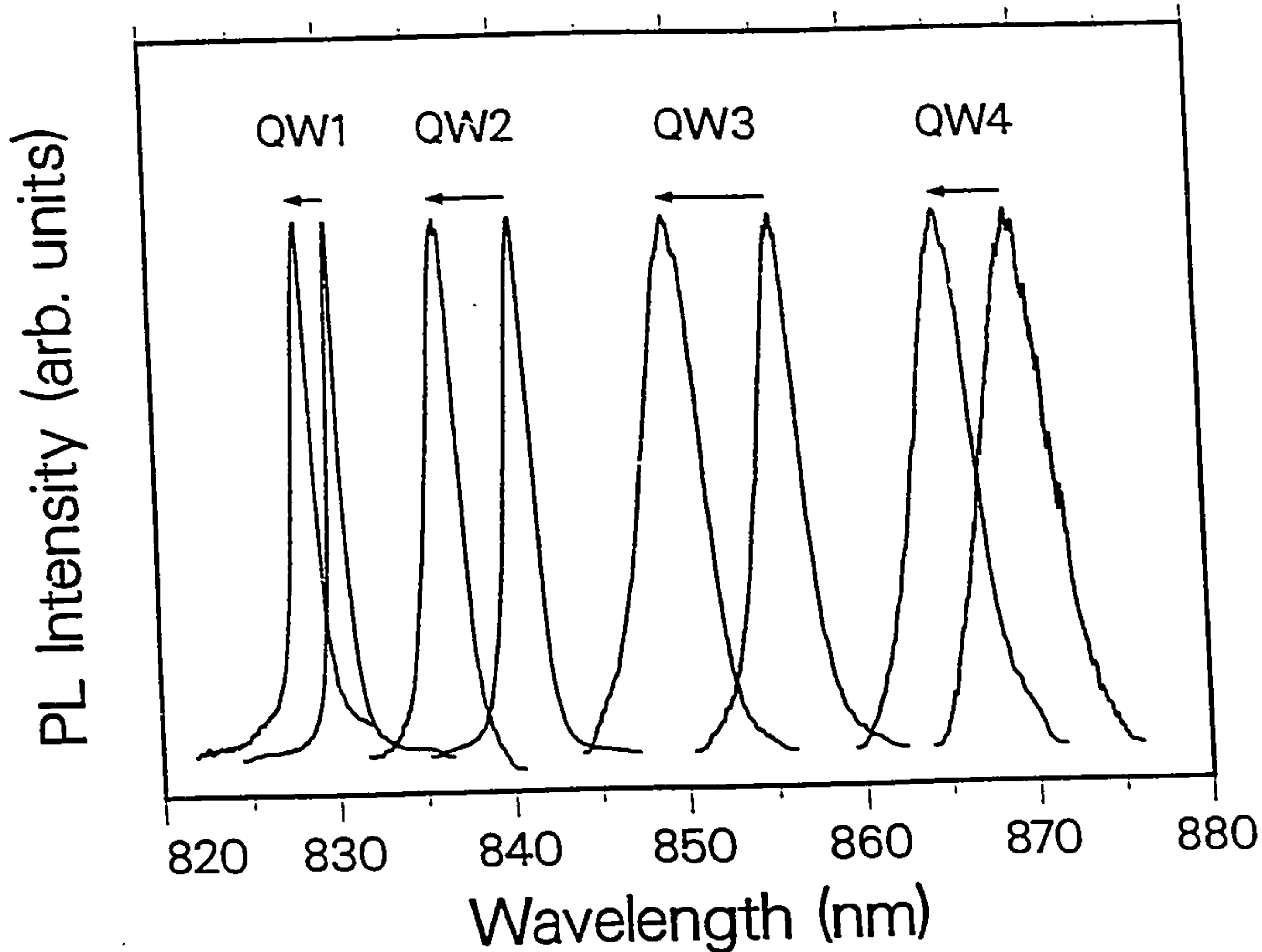

Fig. 3.9 Low temperature (4K), normalized, PL spectra of sample 1020 (see TABLE III.I) before and after broad-area implantation with 0.6×10^{13} Ga^{+} ions/cm^2 and RTA at 850°C for 60 seconds.

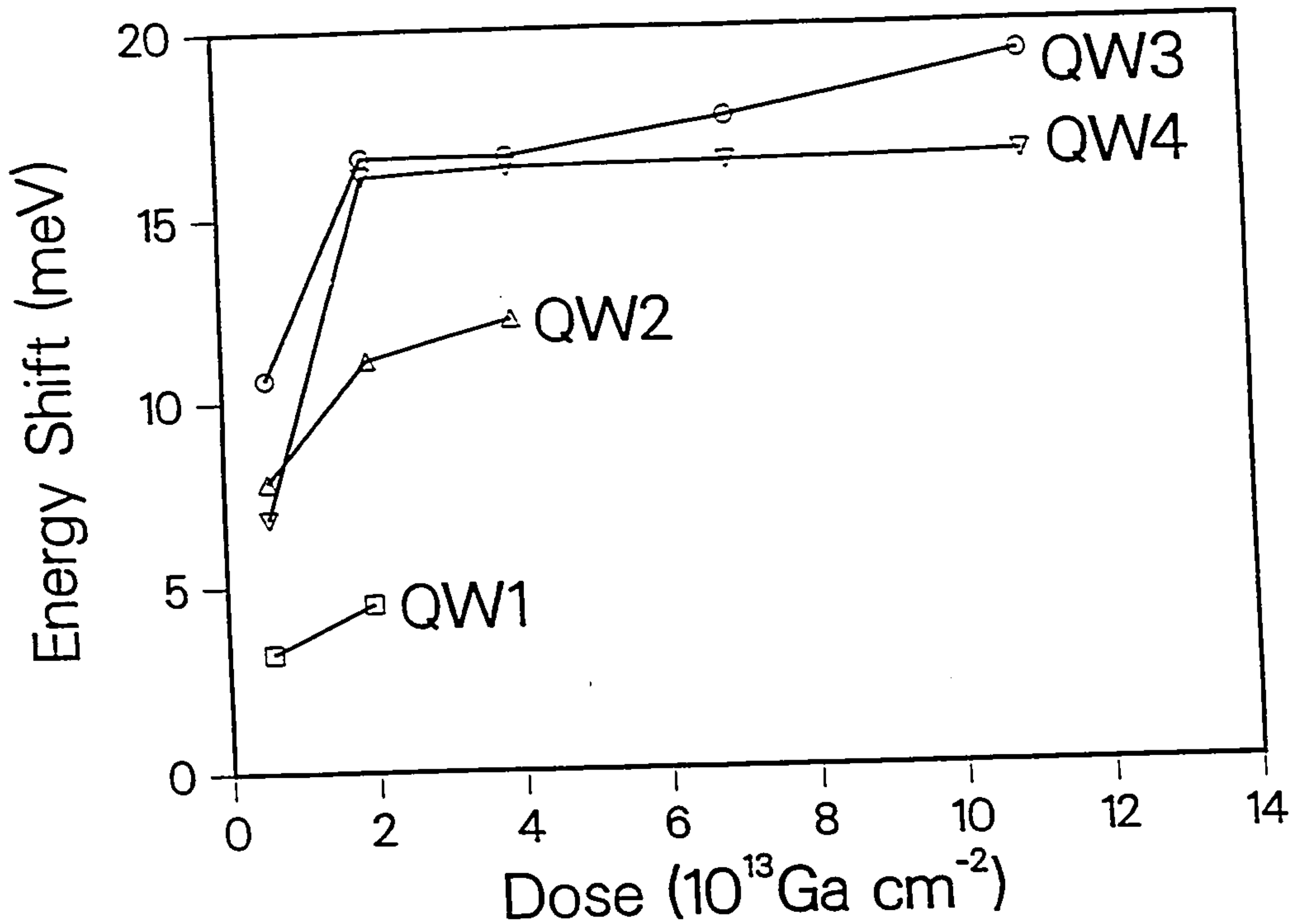

Fig. 3.10 Ga⁺ dose dependence of the PL transition energy shift for the four quantum wells of sample 1020.

Also included in Tables III.IV and III.V are the interdiffusion lengths Δ_i as calculated using the formalism previously outlined. The disordering as indicated by either PL shift or Δ_i in a given QW will be proportional to the dose of ions and, potentially, the indium concentration. As discussed above, the peak in the depth distribution occurs near the first QW with a tail extending at least as far as the fourth QW due to channeling. In sample #1020 the In concentration increases from QW1 through QW4 and it is the competition between the dose and In concentration in this sample that leads to the non-monotonic behaviour in the energy shift and Δ_i as a function of depth. Conversely, for sample #1021 the In concentration decreases from QW1 through QW4 and the observed PL shift and Δ_i show the expected monotonic decrease with depth. This is illustrated in Fig. 3.11. The present implantation geometry does not allow us to determine the quantitative relationships between dose, In concentration, and Δ_i for our strained system because of the uncertainty in the fraction of the dose delivered to each of the quantum wells under channeling conditions. We note, however, that the Δ_i all lie below 2 nm which is the same range observed for the unstrained AlGaAs/GaAs studies of Laruelle and co-workers[3.44], suggesting that strain is not substantially enhancing Δ_i. To determine the relationship between Δ_i and dose, or to answer the question as to whether the In concentration and/or strain in quantum well will lead to enhanced compositional disordering for a given dose requires either that the implantation be undertaken in a random direction or, at least, in

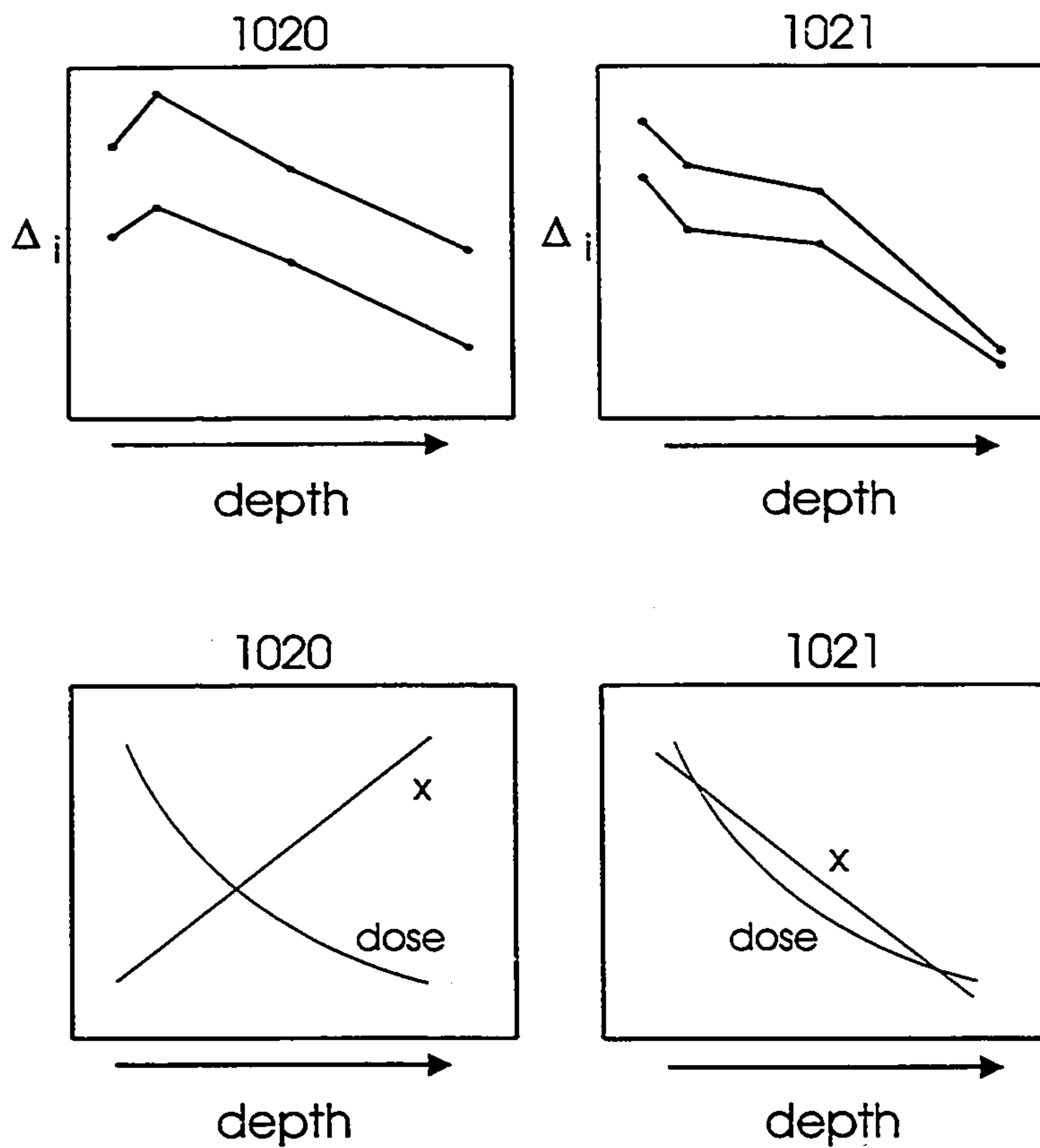

Fig. 3.11 The top two figures show the calculated interdiffusion lengths for the two lowest implanted doses in samples 1020 and 1021 (see Tables III.IV and III.V). The bottom figures show the manner in which the indium concentration (x) and the delivered dose vary as with sample depth.

a well-defined channeling direction.

The PL data obtained for the wire geometry (QW4) in sample #1020 are given in Table III.VI as a function of implantation dose and rectangle width.

TABLE III.VI Energy shift of photoluminescence (meV) observed from the compositionally disordered regions of QW4 of sample 1020 after implantation in the wire geometry and annealing at 850°C for 60 seconds.

Dose (10^{13} Ga^+/cm^2)	Implantation rectangle width (μm)				
	0.4	1.2	1.6	1.8	250
0.6	3.1	4.6	6.3	6.4	6.8
2.0	4.6	12.2	15.4	15.9	16.3
4.0	5.4	13.1	15.6	16.3	16.3
7.0	6.3	14.4	16.4	16.6	16.4

We observed a single PL peak which exhibited a monotonic shift in energy away from the broad-area implant value as the width of the implanted strip was reduced. If one assumed that the lateral straggling was small and the generated carriers did not diffuse before recombination, two PL peaks would be expected originating from unimplanted and implanted regions of the illuminated area. However a lower-bound estimate for the lateral diffusion of carriers in the QW region (in the absence of band gap modulation) would be ~1.9 μm[3,45] comparable to the 2 μm period of the lateral modulation. Since the carriers should diffuse to the lower-band-gap regions this is consistent with our observation of a single PL peak. What is surprising is that the observed peaks are at an

energy significantly higher (3-16 meV) than expected for an as-grown QW in an unimplanted region. This would seem to imply that the entire area has been compositionally disordered to some extent and hence that the apparent lateral straggling (~1 μm) must be much larger than expected. It should be noted that a partial release of the strain in the QW region would lead to a significant decrease in the PL peak energy and is thus not consistent with our experiment.

Table III.VII shows the equivalent data (QW4, #1020) for implantation into the box geometry. Even though the wire and box regions received nominally the same dose, for such large lateral straggling as observed above the energy shifts in the box regions should be, and were, larger than for the wire geometry (Table III.VI).

TABLE III.VII Energy shift of photoluminescence (meV) observed from the compositionally disordered regions of QW4 of sample 1020 after implantation in the box geometry and annealing at 850°C for 60 seconds.

Dose (10^{13} Ga^{+}/cm^{2})	Implantation rectangle width (μm)				
	0.4	1.2	1.6	1.8	250
0.6	7.1	6.8	7.1	6.1	6.8
2.0	8.2	15.6	16.1	16.1	16.3
4.0	10.2	15.9	16.4	16.6	16.3
7.0	11.4	15.7	16.6	14.9	16.4

Using the model of Cibert and Petroff[3.41] we calculated the lateral straggling required to shift the "unimplanted" region peak to the observed value and found values typically between 0.6 and 3

μm, consistent with the above qualitative observation. Similar results were obtained with QW3 and QW4 of sample #1021. These estimates appear to be inconsistent with the measured ion-beam width (70 nm). Note that there is an inherent assumption in the interpretation of the data that changes to the local energy bands (as observed through energy shifts) are induced only by compositional disordering and that there exists a one-to-one correspondence between the disordering and the lateral ion distribution. The agreement between theory and experiment for the broad area implant data supports the association of energy-band shifts with compositional disordering but does not establish any definite correspondence with the ion distribution.

The largest possible lateral straggling would be expected for implantation into a random direction. To reach a depth comparable to that of QW4 (450 nm) Ga ions would have to be implanted at ~1 MeV (ten times the energy used in this study) and would have a lateral ion straggling of ~340 nm which is still much smaller than that required to explain our observed results. We may formulated two parallel hypotheses from this result. The first possibility is that we have induced disordering of the QW in regions where the ion beam did not probe (i.e., there is not a one-to-one correspondence between the disordering and the lateral ion distribution) and further that the additional disorder is most likely related to the strain in the QW since it was not observed in the AlGaAs/GaAs system[3.29]. This conclusion is further supported by an examination of the wire (box) structures prior to annealing. Peaks with

energies corresponding to as-grown (unimplanted) material were observed from all four quantum wells. The intensities of these peaks decreased with increasing distance from the surface consistent with an increasing lateral spread of the ion beam with depth and with an increase of opacity of the material above the QW in question as the probed well is deeper. These results demonstrate that the true lateral straggling of the ion beam was not as large as estimated from the post-annealed data (although interpretation of the intensities is difficult because of the uncertainty in the beam alignment). One possible cause of laterally extended disordering might be strain-enhanced migration during post-implantation annealing. The other explanation is that although the FIB is quite narrow, its background dose might be sufficiently high to induce intermixing in "unimplanted" regions of InGaAs/GaAs QWs; a typical FIB profile is shown on Fig. 3.12. This is discussed in the following section.

3.5 The Critical Dose

Consider a sample subjected to implantation at a certain dose. One can view the total damage inflicted by the implantation as the sum over all ions of the damage created by single ions. We may then regard a single ion as the precursor of a "damage-cylinder" having radius r_d. The direct observation of r_d by transmission electron microscopy (TEM) of *in situ* implantation have yielded

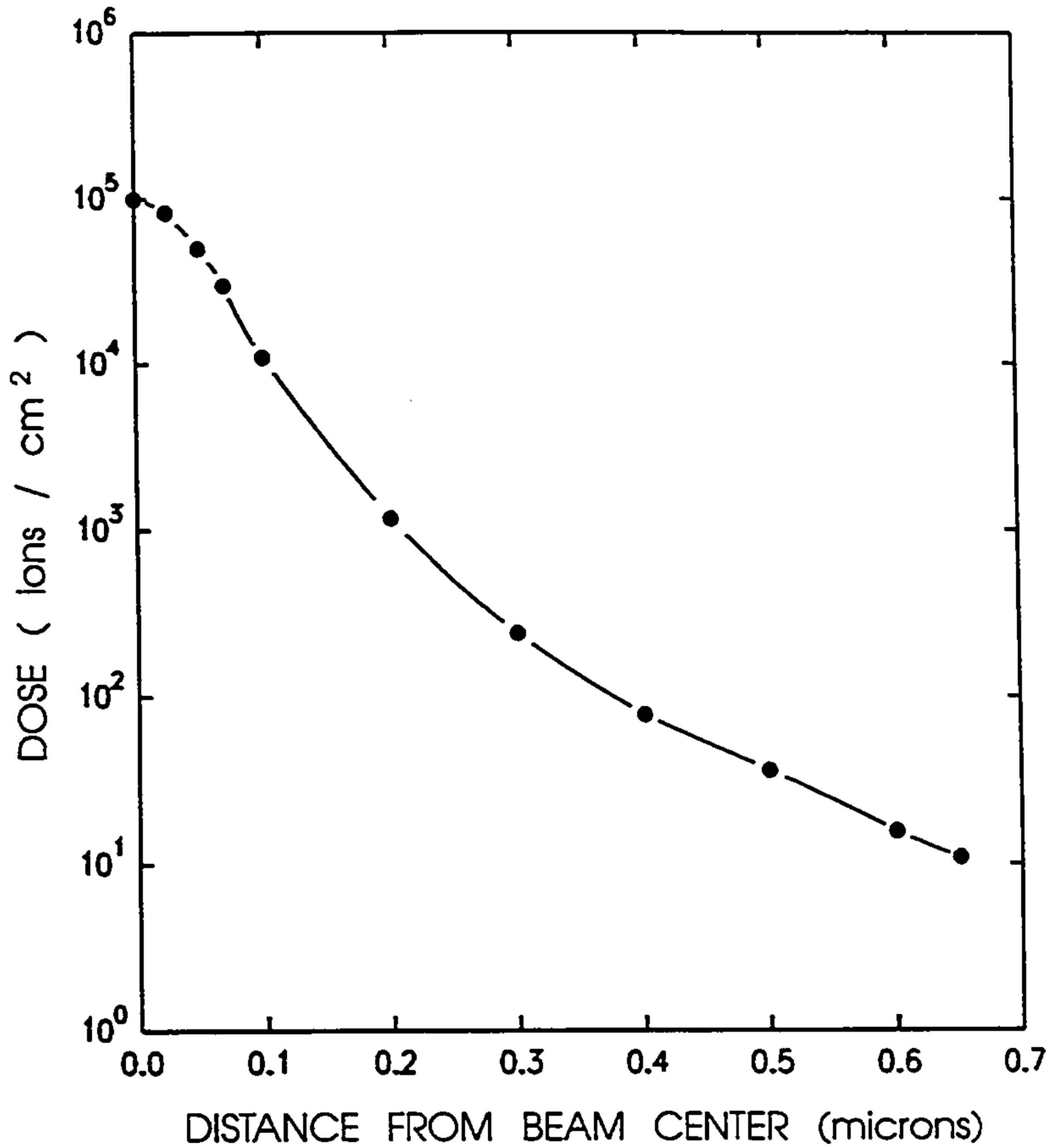

Fig. 3.12 Profile of focused ion beam for Au ions. Doses four orders of magnitude smaller than that delivered at the center of the beam are being implanted at distances of 0.65 microns away from the beam center (background dose).

values of 4.0 nm for 50 keV Kr ions implanted in GaAs at 30 K[3.46] and ~0.7 nm for 320 keV Ga ions implanted at 77 K.[3.47] Upon annealing, this damage radius gives rise, in QW structures, to a mixing radius r_m defined as the extent of the lateral compositional intermixing which was found to be of the order of 20 nm for the AlGaAs/GaAs QW system implanted with 8 MeV Bi ions[3.48].

Consider an exciton located in an implanted and annealed QW structure. If the concentration of the compositional intermixing areas is low, i.e. if "intermixed cylinders" are not overlapping and if the distance between damaged areas is larger than the diameter of a QW exciton, the excitons created in the implanted areas will diffuse to the lower bandgap material (virgin material) and recombine thereby yielding an unshifted spectrum with respect to that of the virgin material. If the implantation dose is increased, the density of damage-cylinders will also increase hence reducing the mean spacing between damage areas. PL spectra will thus have an onset of blue-shifted peaks at the implantation dose which yields a mean spacing of the order of the exciton radius. At this dose, PL stemming from both damaged and undamaged areas will arise; that is how the term 'critical dose' is defined[3.47]. If the dose is further increased, the whole area will have been damaged and the PL signal will comprise only blue shifted photons. The PL lines will also show the characteristic broadening due to statistical distributions of damaged areas of the sample (some of which have been damaged by more than one ion). Kalish and co-workers[3.47] determined r_m to be of the order of 20 nm for the

AlGaAs/GaAs QW system damaged by normally implanted 8 MeV Bi ions. They also showed the critical dose to be 7.5 x 10^{10} /cm^2.

We have undertaken similar PL studies in both AlGaAs/GaAs and InGaAs/GaAs QW structures. Two AlGaAs/GaAs samples were studied. One of these structures comprised four wells (sample 1198) and the other, three (sample 1234). In both of these the concentration of aluminium was 30%. The details are as follows. Sample 1198: wells located at 50, 104, 260 and 470 nm below the surface with well widths of 35, 56, 95 and 185 Å respectively. Sample 1234: wells located at 118, 278 and 484 nm below the surface with well widths of 80, 45 and 28 Å respectively. For the InGaAs/GaAs samples, one was sample 1020, described in Table III.II, while the other was sample 1479 with the same nominal widths (3 nm) and location in depth as sample 1020. The indium concentrations were however somewhat different. Effectively, sample 1479 had 4.1, 7.4, 11.1 and 15.9% indium in QW1, QW2, QW3 and QW4 respectively. These concentrations were evaluated from fitting the virgin material PL peak position while considering the well width fixed at 3 nm (value obtained from TEM measurements).

These samples were implanted with 8 MeV Bi^+ ions which have a projected range of 1.19 µm and a range straggling of 0.26 µm and thus allow each well of every sample to receive the same dose. An RTA of 30 seconds at 850°C was subsequently done on each implanted sample. Each dose was uniformly implanted as a circle of 1 mm diameter thus permitting easy alignment of our HeNe laser (beam spot size ~20 µm) and thereby reducing the risk of inadvertently

exciting virgin material. All of the CW PL measurements were carried out while the samples were kept at 5 K.

Let us first look at the results obtained from the AlGaAs/GaAs samples, for which four doses were studied. These, along with the PL peak energy shift and the interdiffusion length of each QW with respect to neighbouring virgin material, are given in TABLE III.VIII for sample 1198 and TABLE III.IX for sample 1234.

TABLE III.VIII PL peak energy shifts (meV) and Δ_L (nm) for AlGaAs/GaAs sample 1198.

Well (width)	Dose (Bi^+/cm^2)			
	6×10^{10}	3×10^{11}	2×10^{12}	1×10^{13}
QW1 (35 Å)	1.5 meV 0.11 nm	6.2 meV 0.26 nm	38.3 meV 0.73 nm	81.6 meV 1.27 nm
QW2 (56 Å)	1.3 meV 0.19 nm	6.7 meV 0.41 nm	43.6 meV 1.10 nm	81.2 meV 1.64 nm
QW3 (95 Å)	0.2 meV 0.17 nm	2.5 meV 0.41 nm	19.5 meV 1.20 nm	34.1 meV 1.58 nm
QW4 (185 Å)	0 meV 0 nm	0.8 meV 0.50 nm	4.7 meV 1.34 nm	6.5 meV 1.58 nm

TABLE III.IX PL peak energy shift (meV) and Δ_L (nm) for AlGaAs/GaAs sample 1234.

Well (width)	Dose (Bi^+/cm^2)			
	2×10^{10}	1×10^{11}	7×10^{11}	6×10^{12}
QW1 (80 Å)	0.4 meV 0.16 nm	1.3 meV 0.27 nm	6.9 meV 0.60 nm	36.1 meV 1.37 nm
QW2 (45 Å)	0.9 meV 0.04 nm	2.9 meV 0.20 nm	29.0 meV 0.73 nm	110.4 meV 1.89 nm
QW3 (28 Å)	2.3 meV 0.13 nm	4.7 meV 0.20 nm	63.6 meV 0.95 nm	———

The energy shifts are graphed in Fig. 3.13 and Fig. 3.14 for samples 1198 and 1234 respectively. However, since the energy shift depends strongly on the well width, the degree of intermixing cannot be related directly to these shifts. That is why the fitted interdiffusion lengths are used to understand the degree of QW intermixing. Fig. 3.15 shows the interdiffusion lengths for samples 1198 and 1234. We can see that the Δ_t are in a fairly small range of values for a given dose and that the results from the two samples interleave quite well.

None of the PL spectra collected from either sample 1198 or sample 1234 showed a clear double peak structure attributable to partial mixing. However, QW3 of sample 1234 did show a broadened and shifted PL peak for a dose of 2 x 10^{10} ions/cm^2 as seen if Fig. 3.16. This clearly shows that intermixing is occurring even at this low dose but does not provide a clear cut case of partial compositional disordering. Nevertheless, we can ascertain that we are in the minimum dose limit for intermixing in AlGaAs/GaAs heterostructures since the PL peak energy shift for this narrow QW is only 2.3 meV. Such narrow wells (28 Å) constitute a sensitive probe to detect intermixing although their lineshape is wider than that of less sensitive wider wells and therefore makes it harder to observe a double peak structure if one is present. If we take this value of 2 x 10^{10} /cm^2 to be our critical dose (defined by the onset of PL peak energy shift) we can obtain the mixing radius, r_m, through

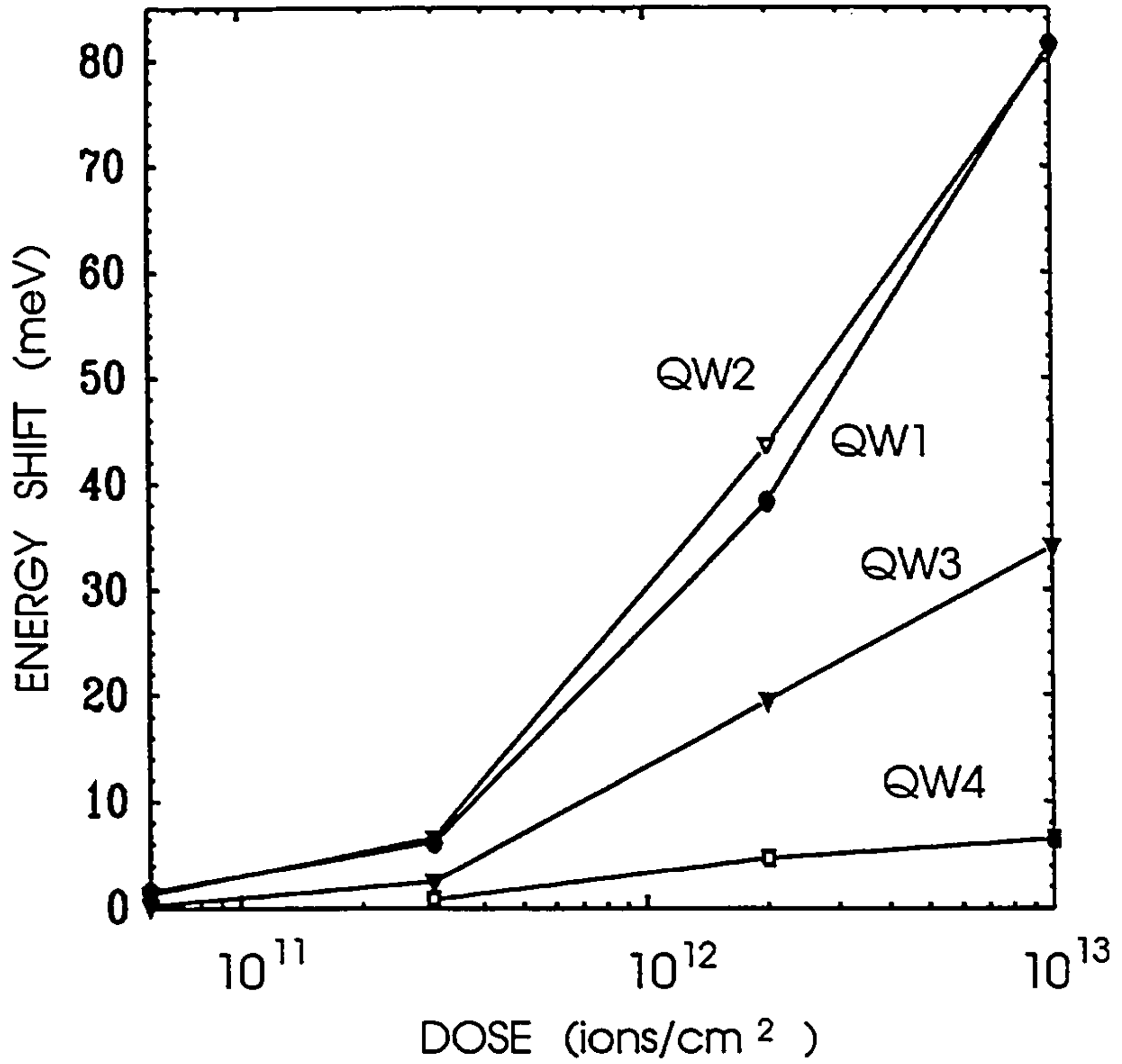

Fig. 3.13 PL peak energy shift Vs. uniform implantation dose of 8 MeV bismuth ions into AlGaAs/GaAs sample 1198.

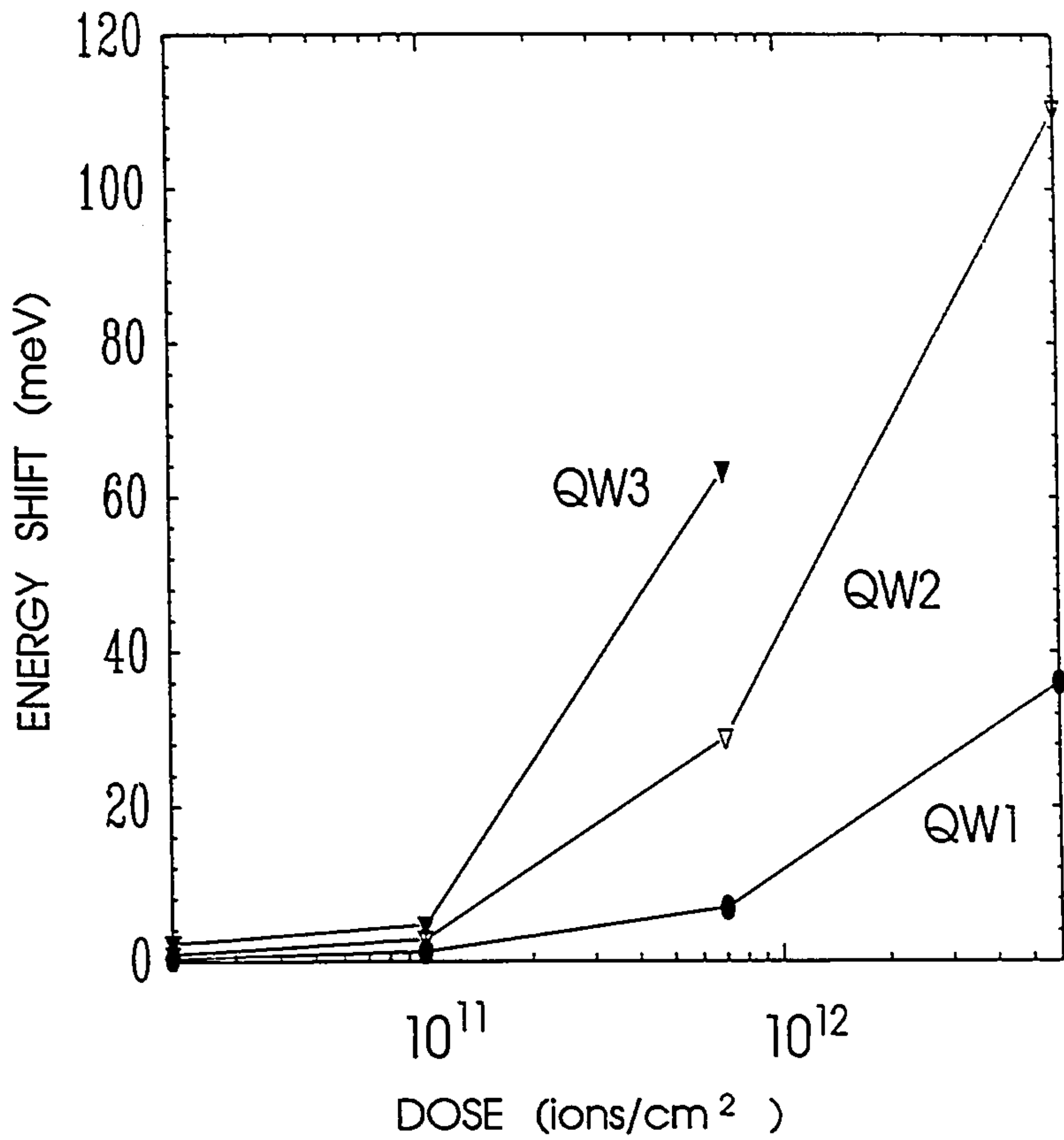

Fig. 3.14 PL peak energy shift Vs. uniform implantation dose of 8 MeV bismuth ions into AlGaAs/GaAs sample 1234.

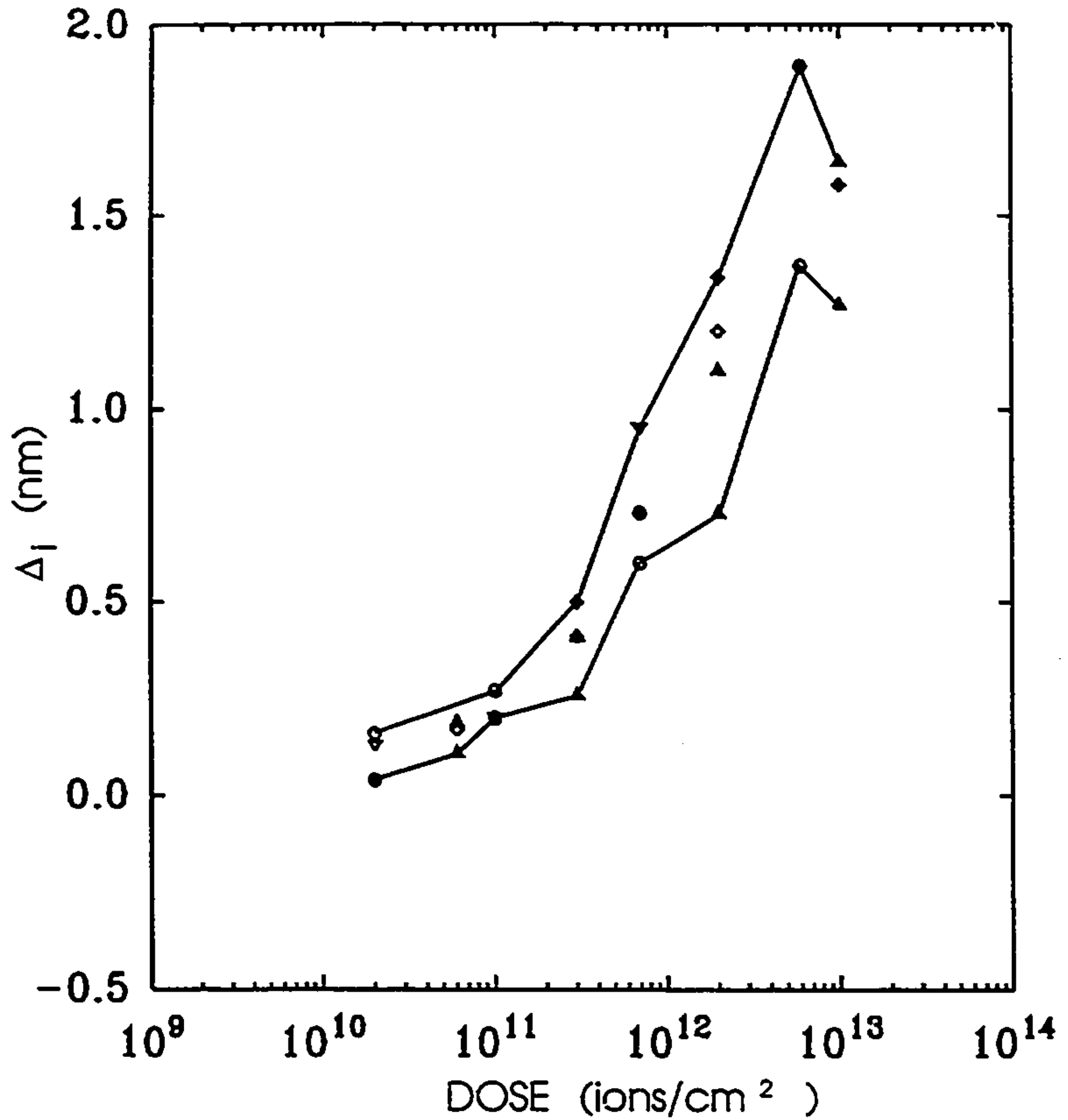

Fig. 3.15 Interdiffusion lengths fitted to PL energy shifts of figures 3.13 and 3.14. In order of distance from the sample surface the symbols for sample #1198 are for well widths: 3.5 nm (Δ), 5.6 nm (▲), 9.5 nm (◊) and 18.5 nm (♦). Symbols for sample #1234 are for well widths: 8.0 nm (○), 4.5 nm (●), 2.8 nm (▽). The lines follow the extreme values at each dose.

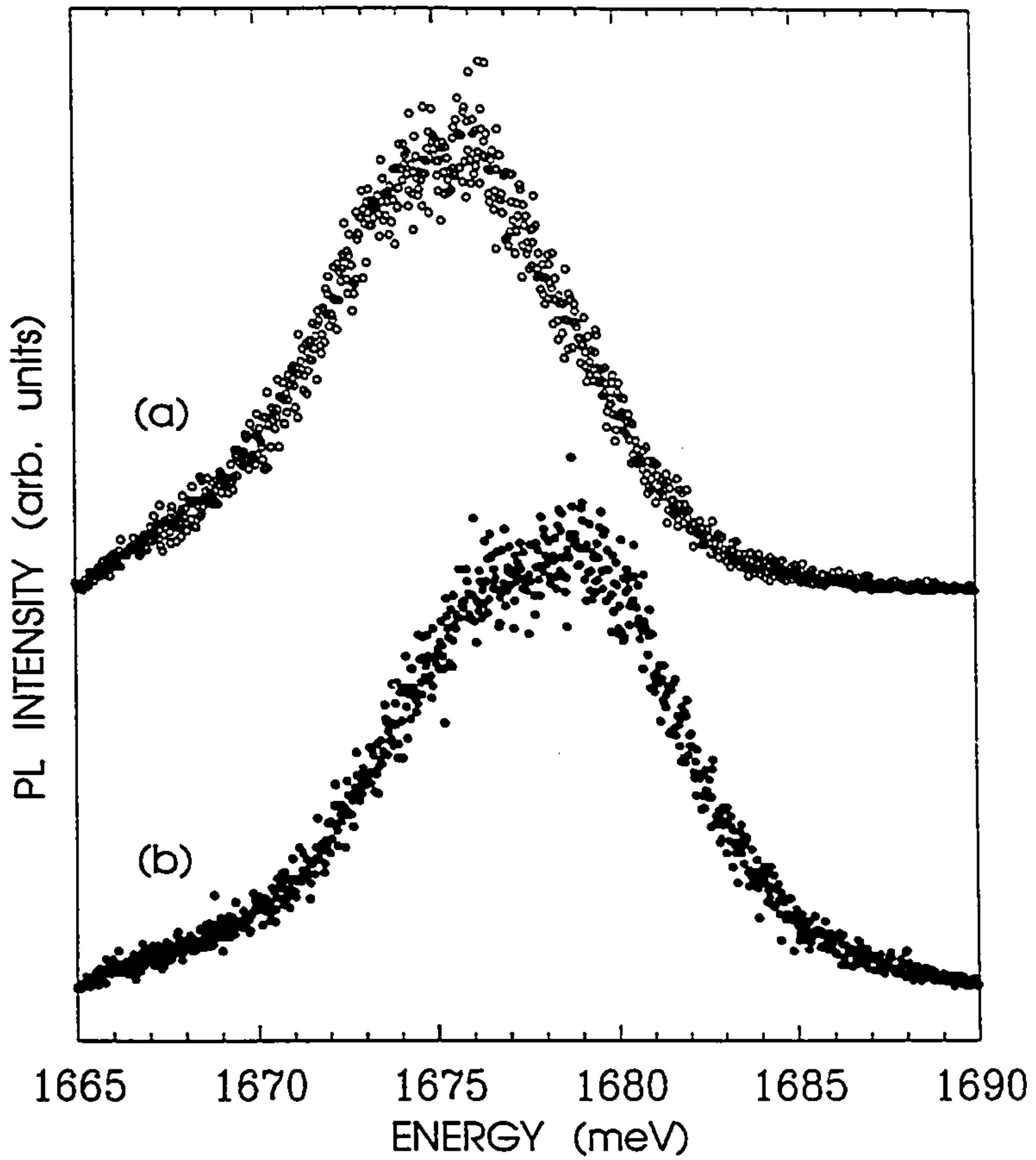

Fig. 3.16 PL spectra of virgin material (a) and uniformely implanted material (b) for QW3. The implanted dose was 2×10^{10} /cm^2.

$$N_c \pi r_m^2 = 1 \qquad (3.8)$$

where πr_m^2 is the area of the cross-section of an intermixed cylinder caused by the passage of a single ion and by the subsequent annealing. We find r_m = 40 nm, a value twice as large as that observed by Kalish and coworkers[3.47].

What is surprising is that we clearly observe blue-shifted peaks for all the wells even at the lowest implant dose and this, for both our AlGaAs/GaAs samples. They observed[3.47] the same for some of their wells but only down to a dose of 7.5 x 10^{10} /cm^2. A particulary interesting point is that they seemingly do not intermix their 20 nm wide (nominal) well even when subjected to doses in the 10^{12} /cm^2 regime combined with 4 minutes of 900°C RTA. This may be related to the fact that the well widths quoted in their paper are nominal values and that the actual widths are larger than the nominal ones.

Let us now look at the results obtained from our two InGaAs/GaAs QW samples. TABLE III.X relates the PL peak energy shifts and the interdiffusion lengths observed from sample 1020 whereas TABLE III.XI those from sample 1479.

TABLE III.X PL peak energy shifts (meV) and Δ_l (nm) for InGaAs/GaAs sample 1020. All wells are 3 nm in width.

Well (In (%))	Dose Bi^+ /cm^2			
	6×10^{10}	3×10^{11}	2×10^{12}	1×10^{13}
QW1 (7.0 %)	0 meV 0 nm	0.4 meV 0.25 nm	4.4 meV 1.05 nm	4.5 meV 1.08 nm
QW2 (10.3 %)	1.2 meV 0.28 nm	5.4 meV 0.69 nm	10.5 meV 1.18 nm	9.8 meV 1.11 nm
QW3 (14.7 %)	5.0 meV 0.45 nm	9.9 meV 0.70 nm	19.8 meV 1.23 nm	22.0 meV 1.37 nm
QW4 (18.0 %)	9.5 meV 0.54 nm	14.7 meV 0.72 nm	29.8 meV 1.32 nm	---

TABLE III.XI PL peak energy shifts (meV) and Δ_l (nm) for InGaAs/GaAs sample 1479. All wells are 3 nm in width.

Well (In (%))	Dose Bi^+ /cm^2			
	1×10^{9}	8×10^{9}	5×10^{10}	1×10^{11}
QW1 (4.1 %)	0 meV 0 nm	0 meV 0 nm	0 meV 0 nm	0 meV 0 nm
QW2 (7.4 %)	0 meV 0 nm	0.2 meV 0.17 nm	0.4 meV 0.24 nm	0.3 meV 0.21 nm
QW3 (11.1 %)	0.9 meV 0.24 nm	1.0 meV 0.25 nm	1.6 meV 0.32 nm	4.9 meV 0.61 nm
QW4 (15.9 %)	2.8 meV 0.30 nm	4.2 meV 0.38 nm	8.8 meV 0.59 nm	14.6 meV 0.84 nm

These correspond to Fig. 3.17 and Fig. 3.18 respectively. From Fig. 3.17 we can see that a considerable energy shift is observed even for the lowest of doses (6×10^{10} /cm^2). Having taken note of this, it was then decided to implant at even lower doses but at this point pieces of sample 1020 were no longer available

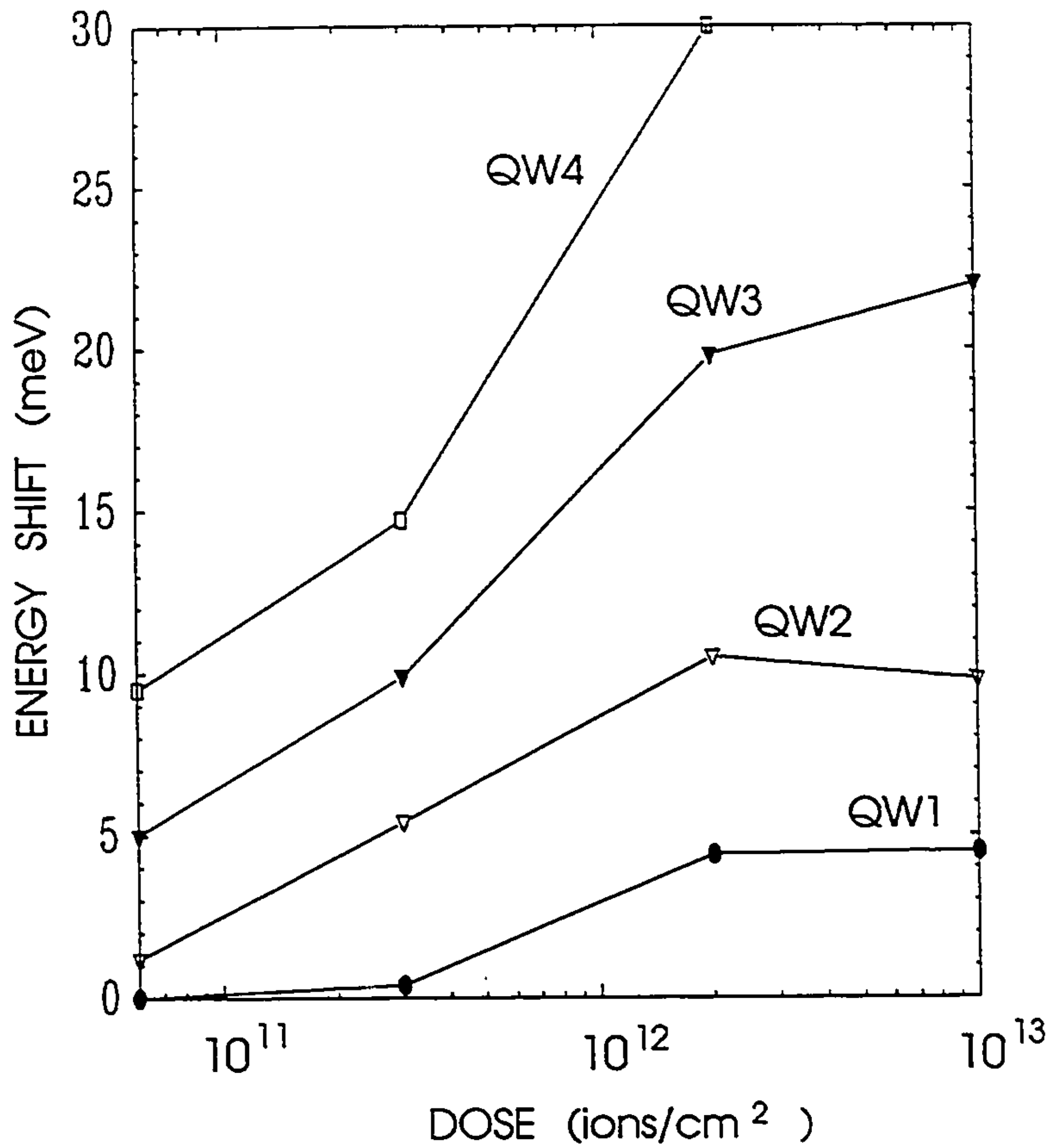

Fig. 3.17 PL peak energy shift Vs. uniform implantation dose of 8 MeV bismuth ions into InGaAs/GaAs sample 1020.

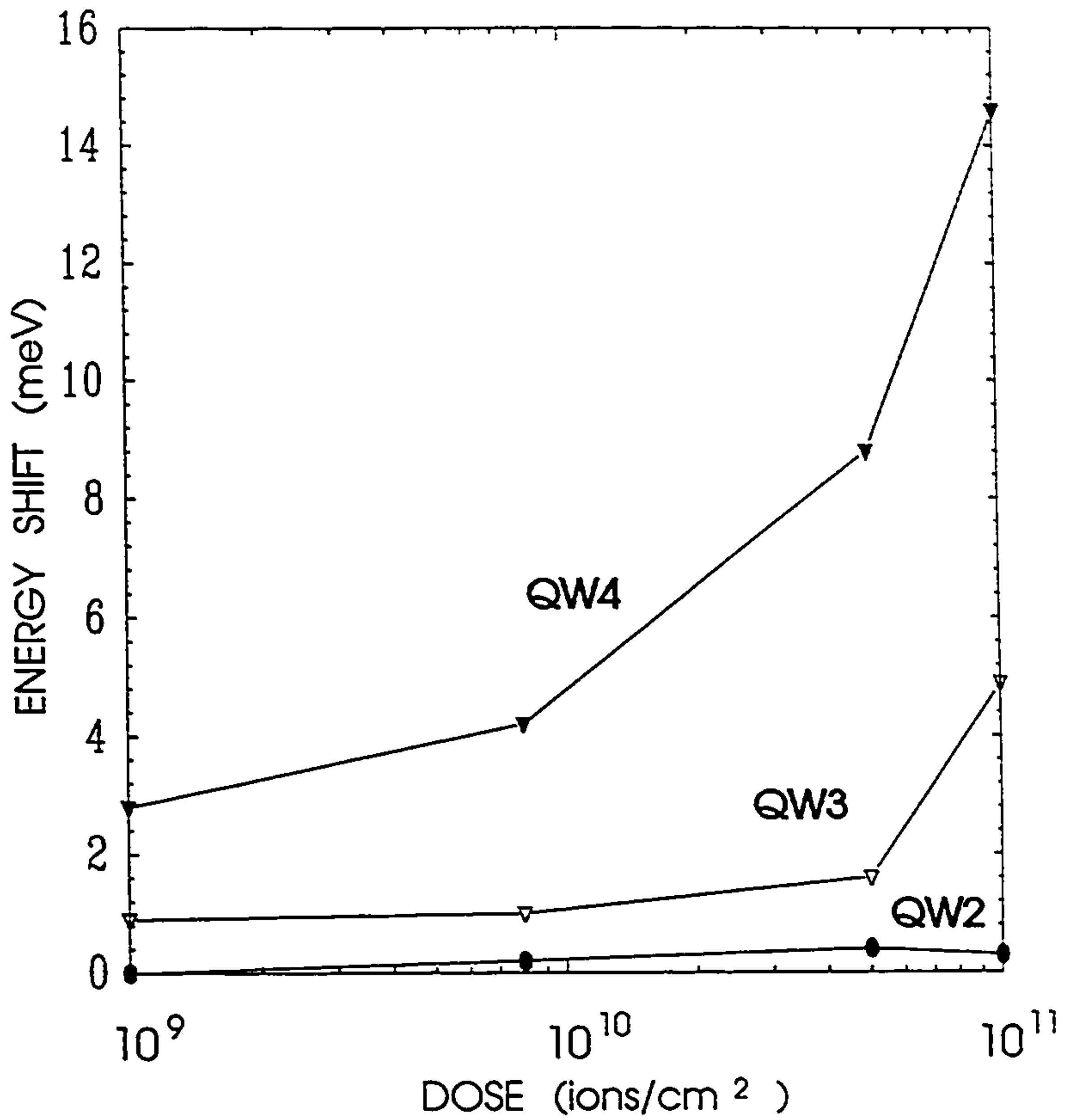

Fig. 3.18 PL peak energy shift Vs. uniform implantation dose of 8 MeV bismuth ions into InGaAs/GaAs sample 1479.

and a nominally similar sample was grown, sample 1479.

If we plot these two data sets on the same graph, as we did in Fig. 3.19, we see that the PL peak energy shift diminishes with implantation dose in both samples as it would be expected. However, there is some discrepancy in the overlapping dose region. Let us first look at QW4. For sample 1479, the In concentration was estimated to be ~16%, i.e. lower than that of QW4 of sample 1020 which is ~18%. We would then expect for a similar implantation dose that the PL peak energy shift of QW4(1479) would be smaller than that of QW4(1020). This is based on the assumption that the more indium in a well would mean more damage for a same delivered dose since indium atoms are bigger than gallium atoms and hence have a larger cross-section. This is not what we observe for the data point of QW4(1479) at the 1 x 10^{11} ions/cm^2 dose. The other three data points of QW4 of sample 1479 do however "line-up" fairly well with the respective curve of sample 1020. As for QW3 data of both samples, it is observed that the curve for 1479 does indeed lie below that of sample 1020 as it should due to lower indium content in the well. In fact, the QW3(1479) data should "line-up" more closely to QW2(1020) since their indium content are fairly close compared to that of QW3 in sample 1020. That is what is observed. As for QW1 and QW2 of both samples, the discrepancies are not as obvious.

Figure 3.20 shows the interdiffusion lengths fitted for samples #1020 and #1479. This figure shows a very clear and consistent behaviour of Δ_I as a function of indium concentration at

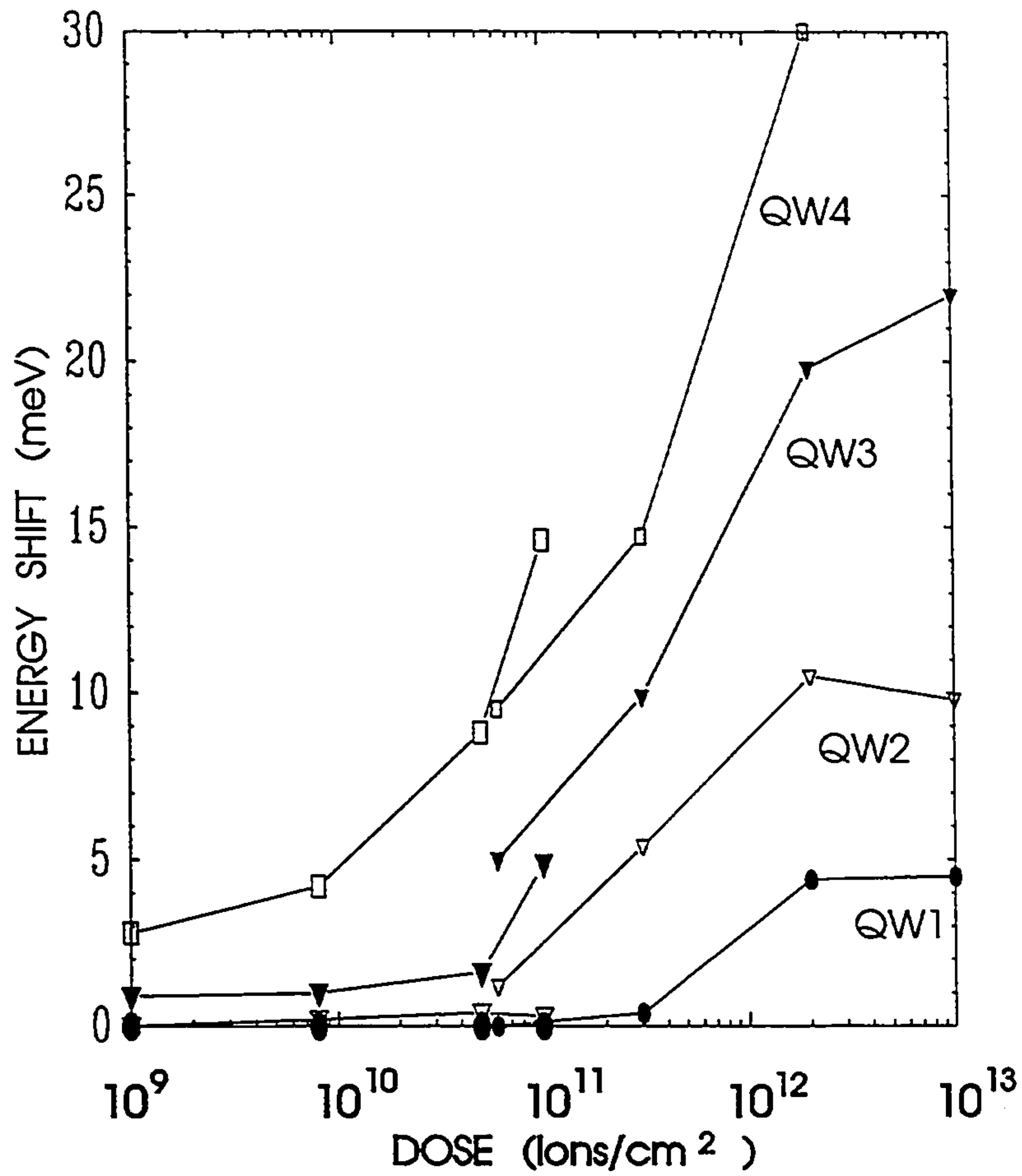

Fig. 3.19 PL peak energy shift Vs. uniform implantation dose of 8 MeV bismuth ions for InGaAs/GaAs samples 1020 (smaller symbols, higher doses) and 1479 (bigger symbols, lower doses).

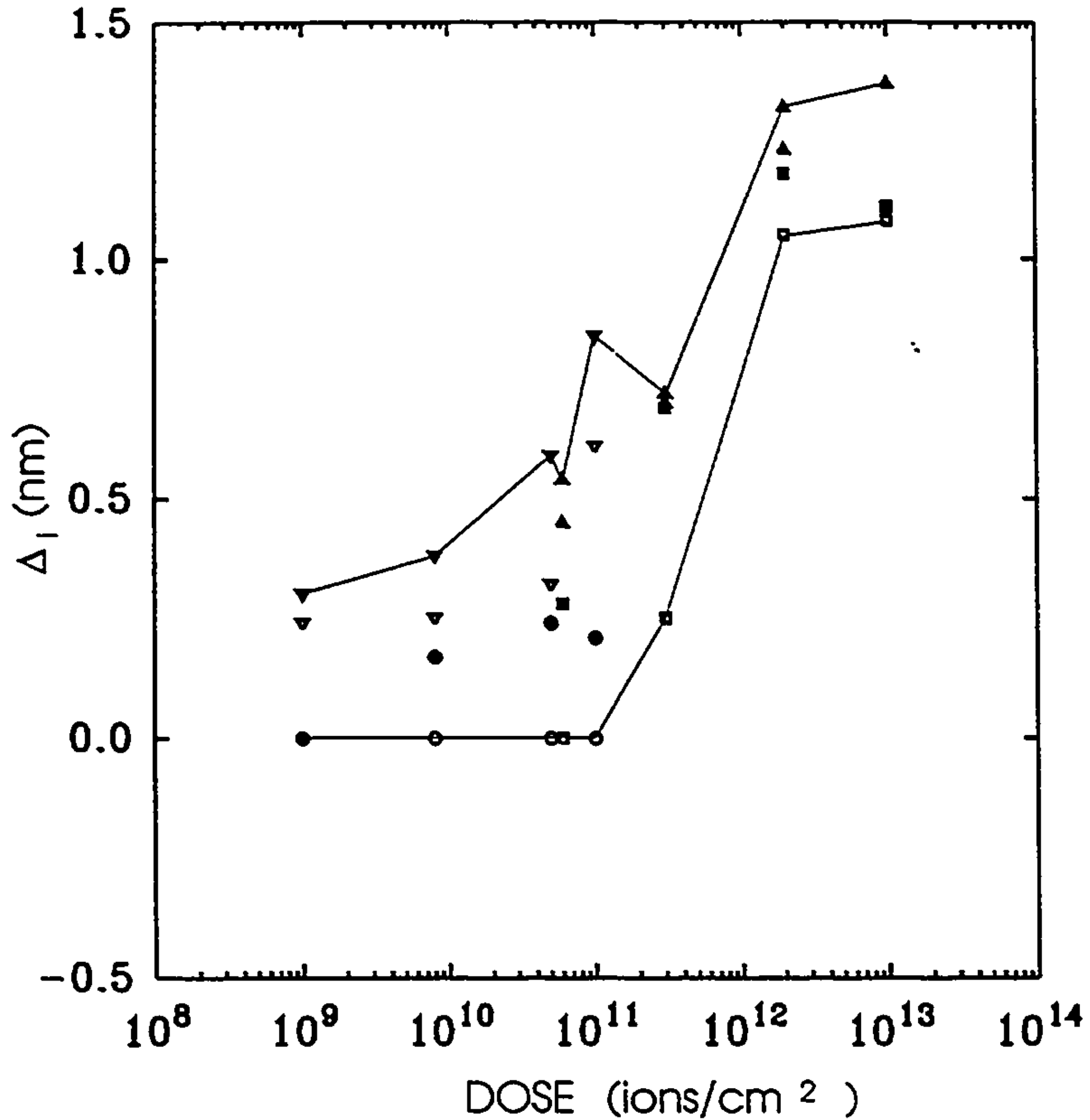

Fig. 3.20 Interdiffusion length fitted to the PL energy shifts of figures 3.17 and 3.18. In order of distance from the sample surface the symbols for sample #1020 are for x = 0.07 (□), 0.103 (■), 0.147 (△) and 0.180 (▲). Symbols for sample #1479 are for x = 0.041 (○), 0.074 (●), 0.111 (▽) and 0.159 (▼). The lines follow the extreme values at each dose.

a given dose. The data points from the two samples again interleave quite well at the intermediate dose. These results support the argument that strain and indium cross-section effects, both of which should increase with concentration, are the primary factors in lowering the threshold dose for QW intermixing in the InGaAs/GaAs system.

Let us now come back to the critical dose problem. Sample 1020 gave out a weak double peak structure for a dose of 6×10^{10} /cm^2 for QW1 as shown in Fig. 3.21. Sample 1479 showed no such spectra but nevertheless exhibited quantum well intermixing for the lowest implanted dose of 1×10^9 cm^{-2} in QW3 and QW4.

Let us try to put this into perspective by recalling what happens in the AlGaAs/GaAs case. Here, the delivered damage or, may we say the point defect creation probability , is the same for every well since the composition of these and of their barriers is constant throughout the structure. Therefore, there exists a one to one correspondence between implantation dose and delivered damage which does not vary from well to well.

Such is not the case for InGaAs/GaAs samples. Here, the relationship between implantation dose and delivered damage is dependent on the amount of In present in the well. Therefore, upon quoting the intermixing radius for InGaAs/GaAs quantum wells, one must state not only at which dose this was observed but also which concentration of indium was present in the initial material. Thus, in the case of QW1(1020) we find $r_m(7\%, 6 \times 10^{10}$ ions/cm$^2) = 23$nm.

Having not observed any PL double peak structure for the

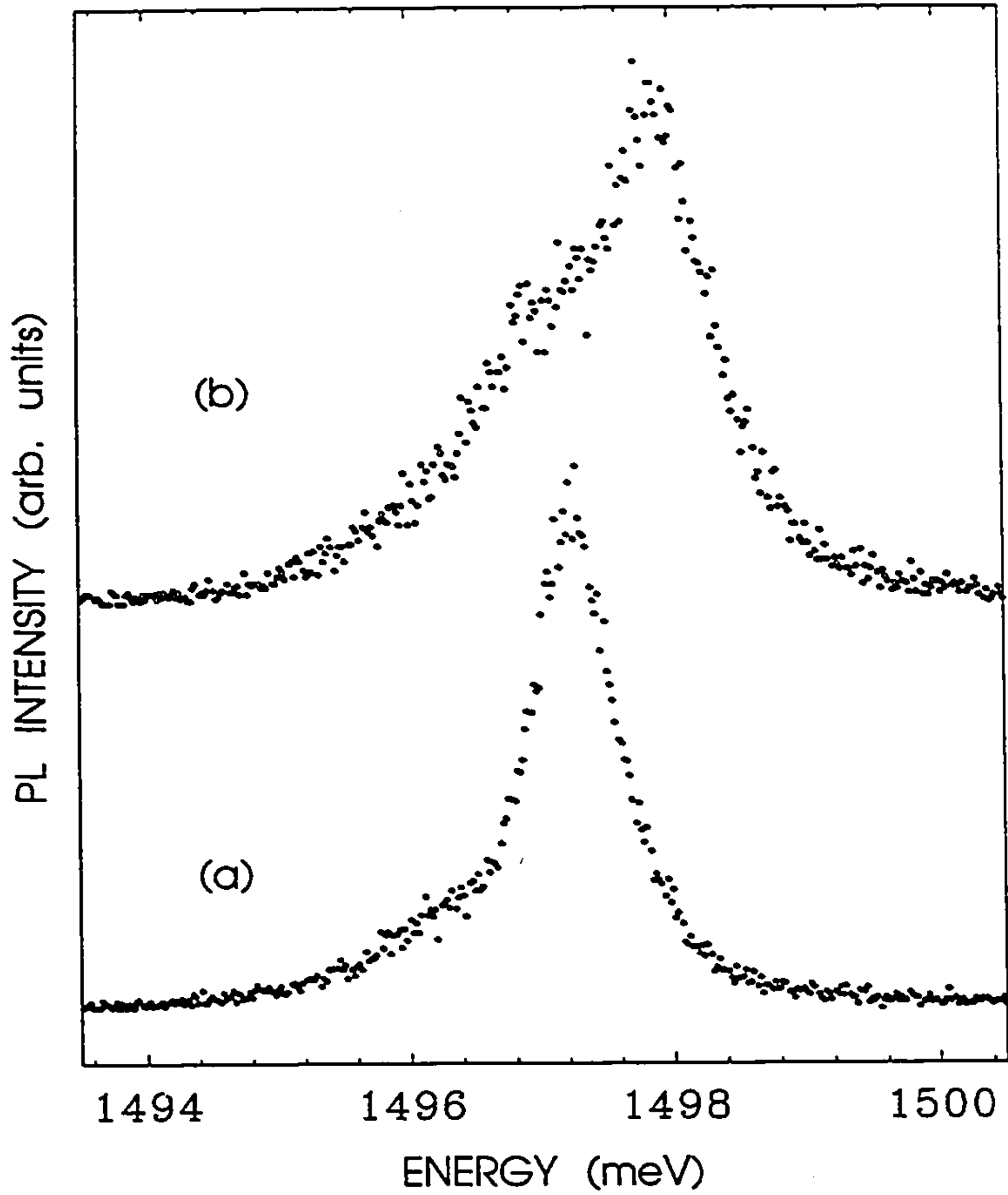

Fig. 3.21 PL spectra taken from sample 1020 showing (a) virgin material peak and (b) 6 x 10 ^{10}/cm^{2} uniformely implanted material associated with QW1. The blue-shifted spectra in (b) still shows a structure at the virgin material peak position.

lowest implants, i.e. sample 1479, we can arrive at the following explanation. The doses implanted are either too low to create the damage necessary to observe any double peak, let alone a peak shift (QW1 and partly QW2) or, the implanted dose/indium content relationship is such that the delivered damage exceeds what is needed to observe a double peak (QW3 and QW4).

Therefore, we may not extract mixing radii values exactly but only give a lower limit to what these values may be. Hence, for 11.1% (QW3) and 15.9% (QW4) indium composition wells of 3 nm in width we find $r_m > 178$ nm. This becomes interesting if one tries to relate it to the data of TABLES III.VI and III.VII obtained from the QWW and QWB geometries. We pointed out that we did not observe neither the PL typical of the virgin material nor that characteristic of the uniformly implanted material. The defects created in the rectangular strip region would have had to laterally migrate distances of the order of 1 µm in length. The critical dose data presented here does not put a precise number on the spatial extent of mixing due to the passage of a single ion but does indicate that further study of this subject is required to better understand what phenomenon are taking place.

However, if we consider the FIB profile of figure 3.12, we see that its background dose, 0.5 µm away from the center of the beam, would be sufficiently high to induce intermixing if the beam center dose is of the order of 10^{13} - 10^{14}. This means that "unimplanted" regions do in fact receive some ions. This could also explain, together with defect migration, the results of TABLES III.VI and

III.VII.

Further studies should include experiments capable of determining the actual damage delivered to a well as function of implantation dose and indium composition (perhaps Raman or TEM would be suited for this) and also photoluminescence studies of uniformly implanted materials at doses below the lowest ones we have looked at. Only then will one be able to quantitatively assess the potential of the implantation and annealing processes to create quantum well wires and quantum well boxes.

3.6 Si^+ Implantation: Low Dose Behaviour

We now briefly examine the effect of changing the implanted species from Ga^+ to Si^+. The general results are the same as for those for Ga^+ implantation but there is one significant difference for low dosage. In figure 3.22 we show the PL spectra for QW4 of sample #1021 at three different doses. It is clear from this figure that implantation with Si^+ initially leads to a red shift of the PL peak before the expected interdiffusion-induced blue shift is seen in figure 3.22(c). For the unimplanted region (Fig. 3.22 (a)) we see a low-energy shoulder that corresponds to a residual impurity-bound exciton transition[3.49]. This assignment is supported by the saturation of this feature with increasing PL excitation intensity. When the well is implanted with Si^+ ions, a large number of donors are introduced[3.50] resulting in a reduction

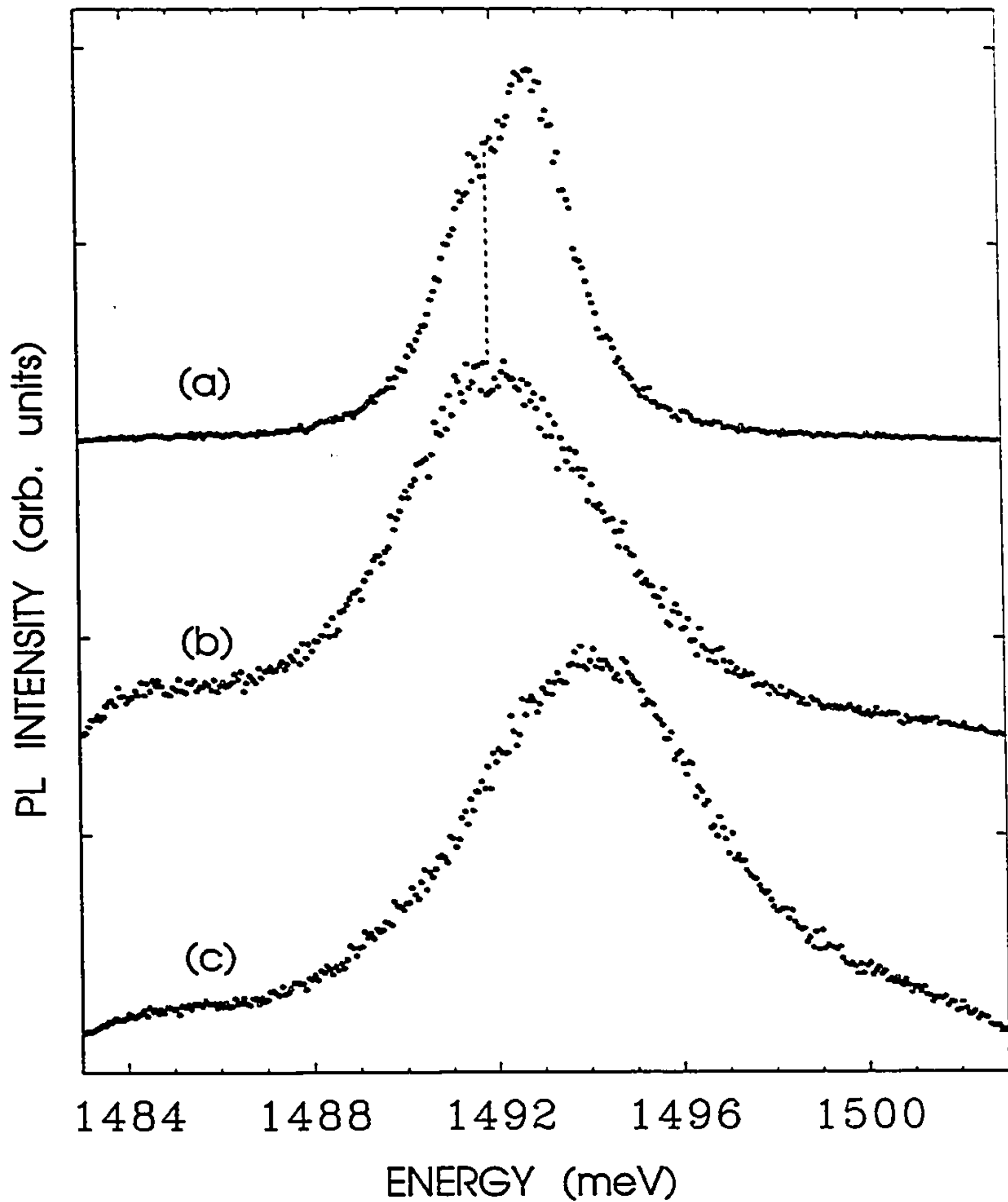

Fig. 3.22 Low-temperature (5K) PL spectra from QW4 of sample 1021. (a) virgin material, (b) 10^{13} Si^{+}/cm^{2} and (c) 4×10^{13} Si^{+}/cm^{2}. The vertical broken line indicates the transition associated with impurity bound excitons. The sample was RTA at 850 celsius for 60 seconds.

in the average PL transition energy (the red shift in Fig. 3.22(b)) which corresponds to the exciton localization energy. QW4 is the deepest well in the sample and therefore the dose delivered is correspondingly small so that the doping effect dominates the optical behaviour until interdiffusion effects become evident at higher doses (see Fig. 3.22(c)).

3.7 Exciton Lifetime and Implanted Dose

Using the PL setup described in Chapter 2, we measured the exciton lifetime for each of the quantum wells of sample #1020 for various implantation doses. We show in figure 3.23 the exciton lifetimes Vs. implanted dose. The decay times for QW2, 3, and 4 are characterized by an initial rise at low dose followed by a decrease at larger dose. It is important to note the difference between the dose dependence of the energy shift (Fig. 3.10) and the decay time (Fig. 3.23) for QW3 and QW4. At higher doses, the energy shift saturates while the decay time continues to decrease. As stated previously, at high doses the large number of defects necessary to produce intermixing are no longer generated in QW3 and QW4. However, a number of defects produced in the near surface region will diffuse inwards during the annealing process (but obviously not a sufficient number to induce measurable intermixing in QW3 and QW4). These defects, however, can act as nonradiative decay centres leading to the observed decrease in the decay times

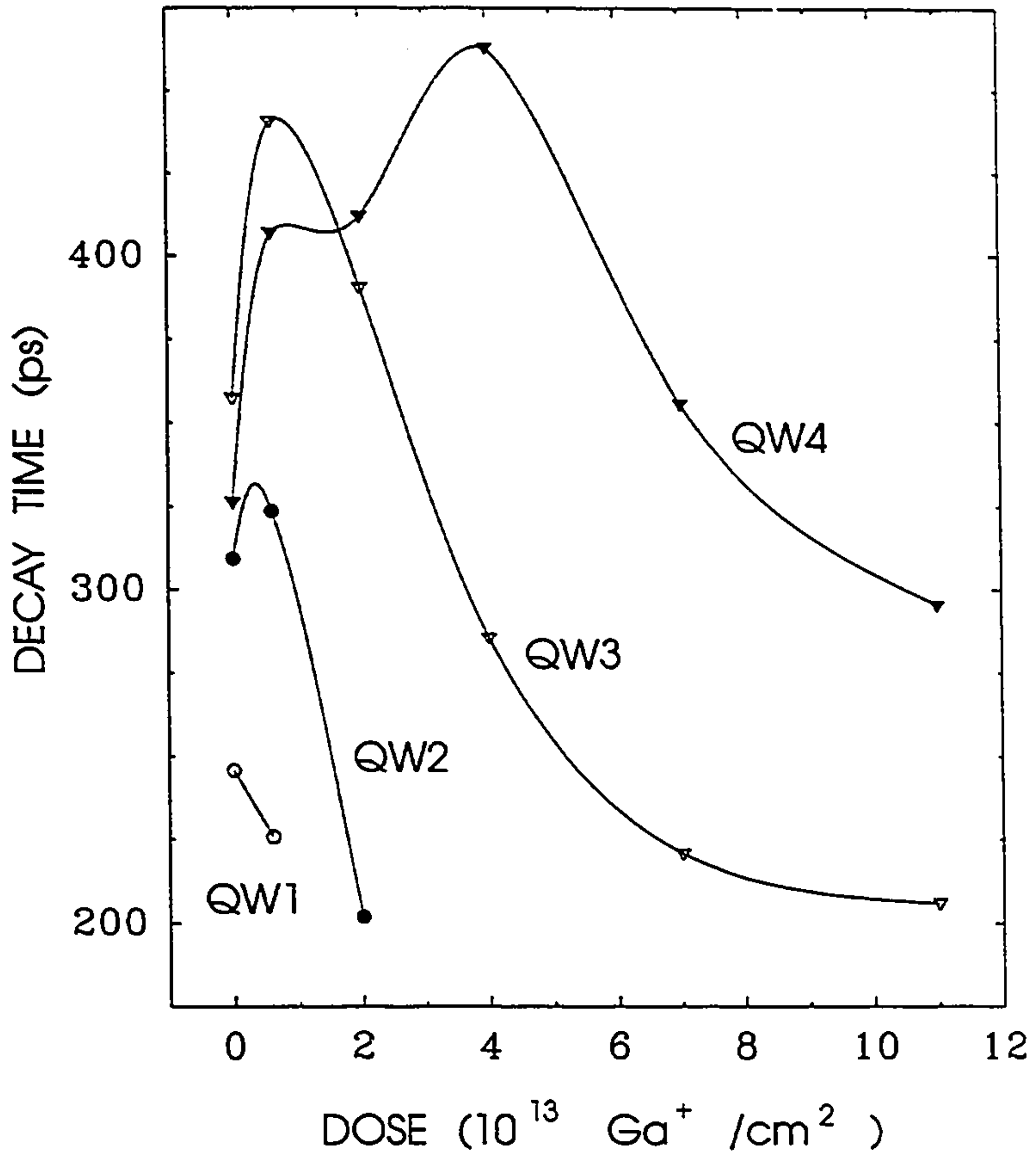

Fig. 3.23 Ga^+ dose dependence of the PL peak intensity decay time for the four quantum well emission peaks of sample 1020.

at larger doses. This interpretation is consistent with the observed incomplete recovery of the PL intensity after annealing at higher doses.

The initial rise in the decay time at lower doses shown in Fig. 3.23 remains to be explained. One possibility is that the broadening of the well by interdiffusion leads to a reduction in the overlap of the electron and hole wavefunctions and thus to an increase in the radiative decay time. However, a calculation of the overlap as a function of interdiffusion yields only small changes (3 or 4%). The observed PL peaks within a QW arise from the decay of both free and bound excitons. We have resolved these two exciton lines for QW1 and QW2 where the indium concentration is low, leading to narrow emission line shapes (these doublet structures are not observable in Fig. 3.9 due to the lower resolution used in the acquisition of these particular spectra). The lifetime of bound excitons in the AlGaAs/GaAs system has been reported to be at least 15% longer than for free excitons[3.51]. By analogy we expect that any process that increases the bound-to-free exciton ratio in the present system will increase the decay time. It would appear that the initial disordering results in an increase in binding sites for the excitons. This is consistent with the observation that the PL intensity only begins to decline when the decay time does, although at this time we do not have a microscopic picture for such binding sites. As the dose is increased, nonradiative sites begin to dominate and the observed decay time is then controlled by the nonradiative recombination term and

therefore the observed lifetime decreases. The results for QW1 are confined only to very low doses but do not show the initial rise in decay time. This well is within the mean range, R_p, from the surface and thus receives a substantially bigger fraction of the dose delivered to the surface than the deeper wells. Consequently, measurements on this well are always in the high-dose regime.

An example of the time behaviour of the PL signal for three different implanted doses is given in figure 3.24. We can see the clear exponential behaviour in every case.

3.8 Discussion

This chapter was concerned with many aspects of ion implantation. The main results are summarized here.

Firstly, channelling effects were studied and the results showed that in order to compositionally disorder quantum wells lying deep beneath the sample's surface, channelling must occur. Following this, an attempt to fabricate quantum well wires and quantum well boxes in InGaAs/GaAs strained QW's was made. To do this, FIB patterned implantation was carried out for doses ranging from 0.6 to 11 x 10^{13} Ga^+/cm^2. The periodicity of the implanted patterns was also varied (recall section 3.4). The steady state PL study that followed showed no evidence of QW wire or QW box formation for any of the dose/pattern-periodicity combinations. In fact, the results obtained showed no evidence of periodic

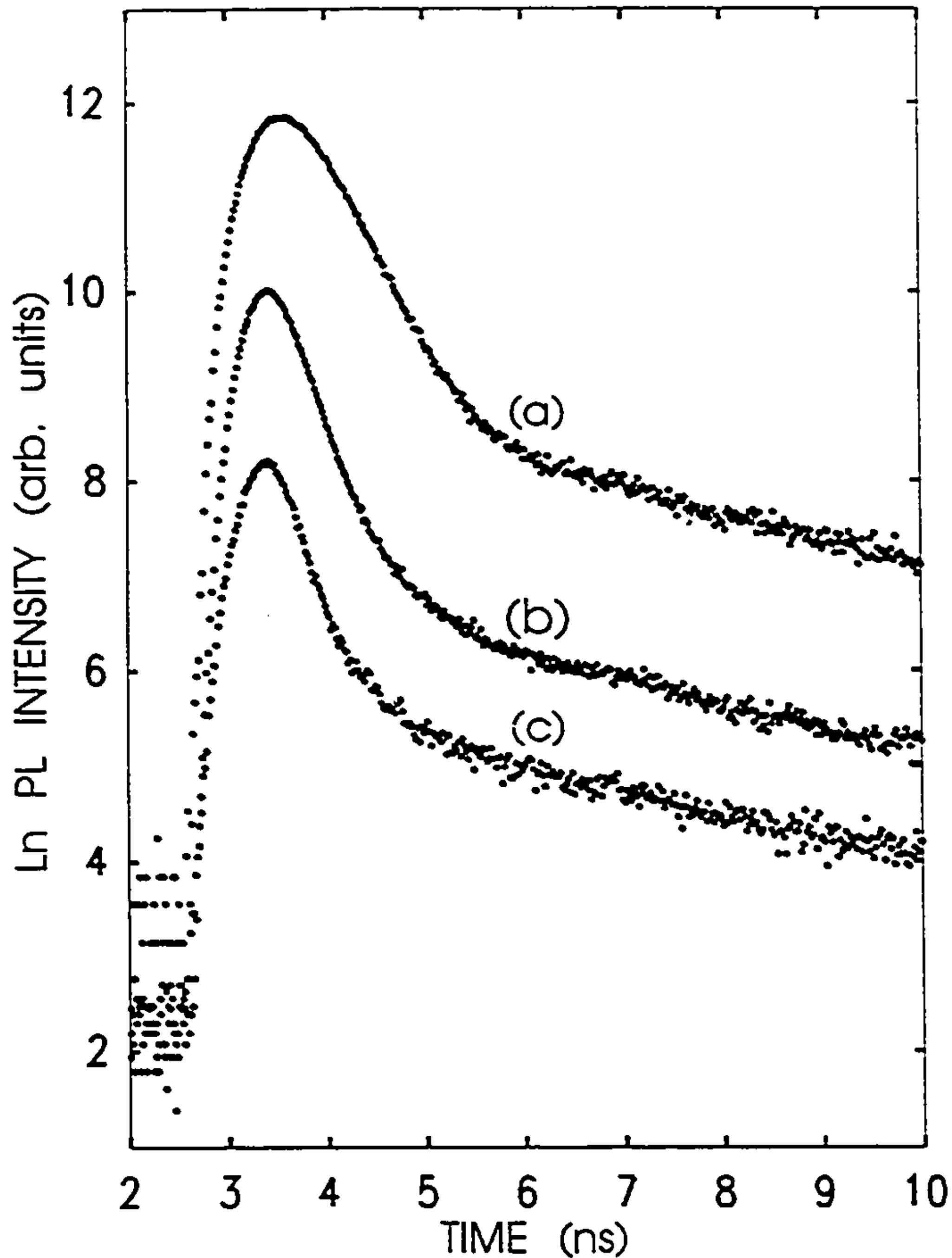

Fig. 3.24 PL peak decay measurements (5K) of the n=1 heavy hole exciton taken from QW3 of sample 1020 at three uniformely implanted doses: (a) virgin material, (b) $7x10^{12}$ Ga^{+}/cm^{2}, and (c) $11x10^{12}$ Ga^{+}/cm^{2}. The lifetimes corresponding to the initial exponential decays are 410, 320 and 280 ps respectively.

compositional disordering as would be expected (this would have been seen if two PL peaks, one associated with the virgin material and one associated with the compositionally disordered material, were detected). This was a surprising result and prompted the following hypotheses to explain it: (1) The InGaAs/GaAs QW system studied is a strained system. The effect that strain might have on the lateral migration of the FIB-created defects during the post-implantation RTA could play a (yet undetermined) role in the observations. The extent of the lateral migration would have to be of the order of 1 µm to explain the result; (2) The minimum dose required (critical dose) to intermix InGaAs/GaAs QW's is so low that the tail dose of the FIB would be sufficiently high to induce compositional disordering in "unimplanted" regions. This tail extends over 0.6 µm away from the beam center and is $\sim 10^{-4}$ times less intense than the center-beam value.

The first hypothesis was not tested. The critical dose hypothesis was however tested by implanting InGaAs/GaAs QW structures with very low doses and carrying PL measurements after RTA. The results clearly showed that the critical dose is in fact much lower than the lowest dose implanted in our initial QW wire and QW box formation attempt. This result that was not comparable to that obtained from similar studies on AlGaAs/GaAs QW structures. Our study unambiguously showed that the reason no QW wires or boxes were formed using the FIB disordering technique had to do with the "high dose" regime in which the patterned implantation were done. The lateral defect migration hypothesis could also play a role but

remains to be tested.

Chapter 4

Two Dimensional Time-Resolved Photoluminescence Imaging

4.1 Introduction

The transport properties of carriers in semiconductor heterostructures have received much attention over the last decade for both fundamental and practical purposes. Many techniques have been developed to gain knowledge of these properties; these include Hall effect measurements[4.1], time-and-space-resolved Raman spectroscopy (TSRR)[4.2], optical four-wave mixing[4.3] and time-of-flight (TOF) PL[4.4] among others.

In this chapter, we will show how the PL setup described in chapter 2 can be utilized to measure the diffusion coefficient of electron-hole pairs in an AlAs/GaAs multiple quantum well (MQW) structure. Results of diffusion coefficient Vs. temperature for a fixed excitation intensity will be given. Preliminary results of the diffusion coefficient Vs. excitation intensity for a fixed temperature will also be shown.

4.2 Temperature Dependence of the Diffusion Coefficient

The optical excitation setup used in this experiment is that of figure 2.8 where the exciting laser beam is focused onto the

sample's surface to a size of ~5 μm. As previously stated, this acts as a localized source of photo-excited electrons and holes whose subsequent expansion is monitored by detecting the light emitted as the carriers recombine.

Steady state PL measurements of our 30 period AlAs/GaAs MQW sample (70.0 nm barrier, 9.3 nm well) have shown us that the emitted PL signal from the quantum wells is spectrally located at a wavelength of ~790 nm at 80 K. In order to perform our 2D TR PL imaging we have used a 715 nm long wave pass filter as our wavelength-selecting element. A PL spectrum taken at 86 K together with the PL decay for this sample was shown in Fig. 2.6.

The 2D TR PL acquisition setup was set to acquire the digitized 2D images in 16 time-windows partitioning the TAC setting. The total acquisition time for each scan (one scan per temperature) was 100 minutes. This was done for temperatures ranging from 80 to 300 K. Figure 4.1 gives an example of four 2D TR PL imaged time-windows. We clearly see the electron/hole cloud expand from its initial radius (a) through (d) which is some 60 ns later.

The diffusion coefficient, D, of the photogenerated electron/hole cloud can be extracted from such 2D time-windowed PL data. To do so, we consider the 2D diffusion equation expressed in cylindrical coordinates

$$\frac{\partial n}{\partial t}=D\frac{1}{\rho}\frac{\partial}{\partial \rho}\left(\rho\frac{\partial n}{\partial \rho}\right)-\frac{n}{\tau} \qquad (4.1)$$

where ρ is the radial coordinate, n is the density (exciton density

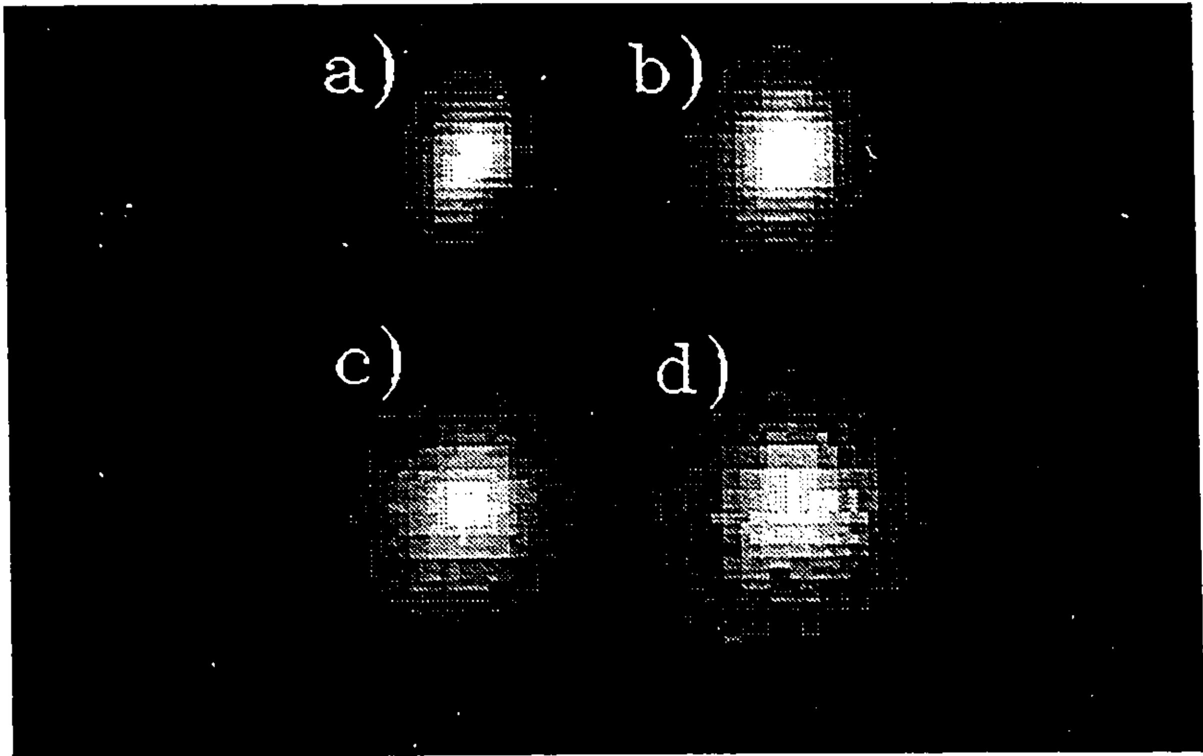

Fig. 4.1 2D TR PL spatial images of photogenerated carriers at room temperature. The scaling factor, HWHM and time-window (Δt) of the spatial images are, respectively, as follows: (a) 1.0, 5.9μm, 0-6.25ns; (b) 2.8, 8.2μm, 18.75-25ns; (c) 8.1, 9.9μm, 37.5-43.75ns; (d) 21.6, 11.1μm, 62.5-68.75ns.

or e-h pair density depending on the regime in which measurements are carried out) and τ the recombination time. If one assumes an initially Gaussian-shaped distribution, equation (4.1) yields the following solution

$$n(\rho,t)=\frac{\sigma_o^2 n_o}{4Dt+\sigma_o^2}\exp\left(-\frac{t}{\tau}\right)\exp\left(-\frac{\rho^2}{4Dt+\sigma_o^2}\right) \qquad (4.2)$$

which gives the following relationship between the square of the FWHM of each 2D PL time-window and time:

$$\Delta^2(t)=\Delta_o^2+11.09Dt \qquad (4.3)$$

where Δ_o is the initial FWHM (Δ_o^2=4ln(2)σ_o and σ_o is the initial 1/e half width). Thus, by measuring the FWHM of the 2D time-windows at various times, a plot of $\Delta^2(t)-\Delta_o^2$ Vs. time would yield a slope from which the value of D could be extracted for the temperature and excitation intensity used in the acquisiton. We show in Fig. 4.2 the diffusion coefficient Vs. temperature data obtained for our MQW sample. The excitation intensity was 2×10^{12} /cm^2. Also shown is the carrier recombination time Vs. temperature curve for the same excitation intensity. These lifetimes were measured using the time-correlated single photon-counting setup and spectrometer system described in chapter 2.

Hillmer and coworkers[4.4] used the TOF method to obtain the diffusion coefficient of 2D excitons in (Al,Ga)As/GaAs QW structures. They studied this, together with carrier lifetime, as a function of well width and temperature. They found a temperature dependence of the diffusion coefficient similar to ours. That is,

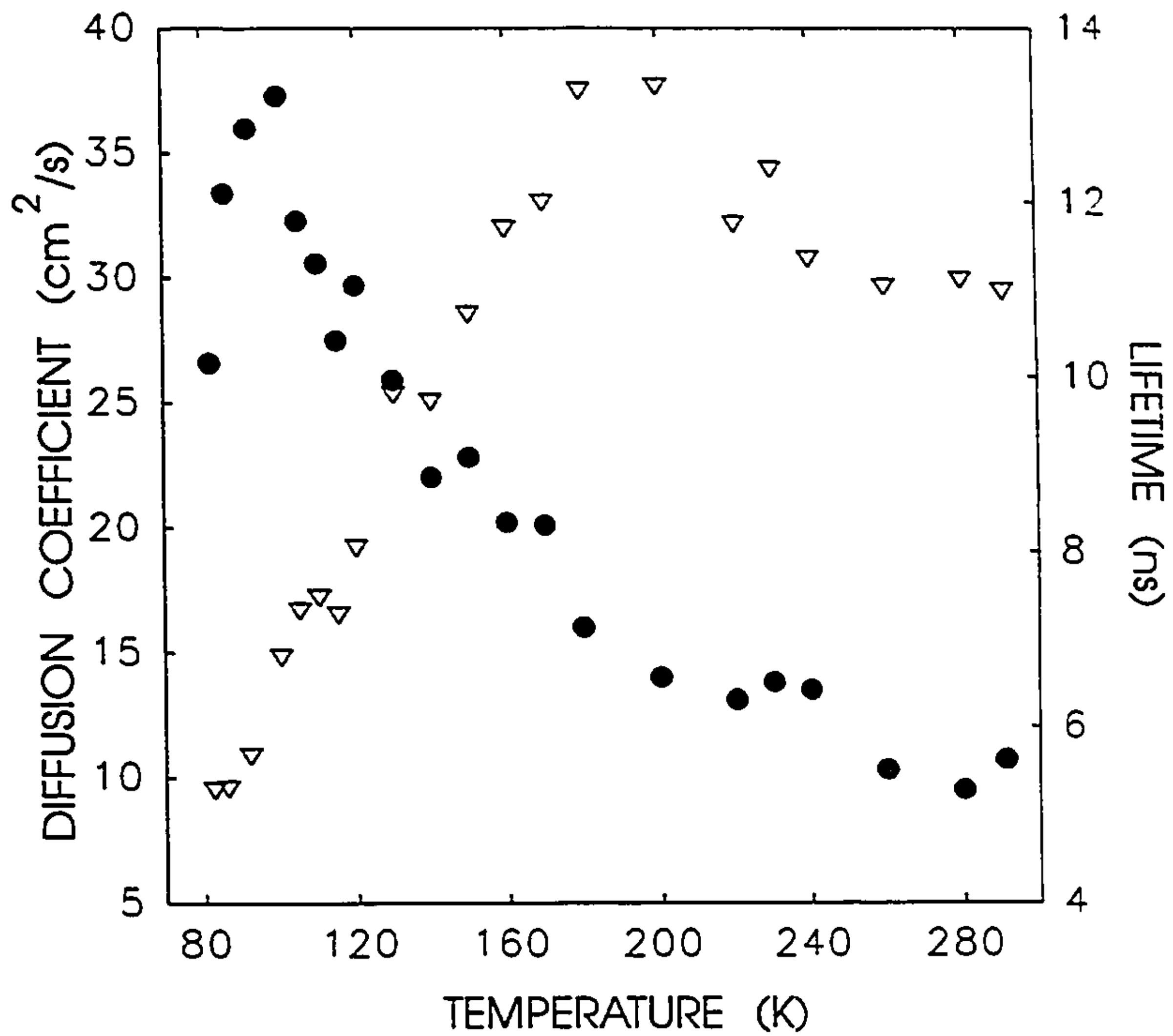

Fig. 4.2 Diffusion coefficient (circles) and carrier lifetime (triangles) Vs. temperature for optically generated carriers in our AlAs/GaAs MQW sample. The diffusion coefficient is obtained from data similar to that of Fig. 4.1.

as the temperature rises from 80 to 100 K, D increases, goes through a maximum and then decreases. They reported that their data was best fitted if the scattering mechanisms taking place were of excitonic nature as opposed to ambipolar. They attributed the rise in the diffusivity data (from 80 to 100 K) as a decrease of the scattering process due to interface roughness as the temperature was increased. The subsequent fall of D (for T > 100 K) was attributed to the eventual dominance of phonon and barrier-alloy-scattering with further temperature rise.

The recombination time Vs. temperature data we gathered also shows the same behaviour as that reported Hillmer et al.[4.4] An initial rise with temperature followed by a decrease. Previous studies on similar samples showed that the rise of the lifetime with temperature is attributable to k-space localization[4.5]. That is, as the temperature rises, the fraction of excitons at K=0 decreases thereby yielding an increase in lifetime since only excitons with K=0 can decay (momentum conservation rule). The decrease in lifetime as the temperature is brought up even further (T > 200 K) is attributable to thermal dissociation of excitons, phonon scattering, interface recombination and occupation of higher bands[4.4].

These measurements have been repeated to show that the novel PL setup we developed was capable of reproducing, in a much simpler fashion, results obtained by more complicated and time-consuming techniques. This has been demonstrated by showing results of D Vs. temperature and τ Vs. temperature data which qualitatively match

that obtained by the TOF method.

4.3 Diffusion coefficient Vs. excitation intensity

We found in the preceding section that the diffusion Vs. temperature data for an injected carrier density of ~2 x $10^{12}/cm^2$ qualitatively matched the data of Hillmer and coworkers[4.4]. Whether the behaviour of the diffusion curve of Fig. 4.2 is best fitted by ambipolar as opposed to exciton-like scattering was not considered since it was shown[4.6] that for carrier densities larger than 1 x $10^{11}/cm^2$, the diffusion is ambipolar.

Thus, having shown that our experimental setup was well-suited for 2D diffusion measurements, we carried out such measurements at a fixed temperature of 80 kelvin as a function of excitation intensity. The corresponding PL decay measurements were also taken.

We first show the PL decay results, Fig. 4.3 and then the FWHM data from which the diffusion coefficients are obtained (via equation (4.3)), Fig. 4.4.

We clearly see the transition from "slow" to "fast" lifetime as the excitation intensity is lowered. This can be explained by carriers diffusing ambipolarely at high density and by behaving more like excitons as the excitation intensity is decreased. The PL decay lifetime of the high carrier density curve (a) is 7.0 ns whereas that of the low density curve, (d), is 1.1 ns. This

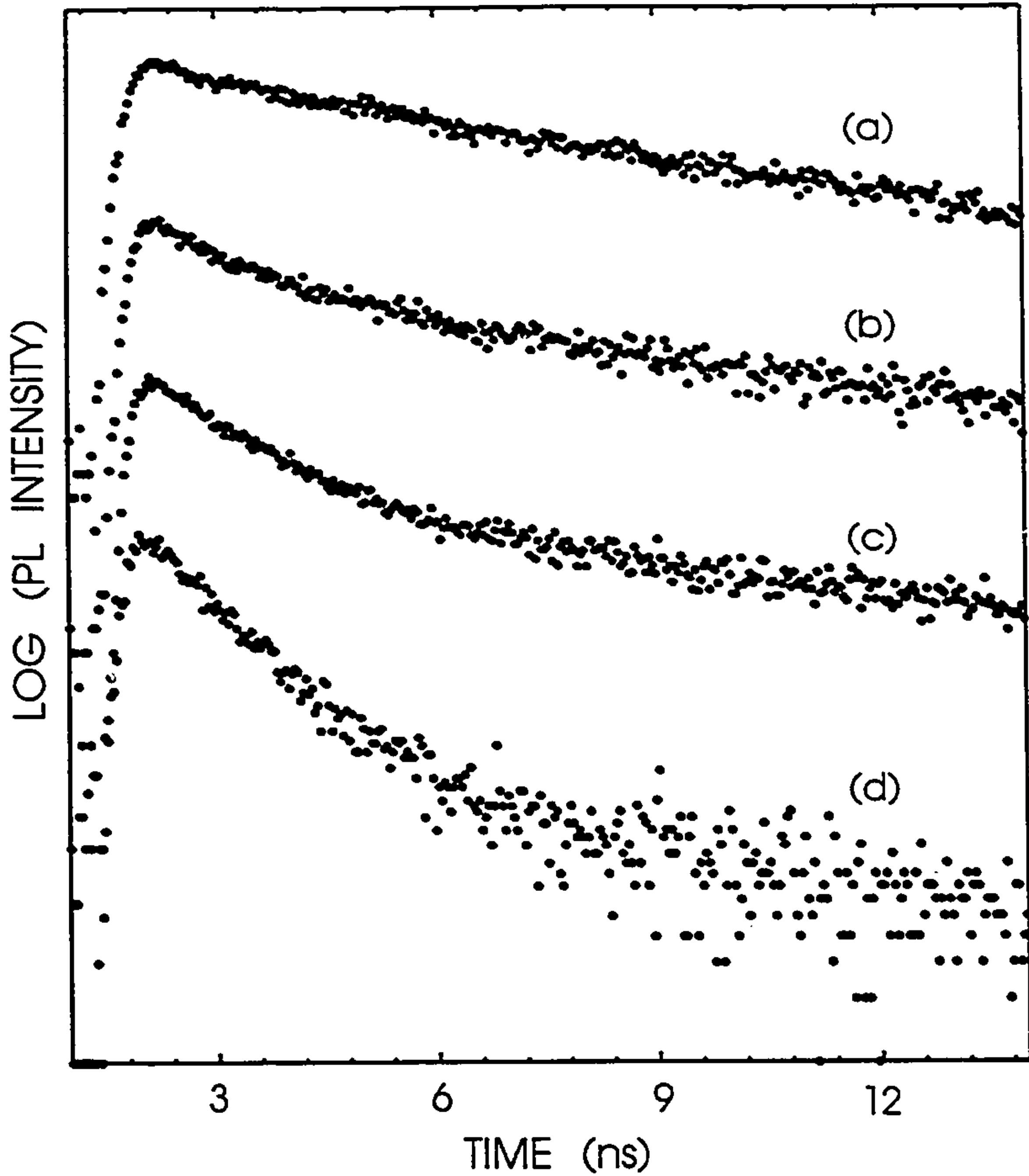

Fig. 4.3 PL decay of AlAs/GaAs MQW sample for four injected carrier densities. (a) $6 \times 10^{12} cm^{-2}$, (b) $6 \times 10^{11} cm^{-2}$, (c) $1.9 \times 10^{11} cm^{-2}$, (d) $1.9 \times 10^{10} cm^{-2}$. The curves are normalized and offset for clarity. The transition from a monoexponential long lifetime to a short lifetime curve follows the passage from high excitation to lower excitation.

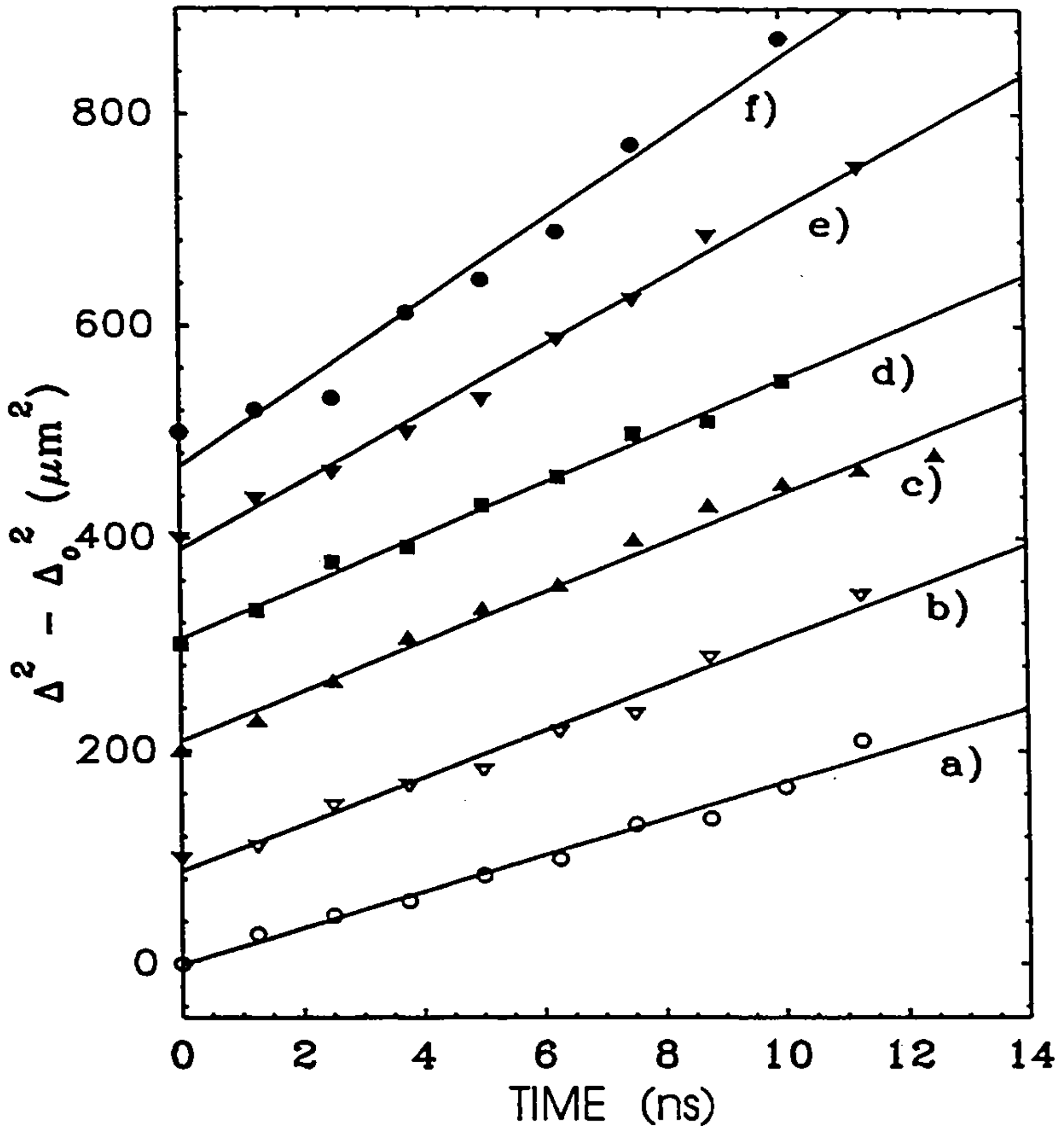

Fig. 4.4 FWHM data obtained using equation (4.3). The injected carrier densities and diffusion coefficients are : (a) 1.9×10^{10} cm^{-2} , 16 cm^2/s; (b) 6×10^{10} cm^{-2} , 20 cm^2/s; (c) 1.9×10^{11} cm^{-2} , 21 cm^2/s; (d) 6×10^{11} cm^{-2} , 22 cm^2/s; (e) 1.9×10^{12} cm^{-2} , 29 cm^2/s; (f) 6×10^{12} cm^{-2} , 35 cm^2/s. The curves a), b), c), d), e) and f) are offset by 0, 100, 200, 300, 400 and 500 microns square for clarity purposes.

behaviour is attributable to the momentum relaxation time which is longer for plasma than for excitons[4.4].

The increase in the diffusion coefficient as a function of excitation intensity, Fig. 4.4, is equally interesting and indicates also that one must consider ambipolar diffusion as the carrier density is increased since the model of two independent particles (electron and hole) diffusing yields higher mobilities than that of excitonic diffusion[4.4] . The diffusion coefficient seems to change considerably between curves (d) and (e). This indicates that studies with higher intensities would be needed in order to see a further increase in the diffusion coefficient.

Another interesting experiment would be to carry out 2D TR PL imaging on uniformly implanted QWs structures. One could thus observe the variation of the diffusion coefficient as the quantum well band structure goes from a square profile to a more parabolic-looking one and thus assess the effect of gradual bandgap discontinuity on carriers and exciton diffusion in implanted material. These measurements could prove to be very important for the future application of optoelectronic/monolithic integration in semiconductor materials where bandgap tuning by QW disordering appears to be the key for future progress in this field.

Chapter 5

Conclusion

In this work, we have reported on the photoluminescence studies of two-dimensional semiconductor heterostructures. We have shown results of ion implantation in quantum wells along with preliminary results on two-dimensional carrier diffusion in quantum wells also.

More specifically, we have shown how ion implantation, followed by annealing, in QW's leads to compositional disordering and have presented a simple formalism permitting the calculation of interdiffusion lengths from PL peak energy shifts measurements. The implantation apparatus used for the most part was an FIB implanter whose major appeal is that it can perform patterned implantation without requiring a lay out of masks. This reduces the number of processing steps required for the fabrication of potential devices and thus yields devices of better optical quality.

The fact that the FIB implanter is limited in the energy it can give to ions implies that the range that these can reach in the target material is limited. This prompted us to study the channeling of these mid-energy range ions. We demonstrated through SIMS measurements the importance of the channeling effect. We showed that to disorder QW's located beyond the expected range of the ions, channeling must occur and that it is maximized when impinging ions are aligned parallel to the <100> crystal axis.

Photoluminescence studies of wire-and-box-patterned regions of our QW samples indicated that compositional disordering was occurring at distances of the order of 1 µm away from implanted regions. This meant that there was either in-plane migration of defects occurring over these large distances or that the threshold dose required to observe intermixing in InGaAs/GaAs QW's was so low that the tail dose of the FIB profile was sufficient to intermix these "unimplanted" regions. To assess which of these possibilities was more probable, we undertook studies of low dose, 8 MeV Bi^+ ions, implantation in InGaAs/GaAs. We did the same for AlGaAs/GaAs QW's since data for these had already been reported; the results we obtained compared very well with those published[3,47]. As for the 8 MeV implantation in InGaAs/GaAs QW's, we found the threshold dose to be two order of magnitude lower than for AlGaAs/GaAs. This indicates that the FIB profile tail dose ($\sim 10^4$ times less than the beam center dose) would indeed be sufficient to induce intermixing at distances of about 0.5 µm away from the beam center if this center dose is in the 10^{13} cm^{-2} regime. Furthermore, the fitted interdiffusion lengths for the InGaAs/GaAs structures increased with the indium content of the well and implanted dose. This result supports the argument that strain and indium cross-section effects are the primary factors lowering the threshold dose for QW intermixing.

We have also reported on the doping behaviour of implanted Si^+ ions and on the effect of implanted dose on exciton lifetime.

The other major part of this work was the development of a low

light level optical detection system that can be easily configured for various PL modes of operation. These include (1) steady state PL, (2) transient, spectrally gated PL decay, (3) time-windowed PL, (4) two-dimensional, time-integrated PL mapping, and (5) time-resolved, two-dimensional PL mapping with 100 ps time resolution.

We have shown preliminary results of time-resolved two-dimensional PL mapping of an AlAs/GaAs multiple quantum well structure as a function of temperature and of excitation intensity. The results obtained for the diffusion coefficient as a function of temperature compare well with those obtained by the more complicated time-of-flight technique[4.4].

To establish a strong link between ion implantation and two-dimensional time-resolved PL mapping, it would be interesting to measure the diffusion coefficient of carriers generated in uniformly implanted quantum wells for the reasons mentionned in the previous chapter.

References

Chapter 1

1.1 A.Y. Cho and J.R. Arthur, Prog. Solid State Chem. 10, 157 (1975).

K. Ploog, in "Crystals: Growth, Properties and Applications", H.C. Freyhardt ed., Vol. 3, p.75, Springer-Verlag Berlin and New York (1980).

L.L. Chang, in "Handbook of Semiconductors", T.S. Moss ed., Vol. 3, P. 563, North-Holland Publ. Amsterdam (1980).

1.2 Robert S. Knox, Theory of Excitons, Solid State Physics, Supplement 5, Academic Press, New York (1963).

1.3 J. Frenkel, Phys. Rev. 37, 1276 (1931).

G.H. Wannier, Phys. Rev. 52, 191 (1937).

N.F. Mott, Proc. R. Soc. A 167, 384 (1938).

1.4 Claude Cohen-Tannoudji, Bernard Diu, and Franck Laloë. Quantum Mechanics, Vol. 2, Complement A_{XIII}. Wiley-Interscience New York (1977).

1.5 E.I. Rashba in "Excitons at High Density", Pp. 150-169, edited by H.Haken and S. Nikitine. Springer-Verlag, New York (1975).

1.6 D.L. Dexter in "Solid State Physics: Advances in Research and Applications", Pp. 353-411, edited by Frederick Seitz and David Turnbull. Academic Press, New York (1958).

1.7 L.L. Chang, L. Esaki, W.E. Howard, L. Ludeke, and G. Schul, J. Vac. Sci. Technol. 10, 655 (1973).

1.8 R. Dingle et al., Appl. Phys. Lett. 33, 665 (1978).

1.9 L. Esaki and R. Tsu, IBM J. Res. Develp. 14, 61 (1970).

1.10 H. Kroemer in "Molecular Beam Epitaxy and Heterostructures", NATO ASI Series, Martinus Nijhoff Publ. (Dordrecht 1985), pp. 358-365.

1.11 R. Dingle, W. Wiegmann, and C.H. Henry, Phys. Rev. Lett. 33, 827 (1974).

1.12 J.M. Rorison and D.C. Herbert, Superlattices and Microstructures, Vol. 1, No. 5, 423 (1985).

1.13 Garnett W. Bryant, Phys. Rev. B 37, 8763 (1988).

1.14 P.J. Dean, Prog. Cryst. Growth Charact. 5, 89 (1982).

E.C. Lightowlers, Growth and Characterization of Semiconductors, R.A. Stadling and P.C. Klipstein eds., Pp. 135-163 (1990).

1.15 S. Charbonneau, L.B. Allard, A.P. Roth, and T. Sudersena Rao, Phys. Rev. B 47, 13918 (1993).

1.16 S. Charbonneau, Optical Eng. 28 (10), (1989).

1.17 K. Kash. Journal of Luminescence 46, Pp. 69-82 (1990).

1.18 H. Hillmer, A. Forchel, S. Hansmann, M. Morohashi, E. Lopez, H.P. Meier, and K. Ploog, Phys. Rev. B 39, 10901 (1989).

Chapter 2

2.1 F.J. McClung and R.W. Hellworth, J. Appl. Phys. 33, 838 (1962).

2.2 H.W. Moker and R.J. Collins, Appl. Phys. Lett. 7, 270 (1965).

2.3 Orazio Svelto, Principles of Lasers (Plenum, New York 1982).

Dye Laser Principles, ed. by F.J. Duarte and Lloyd W. Hellman (Academic Press, Toronto 1990).

W. Demtröder, Laser Spectroscopy (Springer, Berlin 1982).

Peter W. Milonni and Joseph H. Eberly, Lasers (John Wiley & Sons, Toronto 1988).

2.4 Dye Lasers 2nd edition, F.P. Schäfer ed., Topics in Applied Physics, Vol. 1 (Springer, New York 1978).

J.W. Small, The Dye Laser in Physics of Quantum electronics, Vol. 4 (Addison-Wesley, London 1976).

2.5 W. Demtröder, Laser Spectroscopy (Springer, Berlin 1982), page 7.

2.6 W. Demtröder, Laser Spectroscopy (Springer, Berlin 1982), Pp. 178-182.

2.7 K. Thyagarajan and A.K. Ghatak, Lasers: Theory and Applications (Plenum Press, New York 1981), p. 127.

2.8 P.A. Franken et al., Phys. Rev. Lett. 7, 118 (1961).

2.9 Orazio Svelto, Principles of Lasers (Plenum, New York 1982), p. 322.

2.10 Chuangtian Chen, Yicheng Wu, Aidong Jiang, Bochang Wu, Guiming You, Rukang Li, and Shujie Lin, J. Opt. Soc. Am. B 6 (4) 616.

Baichang Wu, Nong Chen, Chuangtiang Chen, Daoqun Deng, and Zuyan Xu, Optics Letters 14 (19) 1080.

Shujie Lin, Zhaoyang Sun, Bochang Wu, and Chuangtian Chen, J. Appl. Phys. 67 (2) 634.

W.S. Pelouch, T. Ukachi, E.S. Wachman, and C.L. Tang, Appl. Phys. Lett. 57 (2) 111.

2.11 W.H. Glenn, M.J. Brienza, and A.J. DeMaria, Appl. Phys. Lett. 12, 54 (1968).

2.12 Amnon Yariv, Quantum Electronics, Third Edition, Chapter 14 (John Wiley & Sons, Toronto 1988).

2.13 (a) C.A. Murray and S.B. Dierker, J. Opt. Soc. Am. A 3, 2151 (1986).

(b) Y. Talmi and R.W. Simpson, Appl. Opt. 13, 1401 (1980).

(c) M. Lampton and C.W. Carlson, Rev. Sci. Instrum. 50, 1093 (1979).

(d) D. Rees, I. McWhirter, P.A. Rounce, F.E. Barlow, and S.J. Kellock, J. Phys. E 13, 763 (1980).

(e) D. Rees, I. McWhirter, P.A. Rounce, and F.E. Barlow, J. Phys. E 14, 229 (1981).

(f) I. McWhirter, D. Rees, and A.H. Greenaway, J. Phys. E 15, 145 (1982).

(g) R.S. Goa, P.S. Gibner, J.H. Nauman, K.A. Smith, and R.F. Stebbings, Rev. Sci. Instrum. 55, 1756 (1984).

(h) I. Yamazaki, N. Tamai, H. Kume, H. Tsuchiya, and K. Oba, Rev. Sci. Instrum. 56, 1187 (1985).

(i) H. Kume, K. Koyama, K. Nakatsugawa, S. Suzuki, and D. Fatlowitz, Appl. Opt. 27, 1170 (1988).

(j) R.F. Floryan and C.B. Johnson, Rev. Sci. Instrum. 60, 339 (1989).

2.14 J.H. Timothy and R.L. Bybee, Appl. Opt. 14, 1632 (1975).

G. Pietry, IEEE Trans. Nucl. Sci. NS-22, 2084 (1975).

M. Audier and J.P. Boutot, Philips Res. Rep. 30, 226 (1975).

J.G. Timothy and R.L. Bybee, Rev. Sci. Instrum. 46, 1615 (1975).

2.15 M. Lampton and F. Paresce, Rev. Sci. Instrum. 45, 1098 (1974).

G.M. Lawrence and E.J. Stone, Rev. Sci. Instrum. 46, 432 (1975).

H. Weiser, R.C. Vitz, H.W. Moos, and A. Weinstein, Appl. Opt. 15, 3123 (1976).

2.16 References 2.13(c)-(j).

2.17 W.G. McMullan, S. Charbonneau, and M.L.W. Thewalt, Rev. Sci. Instrum. 58, 1626 (1987).

2.18 S.H. Courtney and W.L. Wilson, Rev. Sci. Instrum. 62, 2100 (1991).

2.19 T.W. Steiner, M.L.W. Thewalt, M. Maciaszek, and R.P. Bult, Can. J. Phys. 69, 333 (1991).

2.20 I.M. Templeton, private communication.

2.21 R.L. Williams, M. Dion, F. Chatenoud and K. Dzurko, Appl. Phys. Lett. 58, 1816 (1981).

Chapter 3

3.1 P. Sigmund and J.B. Saunders, Proc. Int. Conf. Applications of Ion Beams to Semiconductor Technology, ed. P. Glotin (Centre d'Études Nucléaires, Grenoble 1967), p. 215.

3.2 M.T. Robinson in "Radiation Induced Voids in Metals", ed. J.W. Corbett and L.C. Ianiello, U.S. Atomic Energy Commission Office of Implantation Services, April 1972, p. 397.

3.3 B.R.T. Frost, IEEE Transactions on Nuclear Science NS-19, No. 6, p. 234, December 1972.

J.R. Beeler Jr., Applications of Ion Beams to Metals, ed. S.T. Picraux, E.P. EerNisse, and F.L. Vook, Plenum Press New York, 1974, p. 651.

O.S. Oen, J. Narayan, and T.S. Noggle, Applications of Ion Beams to Metals, ed. S.T. Picraux, E.P. EerNisse, and F.L. Vook, Plenum Press New York, 1974, p. 639.

K.L. Brower, F.L. Vook, and J.A. Borders, Appl. Phys. Lett. 16, p. 108 (1970).

H.J. Stein, F.L. Vook, and J.A. Borders, Appl. Phys. Lett. 16, p. 106 (1970).

3.4 J.F. Ziegler, The Stopping and Range of Ions in Matter, IBM Research, RC8907 (#39047), 6/30/81.

3.5 J.W. Mayer, L. Erikson, and J.A. Davies, Ion Implantation, Academic Press, New York 1970.

3.6 W.L. Brown, T. Venkatesan, A. Wagner, Solid State Technology 24 (8), p. 60 (1981).

Alfred Wagner, Solid State Technology 26 (5), p. 97 (1983).

3.7 J.R.A. Cleaver, P.J. Heard, and H. Ahmed, Microcircuit Engineering 82 (Proceedings of the International Conference on Microlithography, Grenoble, France, 1982), P. 148.

R.L. Kubena, C.L. Anderson, R.L. Seliger, R.A. Jullens, E.H. Stevens, and I. Lugnado, J. Vac. Sci. Technol. 19, p. 916 (1981).

R.L. Seliger, R.L. Kubena, and V. Wang, Jpn. J. Appl. Phys. 21, Supplement 21-1, 3 (1982).

Y. Bamba, E. Miyauchi, H. Arimoto, K. Kuramoto, A. Takamori, and H. Hashimoto, Jpn. J. Appl. Phys. 22, L650 (1983).

Y. Bamba, E. Miyauchi, H. Arimoto, K. Kumamoto, A. Takamori, and H. Hashimoto, Jpn. J. Appl. Phys. 23, L515 (1984).

R.H. Reuss, D. Morgan, E.W. Greeneich, W.M. Clark Jr., and D.B. Rensch, J. Vac. Sci. Technol. B 3, p. 62 (1985).

H. Hamadeh, J.C. Corelli, and A.J. Steckl, J. Vac. Sci. Technol. B 3, p. 91 (1985).

3.8 H. Yamaguchi, A. Shimase, S. Haraichi, and T. Miyauchi, J. Vac. Sci. Technol. B 3, p. 71 (1985).

Y. Ochiai, K. Gamo, and S. Namba, J. Vac. Sci. Technol. B 1, p. 1047 (1983).

Y. Ochiai, K. Gamo, and S. Namba, J. Vac. Sci. Technol. B 3, p. 67 (1985).

3.9 J.M. Chabala, R. Levi-Setti, and Y.L. Wang, J. Vac. Sci. Technol. B 6 (3), p. 910 (1988).

3.10 Z. Nakagawa, S. Sakaki, M. Sato, J. Glanville, and M. Yamamoto, J. Vac. Sci. Technol. B 6 (3), p. 1030 (1988).

Alfred Wagner, Solid State Technology 26 (5), May 1983).

3.11 J. Hiramoto, K. Hirakawa, Y. Iye, and T. Ikoma, Appl. Phys. Lett. 51, p. 1620 (1987).

3.12 T. Shiokawa, K. Ishibashi, P.H. Kim, Y. Aoyagi, K. Toyoda, and S. Namba, Jpn. J. Appl. Phys. 29, p. 2864 (1990).

3.13 Y. Hirayama, Y. Suzuki, and H. Okamoto, Surf. Sci. 174, p. 98 (1986).

Y. Hirayama, S. Tarucha, Y. Suzuki, and H. Okamoto, Phys. Rev. B 37, p. 2774 (1988).

3.14 Y. Hirayama and T. Saku, Appl. Phys. Lett. 54, p. 2556 (1989).

3.15 K. Ensslin and P.M. Petroff, Phys. Rev. B 41, p. 12307 (1990).

3.16 S. Sasa, M.S. Miller, Y.J. Li, Z. Xu, K. Ensslin, and P.M. Petroff, Appl. Phys. Lett. 57, p. 2259 (1990).

3.17 J.F. Ziegler, J.P. Biersack, and U. Littmark, The Stopping and Range of ions in Solids, Pergamon, New York (1985).

3.18 P.M. Petroff, Xueyu Quian, P.O. Holtz, R.J. Simes, J.H. English, J. Merz, and R. Kubena, Mater. Res. Soc. Symp. 126, 55 (1988).

F. Laruelle, P. Hu, R. Simes, R. Kubena, W. Robinson, J. Merz, and P.M. Petroff, J. Vac. Sci. Technol. B 7, 2034 (1989).

F. Laruelle, A. Bagchi, M. Tsuchiya, J. Merz, and P.M. Petroff, Appl. Phys. Lett. 56, 1561 (1990).

H. Temkin, L.R. Harriot, R.A. Hamm, J. Winer, and M.B. Panish, J. Vac. Sci. Technol. B 7, 1467 (1989).

3.19 J.F. Ziegler, J.P. Biersack, and U. Littmark, The Stopping and Range of Ions in Matter (Pergamon, New York, 1985), Vol. 1.

3.20 P.M. Petroff, Xueyu Quian, P.O. Holtz, R.J. Simes, J.H. English, J. Merz, and R. Kubena, Mater. Res. Soc. Symp. 126, 55 (1988).

F. Laruelle, P. Hu, R. Simes, R. Kubena, W. Robinson, J. Merz, and P.M. Petroff, J. Vac. Sci. Technol. B 7, 2034 (1989).

F. Laruelle, A. Bagchi, M. Tsuchiya, J. Merz, and P.M. Petroff, Appl. Phys. Lett. 56, 1561 (1990).

3.21 P.M. Petroff, Xueyu Quian, P.O. Holtz, R.J. Simes, J.H. English, J. Merz, and R. Kubena, Mater. Res. Soc. Symp. 126, 55 (1988).

F. Laruelle, P. Hu, R. Simes, R. Kubena, W. Robinson, J. Merz, and P.M. Petroff, J. Vac. Sci. Technol. B 7, 2034 (1989).

3.22 F. Laruelle, A. Bagchi, M. Tsuchiya, J. Merz, and P.M. Petroff, Appl. Phys. Lett. 56, 1561 (1990).

3.23 H. Sawaragi, H. Manabe, H. Kasahara, R. Aihara, K. Nakamura, F. Nihei, Y. Ochiai, S. Matsui, and T. Nozaki, Jpn. J. Appl. Phys. 28, 2095 (1989).

3.24 R.L. Williams, M. Dion, F. Chatenoud, and K. Dzurko, Appl. Phys. Lett. 58, 1816 (1991).

3.25 W.K. Chu, J.W. Mayer, and M.-A. Nicolet, Backscattering Spectrometry (Academic, New York, 1978).

3.26 J.W. Mayer, L. Erikson, and J.A. Davies, Ion Implantation (Academic, New York, 1970).

3.27 F. Laruelle, A. Bagchi, M. Tsuchiya, J. Merz, and P.M. Petroff, Appl. Phys. Lett. 56, 1561 (1990).

3.28 P.M. Petroff, Xueyu Quian, P.O. Holtz, R.J. Simes, J.H. English, J. Merz, and R. Kubena, Mater. Res. Soc. Symp. 126, 55 (1988).

3.29 F. Laruelle, Y.P. Hu, R. Simes, R. Kubena, W. Robinson, J. Merz, and P.M. Petroff, J. Vac. Sci. Technol. B 7, 2034 (1989).

F. Laruelle, A. Bagchi, M. Tsuchiya, J. Merz, and P.M. Petroff, Appl. Phys. Lett. 56, 1561 (1990).

F. Laruelle, Y.P. Hu, R. Simes, W. Robinson, J. Merz, and P.M. Petroff, Surf. Sci. 228, 306 (1990).

3.30 J.W. Mayer, L. Erikson, and J.A. Davies, Ion Implantation (Academic, New York, 1970).

T.E. Jackman, S. Charbonneau, L.B. Allard, R.L. Williams, I.M. Templeton, M. Buchanan, M. Vos, I.V. Mitchell, and J.A. Jackman, Appl. Phys. Lett. 58, 2733 (1991).

3.31 F. Laruelle, Y.P. Hu, R. Simes, W. Robinson, J. Merz, and P.M. Petroff, Surf. Sci. 228, 306 (1990).

3.32 Y. Hirayama, Jpn. J. Appl. Phys. 28, L162 (1989).

3.33 M. Vos, C. Wu, I.V. Mitchell, T.E. Jackman, and J.-M. Baribeau, Appl. Phys. Lett. 58, 951 (1991).

3.34 T.E. Jackman, J.-M. Baribeau, D.J. Lockwood, P. Aebi, T. Tylisczazk, and A.P. Hitchock, Phys. Rev. B 45, (23) 13591.

3.35 W.K. Chu, J.W. Mayer, and M.-A. Nicolet, Backscattering Spectrometry (Academic, New York, 1978).

J.F. Ziegler, J.P. Biersack, and U. Littmark, The Stopping and Ion Range of Ions in Matter (Pergamon, New York, 1985), Vol.1.

3.36 T.E. Jackman, J.A. Davies, and D. Chivers, Nucl. Instrum. Methods B 19/20, 345 (1987).

3.37 J.P. McCarthy (unpublished)

3.38 I.M. Templeton, private communication.

3.39 S.H. Pan, H. Shen, Z. Hang, F.H. Pollack, W. Zhuang, Q. Xu, A.P. Roth, R.A. Masut, C. Lacelle, and D. Morris, Phys. Rev. B 38, 3375 (1988).

D. Morris, Ph.D. thesis, University of Montreal, 1990.

3.40 S.H. Pan, H. Shen, Z. Hang, F.H. Pollack, W. Zhuang, Q. Xu, A.P. Roth, R.A. Masut, C. Lacelle, and D. Morris, Phys. Rev. B 38, 3375 (1988).

3.41 J. Cibert and P.M. Petroff, Phys. Rev. B 36, 3243 (1987).

3.42 W. Trzciakowski and A.P. Roth, Superlattices and Microstructures 6, 315 (1989).

3.43 T.E. Jackman, S. Charbonneau, L.B. Allard, R.L. Williams, I.M. Templeton, M. Buchanan, M. Vos, I.V. Mitchell, and J.A. Jackman, Appl. Phys. Lett. 58, 2733 (1991).

3.44 F. Laruelle, A. Bagchi, M. Tsuchiya, J. Merz, and P.M. Petroff, Appl. Phys. Lett. 56, 1561 (1990).

F. Laruelle, Y.P. Hu, R. Simes, W. Robinson, J. Merz, and P.M. Petroff, Surf. Sci. 228, 306 (1990).

3.45 K.T. Tsen, O.F. Sankey, G. Halama, S.-C. Y. Tsen, and H. Morkoç, Phys. Rev. B 39, 6276 (1989). We have measured the exciton lifetime to be 300 ps and assumed the lateral diffusion coefficient to be 120 cm^2/s (quoted by those authors for GaAs quantum wells).

3.46 J.S. Vetrano, M.W. Bench, I.M. Robertson, and M.A. Kirk, Met. Trans. A 20A, 2673 (1989).

3.47 M. Bode, A. Ourmazd, J. Cunningham, and M.W. Hong, Phys. Rev. Lett. 67, 843 (1991).

3.48 R. Kalish, L.-Y. Kramer, K.-K. Law, J.L. Merz, L.C. Feldman, D.C. Jacobson, and B.E. Weir, Appl. Phys. Lett. 61, 2589 (1992).

3.49 D.A. Kleinman, Phys. Rev. B 28, 871 (1983).

3.50 Y. Nomura, K. Shinozaki, and M. Ishii, J. Appl. Phys. 58, 1864 (1985).

B.J. Skromme, R. Bhat, and M.A. Koza, Appl. Phys. Lett. 52, 990 (1988).

3.51 S. Charbonneau, T. Steiner, M.L.W. Thewalt, E.S. Koteles, J.Y. Chi, and B. Elman, Phys. Rev. B 38, 3583 (1988).

Chapter 4

4.1 J.H. English, A.C. Gossard, W. Wiegmann, R. Bondal, and K. Baldwin, Appl. Phys. Lett. 50, 1826 (1987).

4.2 L.M. Smith, J.S. Preston, J.P. Wolfe, D.R. Wake, J. Klem, T. Henderson, H. Morkoç, Phys. Rev. B 39, 1862 (1989).

4.3 J. Hegarty, M.D. Sturge, J. Opt. Soc. Am. B 2, No. 7, July 1985.

4.4 H. Hillmer, A. Forchel, S. Hansmann, M. Morohashi, E. Lopez, H.P. Meier, K. Ploog, Phys. Rev. B 39, 10901 (1989).

4.5 J. Feldmann, G. Peter, E.O. Göbel, P. Dawson, K. Moore, C. Foxon, and R.J. Elliott, Phys. Rev. Lett. 59, 2337 (1987).

4.6 D.R. Wake, H.W. Yoon, J.P. Wolfe, and H. Morkoç, Phys. Rev. B <u>46</u> (20) 13452 (1992).